Dipl.-Ing. Johannes Konrad Strasser, BSc

Magnetic Resonance Elastography of the Human Brain

DOCTORAL THESIS

to achieve the university degree of

Doktor der technischen Wissenschaften

submitted to

Graz University of Technology

Supervisor

Univ.-Prof. Dipl.-Ing. Dr.techn. Rudolf Stollberger
Institute of Medical Engineering

Co-Supervisor

Assoc.-Prof. Univ.-Doz. Dipl.-Ing. Dr.techn. Stefan Ropele
Department of Neurology
Medical University of Graz

Graz, Austria, March 2021

Abstract

Magnetic resonance imaging (MRI) is one of the most essential imaging modalities in neuroscience. Routine MRI of the brain is often key supportive to successful diagnosis and monitoring of neurological diseases. Nevertheless, various neurological disorder characteristics may be undistinguishable by clinically established MRI contrasts, encouraging research and development of advanced MRI techniques. Many neurological diseases cause changes in the cerebral microstructure and concomitant alterations in the mechanical tissue properties. Motivated by manual palpation, where irregularities in the mechanical stiffness of tissue are assessed by hand, magnetic resonance elastography (MRE) enables visualization and quantification of mechanical tissue properties. Especially in neuroscience, the novel image contrast of MRE offers innovative possibilities for characterizing the brain tissue and for detecting tissue alterations. Even in encapsulated and deeper lying tissues such as the brain, which is usually not accessible to manual palpation in vivo. Technically, MRE probes the propagation of induced mechanical wave motions within the tissue at several points in time. The gathered image series is used to estimate the underlying mechanical properties such as the tissue shear modulus or stiffness. In this thesis, a novel MRE acquisition sequence scheme was developed for the investigation of the human brain. This imaging scheme allows sampling the propagation of the wave at several discrete time points in a single run. The benefits of the presented approach are short acquisition times coupled with reduced imaging artifacts and the use of low frequencies for the mechanical wave motion excitation. This is especially desirable in brain MRE to investigate deeper lying cerebral areas, as low frequency waves propagate deeper into the tissue. In a second approach, the scheme was enhanced to additionally acquire the three-dimensional motion components at once. Phantom experiments were performed to validate the proposed methods. The method was also validated in the brain of healthy subjects and regional shear moduli were assessed in different brain areas at an excitation frequency of 20 Hz. Due to the reduced acquisition time, the proposed MRE sequence can be integrated into a clinical MRI protocol and is currently part of an ongoing brain MRE study in patients with multiple sclerosis.

Keywords: Magnetic resonance elastography, brain, low-frequency waves, DENSE-MRE, wave sampling

Kurzfassung

Die Magnetresonanz-Tomographie (MRT) ist eines der wichtigsten Bildgebungsverfahren in den Neurowissenschaften. Für eine erfolgreiche Diagnose und Verlaufsüberwachung einer neurologischen Erkrankung ist ein Routine-MRT des Gehirns häufig wesentlich unterstützend. Trotzdem können verschiedene neurologische Krankheitsbild-Merkmale in Routine-MRT-Kontrasten ununterscheidbar sein, was Ansporn zur Forschung und Entwicklung von modernen MRT-Techniken liefert. Zahlreiche neurologische Erkrankungen verursachen Veränderungen in der zerebralen Mikrostruktur und damit einhergehende Änderungen der mechanischen Gewebeeigenschaften. Motiviert durch die manuelle Palpation, bei der Unregelmäßigkeiten in der mechanischen Steifigkeit eines Gewebes per Hand beurteilt werden, ermöglicht es die Magnet-Resonanz-Elastographie (MRE), die mechanischen Eigenschafen des Gewebes zu visualisieren und zu quantifizieren. Speziell in den Neurowissenschaften bietet der neuartige Bildkontrast der MRE innovative Möglichkeiten, das Hirngewebe zu charakterisieren und Veränderungen des Gewebes zu detektieren. Sogar in eingekapselten und tiefer liegenden Geweben wie dem Gehirn, welches normalerweise für ein manuelles Abtasten in vivo nicht zugänglich ist. Aus technischer Sicht untersucht die MRE die Ausbreitung induzierter mechanischer Wellenbewegungen innerhalb des Gewebes zu mehreren Zeitpunkten. Die aufgenommene Bildserie wird dazu verwendet, die zugrundeliegenden mechanischen Eigenschaften, wie den Gewebe-Schubmodul beziehungsweise die Steifigkeit, zu bewerten. In dieser Doktorarbeit wurde eine neuartige MRE-Bildaufnahme-Sequenz-Methode zur Untersuchung des menschlichen Gehirns entwickelt. Dieses Aufnahmeschema erlaubt es, die Wellenausbreitung zu mehreren diskreten Zeitpunkten während eines einzigen Durchlaufs abzutasten. Die Vorteile der präsentierten Methode sind kurze Untersuchungszeiten gekoppelt mit reduzierten Bildartefakten und die Anwendung von niedrigen Frequenzen für die mechanische Wellenbewegungsanregung. Dies ist besonders in der Hirn-MRE erstrebenswert, um tiefer liegende Gehirnareale untersuchen zu können, da sich niederfrequente Wellen tiefer in das Gewebe ausbreiten. In einer zweiten Herangehensweise wurde die Methode weiterentwickelt um zusätzlich auch die drei-dimensionalen Bewegungskomponenten auf einmal aufzunehmen. Um die vorgestellten Methoden zu bestätigen wurden Phantom-Experimente durchgeführt. Weiters wurde die Methode im menschlichen Gehirn gesunder Probanden validiert und regionale Werte der Schubmodule in verschiedenen Gehirn-Arealen bei einer Anregungsfrequenz von 20 Hz bestimmt. Aufgrund der reduzierten Aufnahmezeit kann die vorgestellte MRE-Sequenz in ein klinisches MRT-Protokoll integriert werden und ist derzeit Teil einer laufenden Gehirn-MRE-Studie an Patienten mit Multipler Sklerose.

Schlüsselwörter: Magnetresonanz-Elastographie, Gehirn, niederfrequente Wellen, DENSE-MRE, Wellen-Abtastung

List of publications

The outcomes of this work led to the following thesis-related peer-reviewed publication and conference proceedings and parts of this thesis are based on these publications:

Publications related to the thesis

Journal publications

Strasser J, Haindl MT, Stollberger R, Fazekas F, Ropele S. Magnetic resonance elastography of the human brain using a multiphase DENSE acquisition. *Magnetic Resonance in Medicine*, 81(6):3578-3587, 2019. doi: 10.1002/mrm.27672

Conference proceedings

Strasser J, Soellradl M, Enzinger C, Ropele S. Accelerating DENSE MR elastography by including multi-axes motion encoding into the multiphase DENSE-MRE acquisition scheme. *In Proceedings of the ISMRM 28th Annual Meeting and Exhibition 2020*, page 0170, 2020. ***ISMRM Magna Cum Laude Merit Award***

Strasser J, Fazekas F, Ropele S. Low frequency excited MR elastography of the brain using displacement encoding with stimulated echoes and multi phase offset readouts. *In Proceedings of the Joint Annual Meeting ISMRM-ESMRMB 2018*, page 2282, 2018.

Strasser J, Pirpamer L, Fazekas F, Ropele S. Fast Magnetic Resonance Elastography using a DENSE approach with Multi Phase Offset Readout. *In Proceedings of the ISMRM 25th Annual Meeting and Exhibition 2017*, page 1370, 2017.

Publications unrelated to the thesis

Journal publications

Soellradl M, **Strasser J**, Lesch A, Stollberger R, Ropele S, Langkammer C. Adaptive slice-specific z-shimming for 2D spoiled gradient-echo sequences. *Magnetic Resonance in Medicine*, (July):1-13, 2020, doi: 10.1002/mrm.28468

Soellradl M, Lesch A, **Strasser J**, Pirpamer L, Stollberger R, Ropele S, Langkammer C. Assessment and correction of macroscopic field variations in 2D spoiled gradient-echo sequences. *Magnetic Resonance in Medicine*, 84(2):620-633, 2020, doi: 10.1002/mrm.28139

Üçal M, Haindl MT, Adzemovic M Z, **Strasser J**, Theisl L, Zeitelhofer M, Kraitsy K, Ropele S, Schäfer U, Fazekas F, Hochmeister S. Widespread cortical demyelination of both hemispheres can be induced by injection of pro-inflammatory cytokines via an implanted catheter in the cortex of MOG-immunized rats. *Experimental Neurology*, 294:32-44, 2017, doi: 10.1016/j.expneurol.2017.04.014

Conference proceedings

Soellradl M, **Strasser J**, Ropele S, Langkammer C. Adaptive and slice-specific z-shimming approach for signal rephasing in 2D multi gradient echo imaging. *In Proceedings of the ISMRM 28th Annual Meeting and Exhibition 2020*, page 3152, 2020.

Haindl MT, Üçal M, Zeitelhofer-Adzemovic M, **Strasser J**, Theisl L, Ropele S, Schäfer U, Fazekas F, Hochmeister S. Ausgedehnte kortikale Demyelinisierung beider Hemisphären kann durch Injektion proinflammatorischer Cytokine über einen im Kortex von MOG-immunisierten Ratten implantierten Katheter erzielt werden. *14. Jahrestagung der Österreichischen Gesellschaft für Neurologie.* MAR 22-24, 2017.

Hochmeister S, Üçal M, Haindl MT, Zeitelhofer-Adzemovic M, Theisl L, **Strasser J**, Ropele S, Schäfer U, Fazekas F. Widespread cortical demyelination of both hemispheres can be induced by injection of pro-inflammatory cytokines via an implanted catheter in the cortex of MOG-immunized rats. *32th Congress of the European Committee for Treatment and Research in Multiple Sclerosis*, page 167, 2016.

Strasser J, Roland J, Reiter G, Stollberger R. Parameter Optimization for Liver MR Elastography at 3 T. *In Proceedings of the ISMRM 21st Annual Meeting and Exhibition 2013*, page 4074, 2013.

Diwoky C, Binter C, **Strasser J**, Stollberger R. Waveform Optimized (Easy to Build) Pulsatile Flow Phantom of the Common Carotid Artery. *Proceedings of the International Society for Magnetic Resonance in Medicine 18*, page 1353, 2010.

Affidavit

I declare that I have authored this thesis independently, have not used any other sources/resources than those listed, and have explicitly indicated all material which has been quoted either literally or by content from the sources used.

The text document uploaded to TUGRAZonline is identical to the present doctoral thesis.

Date

Signature

Acknowledgments

First of all, I want to thank Prof. Rudolf Stollberger, who offered me the chance to make my PhD in the fascinating field of MRE and supervised me all the time during my studies.

Furthermore, I want to thank Assoc. Prof. Christian Langkammer for his beneficial comments and suggestions while finalizing my thesis and for his time as reviewer and examiner.

A special thank goes to Assoc. Prof. Stefan Ropele, who gave me the opportunity to be part of his team and do research in the fascinating field of brain MRE. Thank you very much for your support and for encouraging me to implement DENSE for brain MRE.

I also thank DI Stefan Eggenreich, who carefully proof-read my thesis and gave me valuable comments while finishing my thesis.

I want to thank all my current and former colleagues from the great MRI team in Graz and my great colleagues from the Department of Neurology for the wonderful time over the years of work together, and all my friends who supported me also beyond this work.

To my parents and sisters and my whole extendet family: Thank you very much for supporting me all the time. *Family – one of the most valuable things in life.*

Contents

Chapter 1

Introduction

1.1 Magnetic resonance elastography

Magnetic resonance elastography (MRE) is an imaging technique capable of visualizing the viscoelastic mechanical properties (or stiffness) of tissue in vivo [1, 2]. The clinical value behind this technique is linked to the fact that structural changes of biological tissues are indicated by their viscoelastic properties at multiple orders of magnitude with high sensitivity [3]. A lot of conditions can alter tissue stiffness and abnormities of the tissue can show up in its haptic behavior. An assessment of haptic behavior by manual palpation is used for disease investigation and identification since the early times of medical examination [4]. During palpation, the tissue typically experiences shear deformation without compression [4]. The resistance against the deformation depends on the cellular network and can change enormously within progression of several diseases [4]. In times of medical imaging, palpation is still relevant [4] and techniques to noninvasively palpate and assess the mechanical properties of tissue are searched for [5]. Technically, the resistance against shear deformation can be described by a quantity called shear modulus G [6]. When a mechanical force acts onto an area to deform a material, it will lead to a mechanical stress inside the material. The shear modulus thereby couples the extent of material deformation to the applied shear stress. Hence, probing tissue to assess its shear modulus can be performed in vivo by visualizing tissue deformation due to an applied deformation excitation. Magnetic resonance imaging (MRI) offers an elegant way to visualize tissue deformations as MRI is capable of measuring the motion of magnetic spins [7]. The MRI technique which utilizes the measurement of tissue motion to assess tissue mechanical characteristics is called magnetic resonance elastography [7]. The first publication of elastography dates back to 1991, when it was introduced as an ultrasound-based technique for assessment of the elastic modulus by the detection of tissue deformation due to external compression [6, 8]. In MRE, the shear modulus of the tissue is assessed and represented in maps. During the years of MRE development, two different approaches to identify the stiffness of the material have been introduced, namely the static MRE and the dynamic MRE. In the static MRE, the displacement of the material is measured when undergoing a defined compression [9]. The materials position is thus measured before the loading and again after the full loading has been performed and the deformation process reaches a steady condition [9]. Combined with the compression stress, the elastic modulus E can be assessed [9]. However the accurate stress field is challenging to be determined due to difficult boundary conditions and unknown applied forces [10]. For that reason, static MRE is not widely used nowadays in MRE research. The most popular technique is the dynamic MRE [11]. To overcome the problem of the unknown exact compression field, dynamic MRE uses a different approach of assessing the mechanical characteristics of tissue. Based on mechanical wave propagation, in dynamic MRE the shear modulus can be assessed without the limitation of the unknown stress field [10]. A further benefit is, in contrast to static MRE, that dynamic MRE allows probing also deeper lying tissue layers [4]. Hence, dynamic magnetic resonance elastography has been explored in a wide area of applications. Nearly every organ has been investigated for tissue stiffness assessment using MRE since the invention of the technique [12].

1.2 Clinical applications

This thesis focuses on MRE of the human brain – nevertheless, besides the brain, MRE has been applied to a variety of other human organs in the past years. Thus a short overview of several MRE applications to the human body is provided here. Beyond this, further information can be found in MRE books by Venkatesh et al. [1] and Hirsch et al. [2] as well as in a variety of review articles.

In 1995, the first key publication on magnetic resonance elastography (MRE) was presented by Muthupillai et al. [13]. The idea of elasticity imaging was already known from the field of ultrasound [14, 8] and Muthupillai et al. showed how elastography can be performed on the MRI scanner by visualization of propagating acoustic strain waves [13, 5, 15]. Since this, the MRE field grew continuously and researchers started to investigate the human body and organs with the new technique aiming to characterize the biomechanical tissue properties and find disease related changes therein.

In one of the first MRE publications, acoustic waves were imaged in human muscles [15]. Investigating human muscles with MRE is obvious as muscles, during their natural action, undergo active and passive variations in their mechanical properties and upon the muscles contractile state, its stiffness changes [10, 11]. Alterations in these properties can be associated with diseased conditions [16] and in vivo muscle MRE can be used for studying the physiological response of the muscles [10]. Besides disease related aspects also aspects like sports training could be studied using muscle MRE [11]. Dresner et al. found a linear stiffness increase in the biceps brachii muscle while active and passive tension and dependent upon the muscle size [17]. Variations in the stiffness of different muscles were found by Uffmann et al., who investigated four different muscles – the biceps brachii, the flexor digitorum profundus, the soleus and the gastrocnemius – in healthy volunteers [18]. In a more recent study, nine muscles in the thigh at rest were investigated in vivo in healthy subjects by Chakouch et al. aiming as a first step in the development of a muscle atlas [19]. And for diseased muscles versus healthy controls, several studies showed differences in the viscoelastic properties – either higher or lower values depending on the disease type [20, 21, 22]. Further information on muscle MRE can be found e.g. in the review articles by Glaser et al. [11] and Strijkers et al. [23].

In oncology, MRE has been used for the study of cancer, utilizing the unique contrast mechanism of altered cancerous tissue mechanical properties in various organs [6]. MRE investigations of the breast for example searched for lesion classification, pre-operative tumor delineation as well as treatment response [12, 24]. In the detection of a breast lump, manual palpation is important and recommended as part of routine screening [10, 12]. Diagnosis at an early stage and monitoring of treatment can lower the risk of breast cancer accompanied mortality [1]. Diagnostic value of breast stiffness assessment is suggested since malign carcinoma have a higher stiffness than benign fibroadenomas and both have increased stiffness compared to surrounding tissue [12]. Development of breast MRE techniques and investigation of the breast tissue thus started early after the invention of MRE [25, 24, 26]. So far, as a clinical routine tool, breast MRE has not become widely used [12]. Nevertheless, breast MRE continues to evolve since research is still in ongoing development [27, 28, 29] with extended potential areas from lesion differentiating to pre-operative tumor delineation, staging or prediction of metastatic potential of primary tumors [12]. Further information on breast MRE provide e.g. the review articles by Bohte et al. [12] and Patel et al. [29].

The application of MRE to investigate the heart has also been reported [30, 4, 31, 11, 32]. Cardiac stiffness is coupled with the pressure inside the ventricle, thus stiffness changes are an indicator for lost in pump power or increased cardiac work load [4]. Technically, cardiac MRE is challenging, as the heart is shielded by the lungs and chest on the one hand and also has its own motion on the other hand [4]. Advances in MRE acquisition techniques were thus proposed aiming for faster motion encoding to facilitate the applicability of MRE to investigate the heart [31, 33].

For a variety of organs in the abdomen, MRE investigations have been reported – among others spleen, kidneys, pancreas and with the most prominent application of MRE in the liver [34, 35, 36, 2]. MRE has been used in the liver for the non-invasive investigation of chronic liver diseases. The application of MRE for examining diseased livers is one of the most established applications of MRE, especially for the detection of liver fibrosis, as liver fibrosis cannot be identified by routine imaging [34, 37]. Studies have shown a high correlation between liver stiffness and the fibrosis stage determined by the reference standard liver biopsy and histopathology [38, 39, 40]. The non-invasiveness of MRE is an enormous advantage compared to biopsy [37] and meta-analysis studies have further demonstrated its high diagnostic accuracy for the quantification and detection of liver fibrosis [41, 42, 43, 44]. To investigate the liver, MRE assessed liver stiffness has already become beneficial in clinical routine in many centers and provides significant additional information in the detection and characterization of chronic liver disease [45]. Especially, liver MRE is valuable in follow-up exams as it offers high accuracy and excellent re-test reliability as well as intra- and interobserver reproducibility [45]. For the non-invasive assessment of liver fibrosis, MRE represents the most accurate technique [35]. Although liver fibrosis can be characterized by an increased liver stiffness, there are technical confounders like left versus right liver lobe measurements or depth of the measurement [46]. Also MRE-technique specific aspects like the used wave frequency or actuation device influence the gathered quantitative results [46]. The major technical reason for MRE to fail is liver iron overload and associated MR signal loss [37, 47]. There are also other biologic confounders which alter the assessed liver stiffness [46, 45]. Several biological circumstances like hepatic steatosis, inflammation, cholestasis, hepatic venous congestion, right heart failure, or non-disease related conditions like fasting or breathing aspects can alter the MRE assessed liver stiffness [46]. Besides fibrosis assessment, MRE was also used to characterize liver tumors [48, 49, 50]. And in a longitudinal investigation, Ichikawa et al. demonstrated that MRE can predict the development of hepatocellular carcinoma in chronic liver disease [51].

1.3 MRE in the human brain

Since the beginning of MRE, the brain was of high interest to be investigated with this new imaging technique. Neurological disorders are part of major public health concerns in developed countries [52]. Hence, research using the special imaging contrast for neuroscientific application and examining the promising potential of MRE for brain investigations is reasoned. Even though palpation of the brain had no clinical precedent, examining its mechanical properties could help to characterize brain disease or to perform analysis and simulations for brain trauma and surgeries [53].

To identify disease-related alterations in the brain tissues viscoelasticity, knowledge about healthy brain tissue viscoelasticity is indispensable. Hence, various publications reporting brain MRE studies of healthy participants can be found in the literature. However, often healthy participants are also investigated to emphasize technical improvements of the MRE data acquisition, which is typically performed in a rather small cohort [54]. Studies focusing on the explicit exploration of healthy brains often comprise more subjects. The analysis of the quantitative shear modulus values reaches from global assessments within the whole brain to regional assessments in specific brain areas to get insight into the brain mechanical behavior in vivo. It was found that natural biological factors as age and gender have impact on the viscoelasticity of brains [55, 56]. Sack et al. found a decline of global viscoelastic modulus with an increase in age [55, 57]. This was also confirmed by Arani et al. for several specific brain regions as in the cerebrum, frontal lobes, occipital lobes, parietal lobes and temporal lobes [56]. However, in some areas like the cerebellum and the sensory-motor regions, they could not observe a significant correlation between stiffness and age [56]. For the impact of gender, Sack et al. found female brains to have higher global stiffness than their male counterparts [55]. Arani et al. reported female brains to be stiffer in the areas of temporal lobes and occipital lobes but they found no significant difference in other investigated brain areas [56]. Hiscox et al. merged MRE data from multiple studies, which resulted in a large cohort of 134 young subjects in total and they on the other hand found male cortical gray matter to be stiffer within the frontal and parietal lobes [54]. They further mentioned the possibility of changes in the relationship over time as their cohort consisted of young subjects whereas Arani et al. [56] investigated older adults and hence further investigations are needed to learn more about the gender dimorphisms over age [54]. Stiffness variations in different brain structures were investigated in several studies ranging from distinguishing grey matter from white matter [58, 59, 60] over different white matter structures [61] and subcortical gray matter structures [62] and even towards an elastographic atlas of the brain [63, 54].

Besides healthy subjects, MRE has been used to study a variety of neurological diseases. In Alzheimer's disease, Murphy et al. investigated whether MRE assessed stiffness could indicate disease related tissue property changes [64]. They found significantly decreased stiffness values in patients compared to cognitively normal controls [64]. MRE assessed brain stiffness was also investigated as potential biomarker for behavioral variant frontotemporal dementia by Huston et al. [65]. The stiffness was assessed in different brain areas of a group of five patients as well as nine normal controls and significantly decreased stiffness values were observed in regions covering whole brain, frontal lobe and temporal lobes of patients in contrast to controls [65]. ElSheikh et al. investigated patients with different types of dementia and assessed the brain tissue stiffness in the areas unique to each dementing disorder with the intention to obtain a potential dementia type distinguishing biomarker [66]. In their study, they found dependent on the type of disease, regional tissue stiffening (normal pressure hydrocephalus: parietal, occipital, sensorimotor regions), softening (Alzheimer's disease: parietal lobe and sensorimotor region; Alzheimer's disease and frontotemporal dementia: frontal and temporal lobes) and also no significant alteration within the examined regions (dementia with Lewy bodies) [66].

Streitberger et al. performed mechanical imaging of Glioblastoma in 22 patients prior to surgery and found that Glioblastoma have high intratumor heterogeneity with stiff and soft compartments [67]. In the stiffness maps, they obtained in the majority of the cohort significantly decreased values within the Glioblastoma, however, some Glioblastoma also showed higher values [67]. Besides stiffness variations, they found in the viscosity-related maps a reduction in the values in all Glioblastoma indicating a reduced viscous behavior of the tumors in contrast to healthy tissue [67].

Lipp et al. investigated patients with Parkinson's disease and progressive supranuclear palsy and found significantly decreased stiffness in the frontal and mesencephalic regions in patients compared with healthy controls and correlations of the decreased stiffness with brain atrophy in the patients group [68].

In multiple sclerosis patients with mild relapsing-remitting disease course, Würfel et al. performed MRE and found a significant decrease in global cerebral stiffness compared with matched healthy volunteers [69]. Streitberger et al. investigated patients with chronic-progressive multiple sclerosis and found a reduced stiffness in the patients compared to healthy control subjects on the one hand and compared with early relapsing-remitting multiple sclerosis patients on the other hand [3]. Fehlner et al. investigated patients with clinically isolated syndrome and showed a reduced white matter stiffness in the patients over controls, independent of multiple sclerosis imaging markers and clinical scores [70]. They concluded that their findings raise the potential of MRE as an imaging marker in neuroinflammatory diseases for subtle and diffuse tissue damage [70].

Further overview of brain MRE applications in healthy subjects and patients provide e.g. the review articles by Hiscox et al. [52] and Murphy et al. [71]. The direct comparison between studies is often difficult, as there exist substantial variations in the used MRE imaging protocols and stiffness estimation algorithms [54]. MRE offers a potential benefit in a variety of neurological diseases, nevertheless, significant possibilities remain to enhance the technique and gain wider knowledge of the physiological processes behind [71].

1.4 Aim of this work

Encouraged by the promising research across the world in the field of MRE this thesis aimed at making MRE also clinically applicable for investigating the brain. Numerous neurological diseases can affect the microstructure of the brain which usually comes along with a modification of the mechanical tissue properties. Information on changes of the brain mechanical properties could therefore add to conventional MRI and could be relevant for diagnosis and monitoring of various neurological diseases. However, MRE acquisition techniques capable of detecting these mechanical property modifications are still an unmet need in clinical routine. The primary goal of this thesis was thus to develop an innovative and improved image acquisition approach, which allows highly efficient MRE data acquisition in the human brain especially in basal regions of the brain.

Chapter 2

Theory

The theory chapter describes fundamental technical aspects of MRE. Starting with an overview of the principles of MRE, the subsequent section explains in detail the underlying mathematical equations and the mechanical excitation prodecure. Continuing with a general view on how the elastography acquisition via MR imaging sequences is conventionally performed, it follows with the essential background of stimulated echo imaging and their use in MRE acquisitions. Subsequent to the acquisition, image post-processing to obtain shear modulus maps is described.

2.1 Principles of MRE

Magnetic resonance elastography aims at offering a technical way of palpation and assessing viscoelastic tissue characteristics to provide supportive information additional to traditional diagnostic imaging. The assessment of the mechanical tissue properties via MRE can be subdivided into three principle steps [11]. At first, a source of motion or mechanical stress deforms the tissue to a certain extent [11]. The generated tissue deformation resulting from this mechanical excitation depends on the tissue's viscoelastic properties. Deformation of the tissue implies a displacement of the regional spins used for MR imaging [7]. Thus, in the second step, the generated tissue deformation can be imaged as displacement fields by a motion encoding MR sequence [11]. The third step to perform MRE is image processing. Via an inversion algorithm, the imaged displacement fields are processed to maps of mechanical properties which are known as elastograms [11]. For a better structure the following sections start with describing the mathematical equations and continue with explanations of the mechanical excitation.

2.2 Wave motion within the tissue

The concept of dynamic MRE bases on the measurement of tissue motion. The following subsections thus describe the underlying mathematical equations and reported options of motion excitation within the tissue.

2.2.1 Equations of wave motion and shear modulus

To assess the mechanical characteristics of tissue, a mathematical model is used to gain the sought quantities based on other values which are measurable. In dynamic MRE, this starts with the equations of motion. Several assumptions thereby allow simplifications during mathematical modeling. The mechanical excitation generates tissue displacements which introduce a mechanical stress and strain. The displacements produced during MRE measurements in the order of micrometer, thus Hook's law can be assumed, which gives a linear relationship between the mechanical stress σ (units Pa) and the material strain ϵ (dimensionless) [53, 72].

In tension and compression processes, the normal stress σ_n is coupled to the longitudinal strain ϵ by Young's modulus E (units Pa), which describes the resistance against deformation, by [72]:

$$\sigma_n = E\epsilon. \tag{2.1}$$

In shearing processes, a shear stress τ (units Pa) causes a tilting deformation of a material by an angle γ (units radians). In this case, the shear modulus G (units Pa) describes the resistance against the deformation and the relationship between shear stress and transversal strain is given by [72]:

$$\tau = G\hat{\gamma}, \tag{2.2}$$

with $\hat{\gamma} = tan(\gamma) = \frac{\Delta z}{y}$ as clarified in Figure 2.1.

In a general case, the relationship between stress and strain can be described by a rank four tensor including up to 36 independent quantities [53]. However, the simplification of material isotropy put into practice in MRE reduces this amount down to two independent quantities [53]. These two quantities are the first Lamé parameter λ (units Pa) and second Lamé parameter – the shear modulus G – (in literature also often denoted as μ) associated with longitudinal and shear deformation, respectively [53]. Taking Poisson's ratio ν (dimensionless), which describes the ratio between the transverse and longitudinal strains within a material [72], the Lamé constants can be set into relation with Young's modulus in the following way [73]:

$$\lambda = \frac{E\nu}{(1+\nu)(1-2\nu)}, \tag{2.3}$$

$$G = \frac{E}{2(1+\nu)}. \tag{2.4}$$

For soft tissues, the values of Poisson's ratio are in the range of 0.490 to 0.499 [53, 74]. With the assumption of ν of soft tissues beeing close to the value of liquids ($\nu = 0.5$), the two moduli G and E only differ by a factor of 3 [53]:

$$E = 3G. \tag{2.5}$$

In this case, the assessment of either G or E yields the same informative content of the biomechanical tissue characteristics [10].

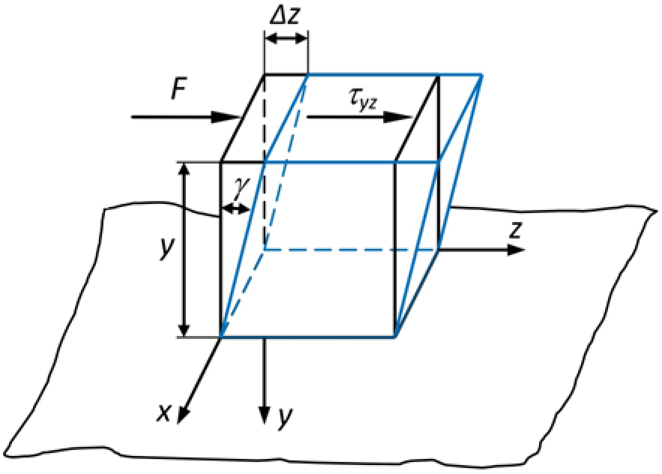

Figure 2.1: Schematic illustration of shear deformation. A force F acting onto an area and the associated shear stress τ causes a tilting deformation described by the angle γ. (modified from [72])

In the general case, the stress-strain-relationship for a linear-elastic material is now given by [53]:

$$\sigma_{ij} = 2G\epsilon_{ij} + \lambda\delta_{ij}\epsilon_{kk} \tag{2.6}$$

for a mechanical stress σ_{ij} acting in direction j on an area which is orthogonal to i. δ_{ij} is thereby the Kronecker delta and over repeated indices is summed up [53].

The strain results from the displacement u (units m) of the tissue and the linear strain tensor ϵ_{ij} is given by the spatial derivative of the displacement with respect to the spatial coordinates x (units m) [53]:

$$\epsilon_{ij} = \frac{1}{2}\left(\frac{\partial u_i}{\partial x_j} + \frac{\partial u_j}{\partial x_i}\right). \tag{2.7}$$

Substituting Equation (2.7) into the general equation of motion neglecting external forces:

$$\rho\frac{\partial^2 u_i}{\partial t^2} = \frac{\partial \sigma_{ij}}{\partial x_j}, \tag{2.8}$$

with ρ as the material density (units kg/m^3), ∂ as the partial derivative and the time t (units s), yields the general wave equation in an isotropic, linear-elastic medium:

$$\frac{\partial}{\partial x_i}\left(\lambda\frac{\partial u_j}{\partial x_j}\right) + \frac{\partial}{\partial x_j}\left[G\left(\frac{\partial u_i}{\partial x_j} + \frac{\partial u_j}{\partial x_i}\right)\right] = \rho\frac{\partial^2 u_i}{\partial t^2}. \tag{2.9}$$

In case of a harmonic motion of the displacement:

$$\vec{u}(\vec{x}, t) = \vec{u}(\vec{x})e^{i\omega t}, \tag{2.10}$$

with angular frequency $\omega = 2\pi f$ (units 1/s), the displacement field $\vec{u}(\vec{x}, t)$ becomes $\vec{u}(\vec{x}, \omega)$. Thus the second time derivative of $\vec{u}(\vec{x}, \omega)$ reduces to a factor of $-\omega^2$, yielding:

$$\frac{\partial}{\partial x_i}\left(\lambda\frac{\partial u_j}{\partial x_j}\right) + \frac{\partial}{\partial x_j}\left[G\left(\frac{\partial u_i}{\partial x_j} + \frac{\partial u_j}{\partial x_i}\right)\right] = -\rho\omega^2 u_i, \tag{2.11}$$

which can be written in vectorial notation, using the gradient operator $\vec{\nabla}$ [73]:

$$\vec{\nabla}(\lambda + G)\vec{\nabla}\cdot\vec{u}(\vec{x}, \omega) + \vec{\nabla}\cdot G\vec{\nabla}\vec{u}(\vec{x}, \omega) = -\rho\omega^2\vec{u}(\vec{x}, \omega). \tag{2.12}$$

Assuming local homogeneity, the two Lamé constants become single unknowns independent of the position resulting in an algebraic matrix equation [53]:

$$(\lambda + G)\vec{\nabla}(\vec{\nabla}\cdot\vec{u}(\vec{x}, \omega)) + G\Delta\vec{u}(\vec{x}, \omega) = -\rho\omega^2\vec{u}(\vec{x}, \omega), \tag{2.13}$$

with Δ as the Laplace operator.

MRE assessment primarily focuses on the shear modulus G. An explanation therefor give the Equations (2.3) and (2.4), which show that for values of ν reaching 0.5, the values of λ are in another order of magnitude than those of G. λ is typically 10^4 or more times higher than G in soft tissues [53]. This difference in magnitude makes it difficult to assess both quantities, G and λ, simultaneously, but a separation of both variables can be performed effectively by separating the displacement field $\vec{u}(\vec{x}, \omega)$ [53]. The displacement $\vec{u}(\vec{x}, \omega)$ consists of longitudinal and transversal waves. It is thus desired to split the information of both wave types within the full displacement field data. The longitudinal waves have a very low spatial frequency (near zero) with tens of meters in wavelength [53]. Spatial image filtering can thus effectively remove longitudinal waves from the displacement images [53]. Moreover, the separation of the wave types can also be performed mathematically. The displacement field can be split into two additive terms – a divergence-free part and a curl-free part. The curl-free part (with $\nabla \times \vec{u} = 0$) corresponds to the longitudinal compressional waves, whereas the divergence-free field (with $\nabla \cdot \vec{u} = 0$) contains the transversal shear waves [53]. Assuming also incompressibility of the material (Poisson's ratio $\nu = 0.5$ [74]), the displacement field is divergence-free (with the shear wave field $\vec{u}_S$) and Equation (2.13) reduces to the Helmholtz equation [53]:

$$G\Delta\vec{u}_S(\vec{x},\omega) = -\rho\omega^2\vec{u}_S(\vec{x},\omega). \tag{2.14}$$

In this Equation (2.14), the three orthogonal direction components of the displacement field $\vec{u}$ are now decoupled, enabling the calculation of the shear modulus by considering only one direction component in the equation [53].

So far, elastic material behavior was considered. To additionally involve viscous tissue properties, the time derivative of the strain $\dot{\epsilon}$ has to be incorporated into the equations which can be achieved, when the Lamé constants are considered as complex quantities. The equations above thus also describe viscoelastic material characteristics, and the Lamé constants consist of a real part and an imaginary part [53]. The complex shear modulus G^* is given as:

$$G^* = G' + iG''. \tag{2.15}$$

The real part G' is called storage modulus and represents the elastic behavior [62]. Its imaginary part G'' is the loss modulus and describes the viscous properties [62].

Alternatively, the complex shear modulus can be presented in terms of magnitude $|G^*|$ and phase angle $\angle(G^*)$. $|G^*|$ describes the amount of storage and loss characteristics, which in biological tissue are both expected to increase with increasing tissue network density [63]. $\angle(G^*)$ estimates the ratio between material elasticity and viscosity [2] and depends on the geometrical mechanical lattice characteristics [63].

$$|G^*| = \sqrt{(G')^2 + (G'')^2} \tag{2.16}$$

$$\angle(G^*) = \arctan\left(\frac{G''}{G'}\right) \tag{2.17}$$

$$G^* = |G^*|e^{i\angle(\mathrm{G}^*)} \tag{2.18}$$

In MRE are also composite measures of the storage and loss moduli frequently used. The shear stiffness (or effective shear modulus) μ relates to the resistance of a viscoelastic solid against a harmonic shear stress [62]. The damping ratio ξ describes the motion attenuation, where motion decays quickly with absence of oscillation for values of $\xi > 1$ [62].

$$\mu = \frac{2|G^*|^2}{(G' + |G^*|)} \tag{2.19}$$

$$\xi = \frac{G''}{2G'} \tag{2.20}$$

The mechanical property quantities can alternatively be represented by the shear wave speed c (units m/s) and shear wave damping Γ (dimensionless) [75, 53, 52]. The shear stiffness is coupled to the wave speed in the following way [53, 74]:

$$\mu = \rho c^2 = \rho \lambda_{sp}^2 f^2, \tag{2.21}$$

with the spatial wavelength λ_{sp} (units 1/m) and the frequency $f = \omega/2\pi$ (units Hz). The shear wave speed is thus:

$$c = \sqrt{\frac{\mu}{\rho}}. \tag{2.22}$$

In terms of the complex shear modulus, the shear wave speed and shear wave damping are [75]:

$$c = \frac{1}{\Re\left(\sqrt{\frac{\rho}{G^*}}\right)} \tag{2.23}$$

and

$$\Gamma = \omega \Im \left(\sqrt{\frac{\rho}{G^*}} \right), \tag{2.24}$$

with $\Re$ indicating the real part and $\Im$ indicating the imaginary part of the complex value.

The complex shear modulus and derivated quantities are functions of the frequency and depend on the mechanical harmonic wave motion frequency [53, 62, 75]:

$$G^* = G^*(\omega), \tag{2.25}$$

which has to be considered when comparing assessed shear moduli of different MRE experiments with different mechanical excitation frequencies.

2.2.2 Mechanical excitation

To be able to assess the shear modulus in MRE, the concept of wave motion and associated mathematical modeling is used as described in Chapter 2.2.1. Generating appropriate wave motion within the tissue is thus necessary for the investigation. The desired wave motion is typically induced by an external actuator. This actuator device vibrates and generates the small tissue displacements while it is synchronized to the MRE imaging sequence. MR compatibility of such devices is thus necessary, as well as consideration of patient safety and comfort aspects. The design of an actuation system that is capable of providing adequate mechanical excitation on the one hand and works within the MR scanner's magnetic field on the other hand is a main issue in MRE [7]. To allow a sufficient wave propergation to the investigated organ, the vibration amplitude at the body surface is preferably more than $200\,\mu$m [76]. Diverse mechanical actuation devices have been reported in the literature and used for studies in the past, which work due to different principles on how the vibration is produced and transmitted into the human body. Most of the devices consist of active parts, which generate the harmonic vibration and passive parts which induce the actual motion movement into the body. The active parts are often placed outside the MR scanner room to avoid interfering issues with the strong magnetic field of the MR scanner. In contrast, other techniques precisely make use of the existing magnetic field to operate. For the diverse actuation systems, widely used types are based on pneumatic concepts, electromagnetic approaches or piezoelectric principles [7, 76, 2]. The next passages shall elucidate these concepts.

Pneumatic device types use air pressure variations to transmit the generated harmonic vibrations into the human body [38, 77]. A loudspeaker, placed outside the scanner room generates the harmonic waves. The speaker system is sealed airtight to a tube which leads to a passive driver that is placed onto the subject and transmits the vibration into the body [38, 77]. Although, longitudinal vibrations are produced in the first place, mode conversion from the longitudinal vibrations to shear waves occurs at the applicator borders and interfaces within the body [52, 78]. Depending on the type of MRE examination, several adaptations of the passive driver part were introduced to investigate different organs of the body [34, 77]. For example, for liver MRE, a 19-cm drum-like passive driver was used by Yin et al. and placed on the anterior body wall [38]. The simultaneous use of two passive drivers at different positions was proposed to illuminate larger regions of the tissue with wave propagation and counteract wave damping issues [79]. And especially for brain MRE investigations, a soft pillow-like passive driver has been designed which is placed under the subjects head within the MR head coil [6, 80, 81]. Beneficial at these device types is that the active hardware part does not require strict MRI compatibility as it is placed outside the scanner room and only the passive parts are exposed to the magnetic field [76].

Another concept are electromagnetic excitation systems [82, 76]. These type of actuators act directly inside the MR scanner. The system uses small coils, which are fed with an electric alternating current. In presence of the main magnetic field of the MR scanner and according to Lorentz law, the small coils make alternating movements [76]. Developments enhanced the technique to allow a variably orientated shear wave excitation via a motion redirecting hardware [82]. To reduce electromagnetic interference and influences of switching magnetic field gradients, the coils can be optimized, however, near the coil, the main magnetic field can be affected and cause imaging artifacts [76]. Especially for brain MRE, these systems were used with the coils fixed at a bite bar [83, 58] or coils fixed to a cradle where the subjects head was placed onto [58] to induce the motion into the head.

Besides, a widely used system creates the motion via piezoceramics. A waveform generator powers the piezoelectric actor and a rigid rod transmits the motion from the actor to the passive driver part placed in contact with the human body. For the MRE investigations of the brain, such a system was introduced by Guo et al. using a cradle positioned under the subjects head as passive driver part [63]. In further MRE studies, the cradle was even omitted and Hirsch et al. directly connected the rod to the subject through a rubber mat and investigated liver and spleen [84].

Developments of new actuation systems are still ongoing. Novel concepts of motion excitation were introduced, which e.g. produce the desired mechanical waves by the help of a small rotating eccentric mass [78, 27]. In addition to explicit actuation devices, also suggestions for feasible alternative mechanical motions were made. A possible way of performing MRE without a special actuation device was introduced by Gallichan et al., who were using the scanner hardware to produce an external excitation [85]. They implemented low frequency switching imaging gradients in their MR sequence, which were used to generate vibrations in the patient table for the MRE excitation [85]. Besides technical motion actuation, also intrinsic actuation due to pulsation during the cardiac cycle was used to investigate the brain [86, 87].

Further overview and detailed descriptions of different systems can be found e.g. in the articles by Tse et al. [76] and Uffmann et al. [7].

Besides different device types, it is also relevant in context of mechanical excitation to consider the applied frequency and amplitude of the vibration. The choice of the excitation frequency is crucial in MRE experiments. Human soft tissue has the ability to absorb mechanical energy to in general prevent itself from getting disrupted by too high shear rates [4]. For MRE this means, that the induced waves are getting damped by the tissue which restricts the applicable actuation frequencies. Higher frequency waves can theoretically provide a higher spatial resolution in the elastograms [4, 52]. However, higher frequencies also require higher vibration amplitudes to penetrate the skull [52]. In contrast, lower frequency waves attenuate less rapidly and the lower the frequency of the shear waves is, the deeper is their penetration into the tissue [4, 52]. Hence, a balance between penetration depth, resolution and noise is required [52]. Applied frequencies in brain MRE experiments thus typically range from 10 Hz to 100 Hz and the majority of brain MRE investigations were performed with 50 Hz to 60 Hz [52]. Besides single frequency experiments, brain MRE examinations with multiple frequencies ranging from 10 Hz to 62.5 Hz have also been frequently used [75, 63, 88, 89, 90].

In this work, a single low excitation frequency has been used for brain MRE to allow the shear modulus assessment in deeper brain regions. The mechanical actuation has been performed with a piezoceramic actuation system, which is described in the next subsection.

2.2.3 Motion excitation via a piezoceramic actor

The MRE investigations in this thesis were performed using a piezoceramic actuation system. The system comprises several active and passive parts. A high power wave form generator (CGC Instruments, Chemnitz, Germany) represents the control unit and produces the required electrical voltage to power the piezoceramics. The frequency and amplitude of the voltage can be adjusted to match the desired experimental setup. An optical fiberglass cable connects the device to the MR scanner which triggers the wave form generation repeatedly to ensure synchronization between the vibration and the MR imaging sequence. A filter unit reduces high frequency interferences in the transfered voltage before the shielded cable reaches inside the scanner room and the voltage energizes the piezoceramic actuator (SPL Spindel und Praezisionslager GmbH, Ebersbach, Germany). In Figure 2.2, the wave form generator and the piezoceramic actor are depicted.

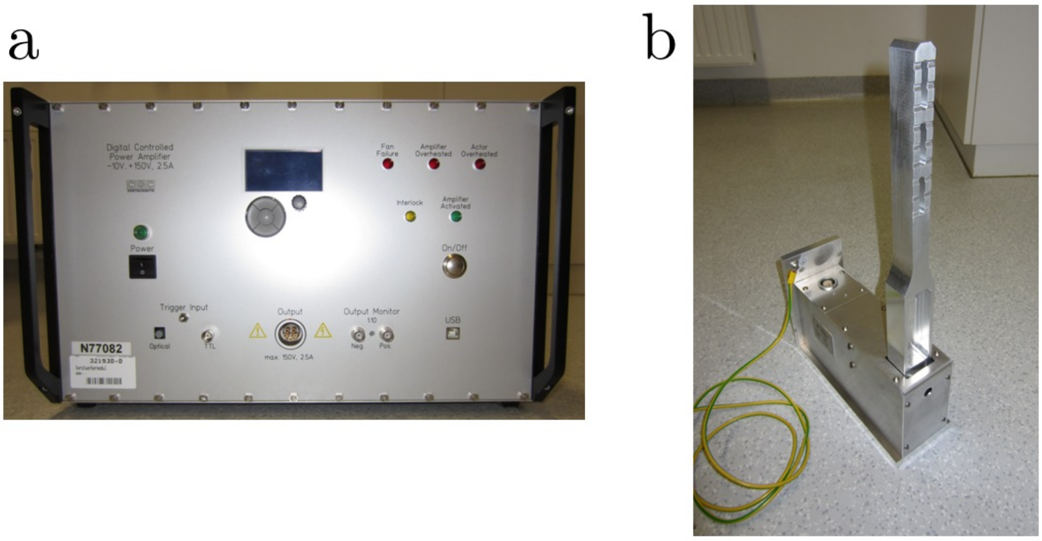

Figure 2.2: The high power digital waveform generator (a) and piezoceramic actuation device (b) used in this work for the generation of motion.

While the waveform generator was placed outside the scanner room, the actuator was fixated on the feet end of the MR scanner's patient table. A carbon fiber rigid rod transmits the generated motion to a head rocker, which is shown in Figure 2.3.

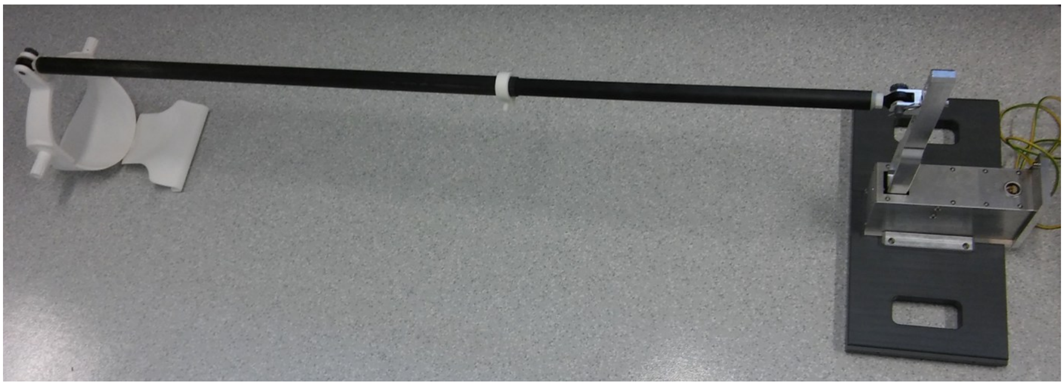

Figure 2.3: The piezoceramic actuator coupled to a head rocker via a carbon fiber rod.

The head rocker is placed in the 20-channel head coil (Figure 2.4) at the head end of the patient table and the actuator's motion forces a tiny nodding movement of the person's head or the phantom during the MRE examination. Figure 2.5 shows the complete MRE setup on the patient table of the MR scanner.

Figure 2.4: The 20-channel head coil with the specially designed head rocker mounted.

The phantom or the subjects head is fixed with foam material inside the rocker to perform the MRE experiments. Thus the wave motion penetrates appropriately into the investigated tissue. A harmonic excitation of the investigated tissue is ensured by a continuous sinusoidal vibration with a single frequency throughout the complete MR sequence execution. To guarantee synchronicity, the control unit is repeatedly triggered by the MR sequence during the whole image acquisition.

2.3 MRE acquisition technique

MRE imaging sequences utilize motion encoding to gather the wave motion information within the tissue, generated by the mechanical excitation. The acquisition sequence thereby captures snapshots of the wave patterns and thus the current tissue displacements at defined points in time. An optimal synchronization between the excitation and

Figure 2.5: The excitation device mounted on the patient table of the MR scanner.

the imaging sequence is required to avoid motion blurring artifacts within the images. Hence, MRE sequences typically contain trigger pulses to link the sequence execution to the actuation device. To acquire the images, several strategies have been reported. An overview of MRE acquisition techniques can be found in the article by Guenthner et al. [91]. Basically, a variety of MR imaging sequences can be adapted to allow MRE acquisitions. Hence, MRE has been performed with gradient echo (GE) sequences [13, 38, 92, 47], spin echo (SE) sequences [93], balanced steady-state free precession (bSSFP) sequences [94], stimulated echo sequences [31] and accelerated and advanced readout schemes like multi-echo GE [95], echo planar imaging (EPI) readouts [47] or spiral trajectories [60]. While each acquisition approach has its own benefits and limitations, they usually have one thing in common: Motion encoding gradients are implemented into the sequence to encode the wave motion into the MR phase image.

2.3.1 Wave motion encoding in phase images

The tissue motions in MRE experiments are encoded into the phase of the MR signal. The phase image thus depicts the displacements of the tissue. This phase-contrast MR imaging technique is capable of detecting tissue displacements in the order of hundreds of nanometers [15]. The following equations describe the motion encoding into the phase signal by means of a gradient.

The MR signal phase $\varPhi$ (units rad) of a spin isochromat at a position $r(t)$ (units m) in presence of an applied magnetic field gradient $G(t)$ (units T/m) is given by [96]:

$$\varPhi = \gamma \int_0^{\tau} G(t) \cdot r(t) dt, \tag{2.26}$$

with the gyromagnetic constant γ ($\gamma_{proton} = 42.576\ \frac{\mathrm{MHz}}{\mathrm{T}}\, 2\pi$ rad) and the duration τ (units s) of the gradient [96]. A phase is thus accumulated during τ. A pair of two gradients with the same durations however with opposite gradient amplitudes ($G_1 = -G_2$), hence a bipolar gradient:

$$G(t) = \begin{cases} G_1, & 0 < t \leq \tau \\ G_2, & \Delta t < t \leq \Delta t + \tau \end{cases} \tag{2.27}$$

allows encoding the motion of an isochromat along the gradient direction. The resulting phase for stationary isochromats is zero, whereas for moved isochromates an accumulated phase remains. A schematic illustration of this motion encoding is depicted in Figure 2.6 for an arbitrary gradient axis.

Gradients which encode the motion are commonly called motion encoding gradients (MEG) in MRE. With the strength and duration of the MEG, the extend of generated phase is controlled. The ratio between the maximum generated phase $\varPhi_{max}$ and encoded displacement u describes the encoding efficiency E_0 (units rad/m) [89]:

$$E_0 = \frac{\varPhi_{max}}{u}. \tag{2.28}$$

Assuming a displacement of an isochromat from position r_1 to r_2 in the time gap between the two gradients, the generated phase shift reads:

$$\varPhi = \gamma \int_0^{\tau} G_1 r_1 dt + \gamma \int_{\Delta t}^{\Delta t + \tau} G_2 r_2 dt = \gamma G_1 \tau (r_1 - r_2) = \gamma G_1 \tau u. \tag{2.29}$$

Hence, the generated signal phase is proportional to the tissue's displacement. A case, where the motion only occurs in the gap between the two gradients, is given in static MRE experiments [9]. Here, G_1 generates an initial phase before a motion actuator forces a step displacement of the tissue from state A to state B. Within the tissue, a steady state of the movement has to settle before G_2 completes the motion encoding.

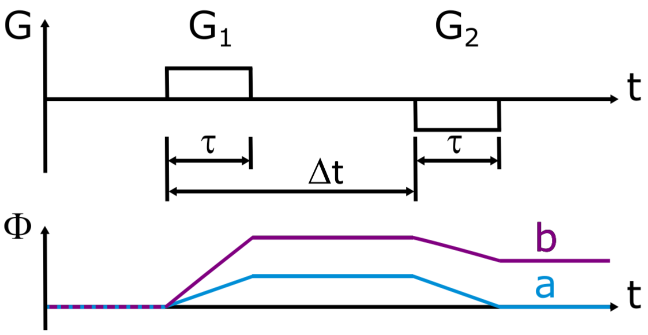

Figure 2.6: Schematic illustration of the accumulated phase due to a gradient pair G_1 and G_2 with opposite amplitudes for a stationary (a) and a moved spin isochromat (b). (modified from [96])

The use of a dynamic motion excitation with a harmonic vibration on the other hand causes a displacement that varies over time and follows a sinusoidal function

$$r(t) = r_0 \sin(2\pi f_u t + \delta), \tag{2.30}$$

with amplitude r_0 and frequency f_u (units Hz) according to the excitation and a constant phase offset δ (units rad). As long as the MEGs are short enough and sufficiently separated from each other ($\tau << \Delta t$ in Figure 2.6), the motion during the gradient pulse is negligible [24]. Thus the positions r_1 and r_2 are simply evaluated via Equation (2.30) at the time points of the activated gradients G_1 and G_2 and the phase shift results from Equation (2.29). Quasistatic MRE experiments use this approximation to measure the displacement using very low dynamic excitation frequencies of e.g. 1 Hz [24]. The separation Δt is thereby long due to the long vibration period $T_u = \frac{1}{f_u}$ (units s).

In classical time-harmonic dynamic MRE, this condition is usually not fully applicable. Longer gradient durations and higher excitation frequencies influence the behavior and so the approximation of a constant position during the MEG is no longer valid. Thus, the sine function of the motion has to be taken into account. By substituting Equation (2.30) into Equation (2.26), the motion encoded signal phase becomes:

$$\Phi = \gamma \int_0^\tau G(t) r(t) dt = \gamma \int_0^\tau G(t) r_0 \sin(2\pi f_u t + \delta) dt. \tag{2.31}$$

Inserting Equation (2.27) into Equation (2.31) yields the two phases Φ_1 and Φ_2 according to G_1 and G_2 [31]:

$$\Phi_1 = \frac{\gamma G_1 r_0}{\pi f_u} \sin(\pi f_u \tau) \sin(\pi f_u \tau + \delta), \tag{2.32}$$

$$\varPhi_2 = \frac{\gamma G_2 r_0}{\pi f_u} \sin(\pi f_u \tau) \sin(\pi f_u \tau + 2\pi f_u \Delta t + \delta). \tag{2.33}$$

With $G_2 = -G_1$, the summed phase reads:

$$\varPhi = \varPhi_1 + \varPhi_2 = \frac{\gamma G_1 r_0}{\pi f_u} \sin(\pi f_u \tau) \left[\sin(\pi f_u \tau + \delta) - \sin(\pi f_u \tau + 2\pi f_u \Delta t + \delta)\right]. \tag{2.34}$$

By choosing the gap between the gradients to match half a period of the excitation vibration $\Delta t = \frac{T_u}{2} = \frac{1}{2 f_u}$, the summed phase becomes twice the phase $\varPhi_1$ [31]:

$$\varPhi = 2\frac{\gamma G_1 r_0}{\pi f_u} \sin(\pi f_u \tau) \sin(\pi f_u \tau + \delta). \tag{2.35}$$

Furthermore, by matching the gradient durations to the excitation wave period as $\tau = \frac{T_u}{2} = \frac{1}{2 f_u}$, thus

$$G(t) = \begin{cases} G_1, & 0 < t \leq \frac{T}{2} \\ -G_1, & \frac{T}{2} < t \leq T, \end{cases} \tag{2.36}$$

the accumulated phase becomes:

$$\varPhi = 2\frac{\gamma G_1 r_0}{\pi f_u} \sin\left(\frac{\pi}{2}\right) \sin\left(\frac{\pi}{2} + \delta\right) = 2\frac{\gamma G_1 r_0}{\pi f_u} \cos(\delta). \tag{2.37}$$

Equation (2.37) describes the case of conventional motion encoding in MRE using one rectangular shaped bipolar MEG with 0^{th} gradient moment nulling [97].

2.3.2 Conventional motion encoding

In a conventional MRE sequence, an MEG is inserted in the used MR sequence and the duration of the MEG thereby matches a full vibration period ($T_{MEG} = T_u$) [10]. The bipolar shape implies zeroth gradient moment nulling. Thus, static spin isochromats do not contribute to the accumulated phase, but non-static spins do. Figure 2.7 illustrates a conventional MEG and its relation to the excitation motion schematically.

Besides rectangular shaped MEGs, also sinusoidal MEGs are used [97]. Additionally, first order moment nulling can be applied, which, for example, a cosine-shaped MEG fulfills [98, 99]. In this case, spin isochromats with higher order motion terms, like acceleration, contribute to the acquired phase but static terms and also first order velocity motion terms result in zero net phase. Thus, unwanted tissue motion coming from e.g. pulsation can be suppressed in the acquired images which can be beneficial for in vivo acquisitions [98]. Increased motion sensitivity can be achieved by using a higher number of MEGs instead of a single one [15]. However, the fact that the conventional MEG lasts for the complete vibration wave period can restrain its suitability for use, because lower vi-

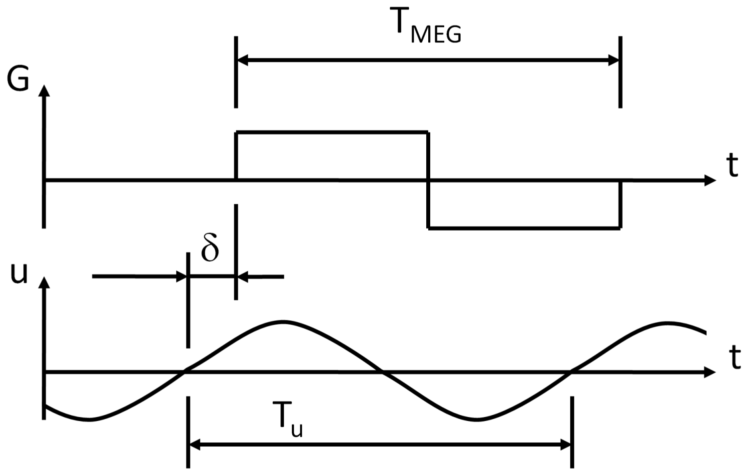

Figure 2.7: Schematic illustration of an MEG and the excitation motion in conventional MRE. (modified from [10])

bration frequencies lengthen the MEG duration remarkably. Hence, the minimum feasible echotime (TE) prolongs. Adjustments of the conventional MEG were thus introduced.

2.3.3 Fractional motion encoding

The coupling of the mechancial excitation frequency to the MEG frequency in conventional motion encoding prolongs sequence timings, meaning TE and the repetition time (TR) are always longer than the actuation wave period [33]. To overcome the issue of long MEG durations, a technique called fractional motion encoding was invented [33]. In this approach, the MEG duration is shorter than the vibration period ($T_{MEG} < T_u$), thus, only a fraction of the motion is encoded into the MR phase signal. Hence, also TE and TR can be shorter than the excitation wave period. On the one hand, especially in tissues having short transverse relaxation times, reducing TE results in a less evolved MR signal decay which brings along a higher measurable MR signal. And on the other hand, decoupling of the MEG duration from the mechanical excitation frequency also simplifies the use of low vibration frequencies with long wave period times. This approach was first introduced in a bSSFP sequence [33] but can be applied to any sequence type. In modern EPI based MRE sequences, fractional motion encoding is involved combined with variable MEG numbers to optimize the encoding efficiency for a desired TE [89].

2.3.4 Motion encoding via imaging gradients

Alternative approaches to circumvent conventional motion encoding were also proposed. As every gradient produces a spin dephasing, ideas arose to perform motion encoding using gradients, which are already included in a standard MR sequence. Imaging gradients as the readout encoding gradients can be used to encode the motion into the phase images

[100, 101]. Omitting the additional MEG results in some benefits. Due to the saved MEG time, TE can be shortened, thus, also the acquisition time (TA) can be reduced and the MR signal is higher since its decay is less progressed [100]. In contrast, the motion encoding sensitivity is reduced compared to applying explicit MEGs, which can be counteracted with higher excitation amplitudes [100]. Alternatively, the sensitivity can be enhanced via optimized imaging parameter settings of the sequence. By acquiring multi-echo gradient-echo images with symmetrical bipolar readout gradients and excitation-synchronized echo acquisitions, the motion encoding sensitivity can be magnified [101]. From echo to echo, the wave amplitudes are thereby more pronounced in the resulting phase images [101]. However, as the readout gradients act MEG-like, the displacement encoding axis is defined by the readout direction and thus through-plane motion cannot be acquired with this approach [101].

2.3.5 Phase offsets to sample the wave motion

The acquisition of a motion encoded MR phase image results in one snapshot of the mechanical wave patterns. The information of the temporal wave propergation, however, is relevant to assess the viscoelastic mechanical tissue properties, which characterize not only the static but also the dynamic material behavior. Thus, in dynamic MRE acquisitions, the tissue motion is imaged at several discrete time points resulting in different wave snapshots. As the MEG captures the motion, acquiring the wave snapshots is achieved by adjusting the offset between the MEG and the mechanical motion [53]. Therefor, the offset δ (see Figure 2.7) in Equations (2.30)-(2.37) is varied over subsequent acquisitions in conventional MRE imaging approaches. Typically four to eight temporal snapshots are then imaged, equally spaced across one vibration period, and these images are called phase offsets [10]. As a result, a series of phase offset images is acquired which shows the propagation of the waves over time.

The phase offsets can be realized by different strategies. One possibility is to shift the MEG within the interval between the radiofrequency (RF) pulse and the readout gradient. The start time point of the MEG is thereby chosen to reach the desired temporal phase shift. The minimum TE of the sequence is thus limited not only by the MEG duration but additionally by the longest temporal MEG shift. To allow shorter TEs, the MEG onset can be fixed within the sequence time course and the shift is realized by adapting the trigger of the excitation device for each phase offset. In that case, to allow the wave propagation to settle to a new steady state at the next phase offset, several additional TRs are typically executed without data acquisition prior to the actual acquisition of the phase offset image.

TR is typically set to an integer multiple of the exctitation wave period, to ensure a steady state of the wave during acquisition of each phase offset. Alternatively, the phase shifts can be realized by adjusting TR properly. If the desired phase shift is achieved via a specfic TR, TRs without data acquisition can be skipped resulting in a reduction of scantime [102].

2.3.6 Full motion vector field encoding

In general, the mechanical waves propagate through the tissue in three-dimensional space. Hence, the acquisition of the full three-dimensional wave propagation field is necessary for an optimal MRE examination. As the MEG is sensitive to the motion components in MEG direction, due to the scalar product in Equation (2.26), only one motion direction is encoded by a single MEG. An MRE sequence is thus typically repeated with switched MEG axis in the subsequent acquisitions to gather all three orthogonal motion directions [11]. Especially in brain MRE, the full wave information is required for high quality MRE examinations [83]. Advanced acquisition approaches were thus proposed to acquire all motion components simultaneously to reduce total scan time. In SLIM-MRE [103, 98], MEGs are applied simultaneously on all three gradient axes with a specific temporal offset. Instead of sampling the wave motion over one wave period, the sample intervals are modulated differently for each MEG axis over several wave periods. After Fourier transform (FT) of the dataset along time dimension, each motion component corresponds to a separate bin of the computed spectrum and can be extracted.

2.3.7 Stimulated echo motion encoding – DENSE-MRE

Besides acquiring wave images by means of gradient echoes or spin echoes, the motion can also be imaged using another type of echoes – the stimulated echoes. The use of stimulated echo sequences for motion encoding offers several useful benefits in contrast to conventional motion encoding schemes used in MRE. To understand this concept, the next sections describe the stimulated echoes starting with their generation, followed by their use for displacement encoding and their applicability for dynamic MRE.

2.3.7.1 Stimulated echoes

To describe the generation process of stimulated echoes, a three-pulse experiment is used [104, 105]. In a sequence with three 90° RF pulses, the first RF pulse flips the magnetization onto the transverse plane. Directly after this first RF pulse, the transverse magnetization decays and starts to dephase and relaxate with the relaxation time T2. The dephasing process in this preparation part however has some beneficial effects which can be utilized. By applying a second RF pulse after an echo time portion TE/2, the magnetization gets flipped back onto the longitudinal axis. Due to the dephasing occurred before, the magnetization is now prepared with a modulation pattern. Stored on the longitudinal axis, the magnetization now relaxates with the relaxation time T1 during the mixing time (TM) period. A third RF pulse, applied after a certain TM, continues to use the prepared longitudinal magnetization and flips it back onto the transverse plane. In this readout part, the magnetization rephases again after TE/2 and forms to the so-called stimulated echo (STE). Figure 2.8 shows the manipulation steps of the magnetization (green) during this experiment.

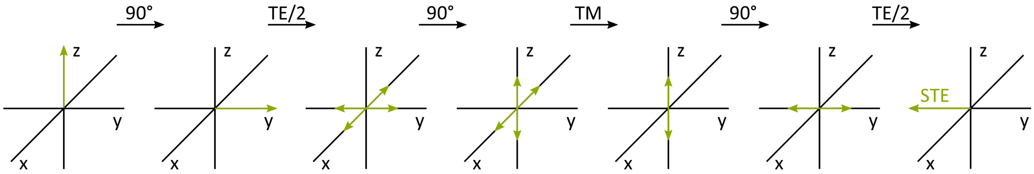

Figure 2.8: Simplified scheme of a stimulated echo formation. (modified from [104])

Besides the formation of one stimulated echo, such a three-pulse experiment also generates multiple spin echoes (SE) [104, 105], as illustrated in Figure 2.9. The second RF pulse forms the first spin echo (SE1) during the mixing time part, since it rephases the dephased magnetization from the preparation part. Applying the third RF pulse leads to three more spin echoes. The spin echo SE2 results from directly refocusing the dephased SE1 with the third RF pulse. Further on, the third RF pulse generates a spin echo SE3 from the transverse magnetization emerging directly after the second RF pulse. And moreover, a fourth spin echo SE4 is generated by the third RF pulse, since it also refocuses the transverse magnetization emerging at the very beginning of the three-pulse experiment directly after the first RF pulse.

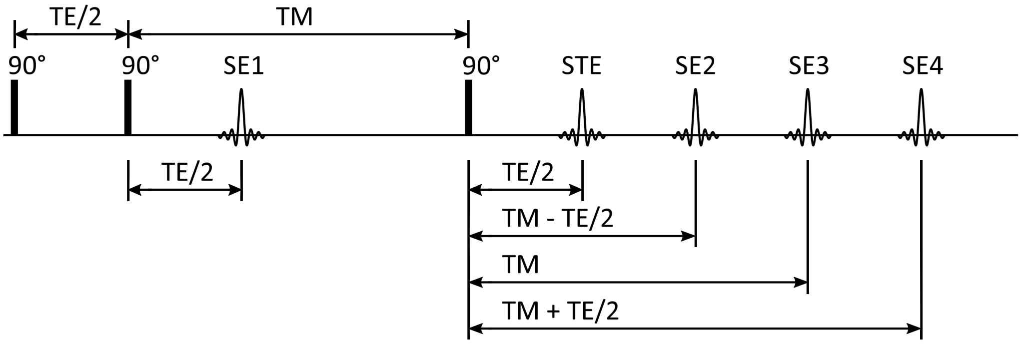

Figure 2.9: Spin echo (SE) and stimulated echo (STE) formations in a three-pulse experiment at the corresponding timings. (modified from [104])

Further detailed description of stimulated echoes can be found e.g. in the article by Burstein [104] or in the book of Haacke et al. [105].

2.3.7.2 Displacement encoding via stimulated echoes – DENSE

Besides the three RF pulses in a stimulated echo sequence, gradients can be included to influence the spin signal behavior [104]. A pair of gradients, one gradient after the first RF pulse and a similar gradient after the third RF pulse, is used to force a stimulated echo, while suppressing the spin echoes and also the free induction decay (FID) signal. As every gradient generates a phase shift of the spins, in consequence of such a gradient pair, if spins have moved during the time between the two gradients, the phase shift of the first and the shift of the second gradient differ and a net phase remains [104]. Stimulated echo sequences thus also allow encoding the motion into the phase images. With the description of the technique for measuring cardiac motions, the acronym DENSE, Displacement ENcoding via Stimulated Echoes, was introduced by Aletras et al. in 1999 [106].

2.3.7.3 Stimulated echoes for MRE acquisitions

The use of stimulated echo displacement encoding in MRE has already been reported in 1998 by Chenevert et al. [9] and in 2000 by Plewes et al. [24]. Both publications deal with static or quasi-static MRE and the long TM applicable in stimulated echo acquisitions allows a sufficient separation of the two MEG lobes and considering the tissue positions as constant during the active gradient times. Motion encoding is thus described by Equation (2.29). In 2009, Robert et al. [31] introduced the application of dynamic DENSE-MRE to investigate the human heart and described in detail the underlying dynamic motion encoding. Figure 2.10 illustrates the sequence concept for this dynamic DENSE-MRE. The generated phase according to the harmonic motion is now expressed by Equation (2.35), where G_1 and G_2 are separated by $\Delta t = T_u/2$. The opposite amplitudes of the gradients ($G_1 = -G_2$) match to the opposite directions of the motion half-wave. Each single phase offset is acquired consecutively by shifting the offset δ.

The encoding efficiency $E_{0,sp}$ is derived from Equations (2.28) and (2.35), where $\sin(\pi f_u \tau + \delta)$ is set to its maximum magnitude of 1, as:

$$E_{0,sp} = \frac{\Phi_{max}}{r_0} = 2\frac{\gamma G_1 r_0}{\pi f_u}\sin(\pi f_u \tau). \tag{2.38}$$

The fundamental strategy of DENSE-MRE was used to develop advanced multiphase DENSE-MRE [107, 108, 109] and multiaxes multiphase DENSE-MRE [110] acquisition concepts for brain MRE. Before these concepts are presented in specific chapters, the following section describes image post-processing steps, which are performed in MRE to process the acquired wave motion dataset to maps of mechanical tissue properties.

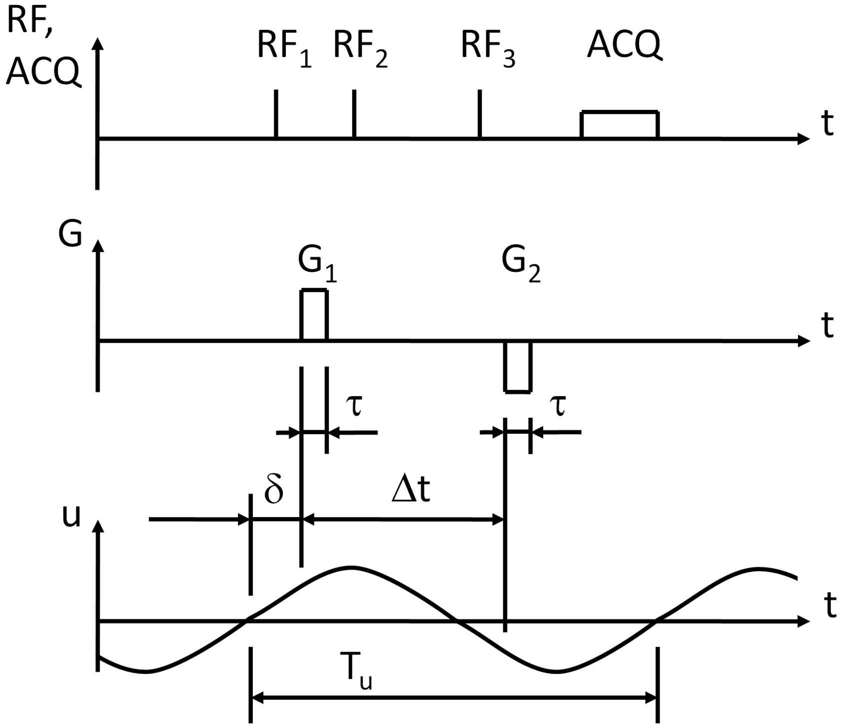

Figure 2.10: Schematic illustration of the MEGs G_1 and G_2 in dynamic DENSE-MRE. (modified from [31])

2.4 Image post-processing

In MRE experiments, the acquired series of phase offset images contains the propagation of the wave motion, the displacement field $\vec{u}(\vec{x}, t)$, within the tissue. With this encoded displacement field, the complex shear modulus G^* can be computed for the investigated material. However, the wave information within the phase offset images is superimposed by additional background phase values arising from general MR imaging aspects. Several image processing steps are thus inevitable, to prepare the wave images and for the determination of G^* maps. These steps usually include phase unwrapping, Fourier-extraction of the desired wave frequency component, filtering of noise and unsuitable wavelengths, and finally the mathematical inversion from wave motion information to shear modulus values.

2.4.1 Phase unwrapping

A characteristic of a phase signal is the limited encoding range of 2π for its values. For MRE motion encoding this means, that if the caused displacement in a voxel induces a larger phase shift than 2π, the phase will wrap into the 2π range and the appearing phase signal will differ from its actual developed value. The relation between the measured (wrapped) phase $\Phi_{wrapped}$ and the developed phase Φ at a given position and time point is [111]:

$$\Phi_{wrapped} = \Phi mod 2\pi + \Phi_L = \Phi - 2\pi \left\lfloor \frac{\Phi}{2\pi} \right\rfloor + \Phi_L, \tag{2.39}$$

with the modulo operation mod, the floor operation $\lfloor ... \rfloor$ for rounding down and the lower phase limit Φ_L (usually 0 or $-\pi$) of the 2π phase range $(\Phi_L, \Phi_L + 2\pi]$ [111]. Such phase wrapping effects can occur in the resulting phase image either as phase isocontours (closed loops or start- and end-point at object boundaries) or open-ended fringelines (termination of the wrap within the object) [111]. Estimating the actual total accumulated phase can be performed via an unwrapping technique, which adds the necessary integer number k of 2π shifts to the wrapped phase [112]:

$$\Phi_{unwrapped} = \Phi_{wrapped} + 2\pi k. \tag{2.40}$$

To remove wraps from an image, several phase unwrapping algorithms have been invented which, however, work with some uncertainty [113, 111, 112, 114]. In MRE studies, a variety of phase unwrapping algorithms has been applied [112, 114, 84]. Nevertheless, phase unwrapping is not straightforward since the process is an ill-posed problem [111]. But avoiding the phase wraps completely with an optimized acquisition is often not possible due to the wanted strong motion encoding and also the proceeding general phase accumulation during TE. However, a useful way to deal with wraps is to design further phase processing algorithms such, that wraps potentially vanish anyway. One option is the mathematical combination of phase images in the complex domain, whereby wraps under certain conditions inherently reduce or cancel out, which is utilized in this work (Chapter 3.4.2).

An alternative is to include the phase unwrapping mathematics intrinsically into a step of the MRE wave inversion algorithm [84]. The idea behind this approach is to work with the spatial derivatives of the phase data rather than with the raw phase image, as the inversion uses spatial derivative images (strain images) [84]. The direct calculating of spatial derivatives from the raw wrapped phase, generates strain images [115]:

$$\frac{\partial \Phi}{\partial(x,y)} = -i\, e^{(-i\Phi_{wrapped})} \frac{\partial e^{(i\Phi_{wrapped})}}{\partial(x,y)}. \tag{2.41}$$

This method is referred to as gradient based unwrapping and produces wrap-free and unbiased derivatives if the phase difference of two adjacent voxels is less or equal to π [84]. In the inversion algorithm applied in this thesis, such an approach is integrated (Chapter 2.4.5).

2.4.2 Excitation frequency extraction

In the dynamic phase offset image data, not only waves with the excitation frequency but also additional motion with other frequencies can appear, as for example slow bulk motion or direct current (DC) offsets. For further MRE processing, the excitation frequency component is relevant. Temporal filtering can be performed via one-dimensional discrete Fourier transform of the (real valued) phase image time series from time to frequency domain. The appropriate frequency bin is then selected to obtain a complex image of the wave patterns. This filtering step is often called first harmonic extraction. If one full period of the harmonic wave is sampled via an even number of equally spaced phase offsets and the Nyquist-Shannon sampling theorem is satisfied, hence four phase offsets or more are acquired, the bin corresponding to the excitation frequency will be the first harmonic bin, the first bin after the DC bin. The corresponding bin changes when other then one wave period is sampled, as it is for example utilized in SLIM-MRE [103]. The resulting complex image is called complex wave image, which is input to further processing steps.

2.4.3 Converting phase values to displacements

As described in Chapter 2.3.1, the acquired phase data is directly proportional to the underlying motion. The phase images can thus be converted to displacement maps. In dependence of the MEG, the appropriate equation has to be chosen. With the approximation of very short gradient durations and a long gap in between the two gradient lobes, Equation (2.29) can be rewritten as:

$$u = r_1 - r_2 = \frac{\Phi}{\gamma G_1 \tau}, \tag{2.42}$$

to obtain the displacement value. However, for different MRE acquisition approaches with different MEGs, the according conversion has to be derived. In general, if the encoding efficiency of an MRE sequence is given, the conversion simplifies to:

$$u = \frac{\Phi}{E_0}, \tag{2.43}$$

based on Equation (2.28).

2.4.4 Inversion to shear modulus

The wave images are the input to an algorithm that determines the shear modulus maps. These algorithms invert the wave equations (Chapter 2.2.1), thus they are typically called inversion algorithms. In the evolution of MRE, different strategies to recover the mechanical tissue properties from the gathered displacement data have been proposed. Inversion techniques reach from image filtering approaches, were local spatial wavelengths are estimated, over finite element reconstructions to mathematically modeling and solving the wave equations under various assumptions [53]. Also modern processing methods like artificial neural networks have been utilized for inversion [116]. A common analytic approach is the Helmholtz inversion, in which Equation (2.14) is inverted to obtain the shear modulus as [53]:

$$G = -\rho\omega^2 \frac{u}{\Delta u}. \tag{2.44}$$

The density ρ of the tissue is typically set to a constant value of around 1000 kg/m^3 during inversion [10].

2.4.5 MDEV wave inversion

In this work, 2D wave inversion by an multifrequency dual elasto visco (MDEV) algorithm [67, 117, 84, 63] was applied to estimate the complex shear modulus values. This inversion algorithm solves the Helmholtz equation in a least squares way, while processing the data of all motion encoding direction components ($j = 1, .., N_c$) and dealing with data from a multiple number of excitation frequencies ($l = 1, .., N_f$). The input phase images are filtered by a Gaussian smoothing filter to reduce noise before gradient unwrapping is performed. The data from every frequency and motion direction component is processed to two in-plane derivatives along the image axes ($k = 1, 2$). FT is applied along time-axis to obtain complex valued shear strain images $u^*_{j,k}(\omega_l)$ at the respective excitation frequency ω_l. A 2D Butterworth lowpass filter further smoothes the images befor the magnitude $|G^*|$ and phase angle $\angle(G^*)$ of the complex shear modulus are calculated according to [67]:

$$|G^*| = \rho \frac{\sum_{j=1}^{N_c} \sum_{k=1}^{2} \sum_{l=1}^{N_f} \omega_l^2 |u^*_{j,k}(\omega_l)|}{\sum_{j=1}^{N_c} \sum_{k=1}^{2} \sum_{l=1}^{N_f} |\Delta u^*_{j,k}(\omega_l)|} \tag{2.45}$$

and

$$\angle(G^*) = \arccos\left(-\frac{\sum_{j=1}^{N_c} \sum_{k=1}^{2} \sum_{l=1}^{N_f} \left[\Delta u'_{j,k}(\omega_l) u'_{j,k}(\omega_l) + \Delta u''_{j,k}(\omega_l) u''_{j,k}(\omega_l)\right]}{\sum_{j=1}^{N_c} \sum_{k=1}^{2} \sum_{l=1}^{N_f} |\Delta u^*_{j,k}(\omega_l)||u^*_{j,k}(\omega_l)|} \right). \tag{2.46}$$

Chapter 3

Multiphase DENSE-MRE

Parts of this chapter have been published in Strasser J. et al., Magn Reson Med. 2019;81(6):3578-3587 [109], Proc. ISMRM 2017 (1370) [107] and Proc. ISMRM 2018 (2282) [108].

On basis of the DENSE acquisition principles used for displacement encoding in MRE and other fields of MR imaging, a new MRE acquisition approach was developed, which accelerates the MRE phase offset sampling in a multiphase way. With dynamic wave sampling in MRE acquisitions, a series of phase offset images at different points in time is gathered. In conventional MRE sequences, this image series is acquired by repeated acquisitions, each shifted in time with respect to the mechanical excitation. The shift is thereby defined by the offset in phase δ in Equations (2.30)-(2.37). Classical DENSE-MRE approaches also utilize the concept of δ-shifts in Equation (2.35) to sample the wave and acquire each single phase offset individually over repeated measurements. Thus, this is called singlephase (sp) DENSE-MRE in the following text. In contrast, the developed multiphase (mp) DENSE-MRE approach operates without the need of δ-shifted repetitions.

3.1 Concept of multiphase DENSE-MRE acquisition

The multiphase DENSE-MRE approach enables the acquisiton of all phase offsets at once, thus repeated sequence execution are not necessary for fully sampling the wave motion. Due to the stimulated echo imaging, the motion encoding for a series of wave sampling points can be performed within one TR. This is achieved as follows:

In DENSE-MRE, the longitudinal magnetization gets prepared at a distinct time point in relation to the mechanical excitation wave by the first MEG G_1. The following readout part decodes the prepared magnetization and thereby encodes the displacement information into the MR phase signal via the second MEG G_2. In the previous Chapter 2.3.7, this was explained with the use of three 90° RF pulses – two for the preparation part and one for the readout part. However, in stimulated echo imaging it is not required to use 90° pulses, in fact, also lower flip angles are feasible [104]. By reducing the flip angle of the readout block RF pulse, a part of the prepared longitudinal magnetization remains. This remaining prepared magnetization is further used for a subsequent readout block. This concept enables utilizing of a series of readout blocks – one readout block for each desired phase offset of the motion.

A detailed description of the motion encoding concept provide the next sections. However, the schematic is already depicted in this section. For the acquisition of four wave sampling points, Figure 3.1 shows the according schematic sequence diagram and clarifies dependencies of RF pulses and MEGs as well as readout blocks and relations to the wave motion.

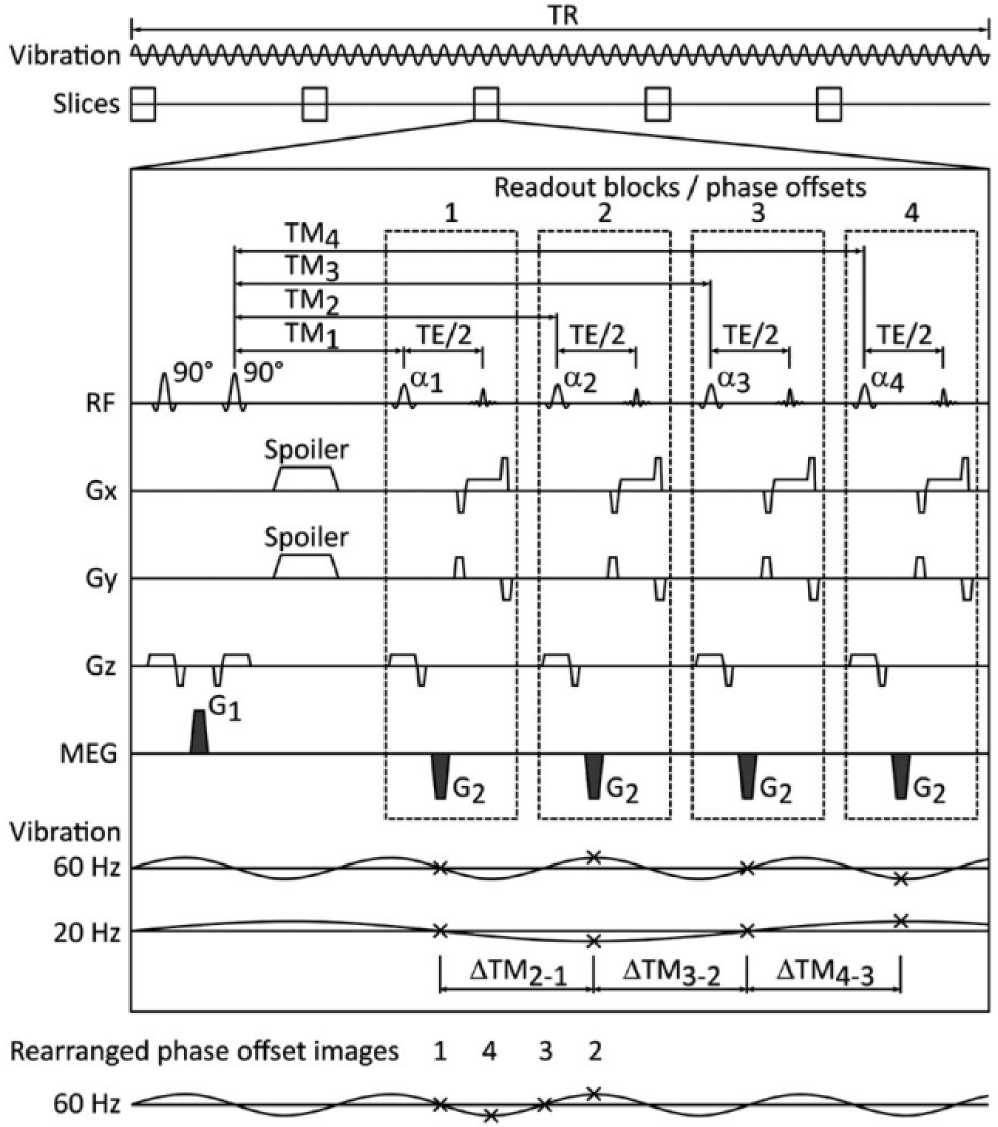

Figure 3.1: Schematic sequence diagram, showing one TR of the multiphase DENSE-MRE approach. Explanations are given in the text of the following sections. (from [109])

3.2 Readout blocks and MEGs

A set of N readout blocks is utilized in the sequence ($N = 4$ in Figure 3.1). Each i^{th} block consists of an RF pulse, an MEG G_2 and imaging gradients for slice selection, phase encoding and readout. At a particular mixing time TM_i, the i^{th} readout block occurs. Within each readout block, at $\frac{TE}{2}$ after the flip angle α_i, the stimulated echo is recorded. During $\frac{TE}{2}$, between the imaging gradients, the MEG is inserted which matches the condition $G_2 = -G_1$. The duration τ and amplitude G_2 of the MEG – and thus the gradient moment $m_{G_2} = \int_0^\tau G_2 dt$ – control the efficiency of the motion encoding. As the motion, generated by the mechanical excitation, is limited due to patient comfort, a trade-off between the gradient moment and the intensity of mechanical excitation has to be found to allow proper wave motion encoding. Higher MEG moments result in higher encoding efficiencies and allow decreasing the excitation motion amplitude. But, an increased MEG moment can also lead to longer MEG durations, which also affects the minimum feasible TE. Hence, short TEs can be applied using a short MEG.

3.2.1 MEG time points – TM series

Each MEG pair G_1 and $G_{2,i}$ encodes a snapshot of the wave motion pattern. Crucial for the correct multiphase acquisition are thereby the time points, when the second MEGs $G_{2,i}$ are switched on, as they define the sampling points of the excitation wave motion. Hence, only $G_{2,i}$ are shifted in relation to the excitation motion, whereas G_1 is fixed. In contrast, in conventional MRE and singlephase DENSE-MRE both of the MEG parts G_1 and G_2 are shifted in relation to the motion by an offset δ. However, in the multiphase approach δ is fixed and the wave sampling points are realized by shifts in Δt in Equations (2.32) and (2.33). For an equidistant sampling of the full excitation wave period (T_u), the sampling point interval ΔT_u is given as:

$$\Delta T_u = \frac{T_u}{N}. \tag{3.1}$$

Hence, the Δt_i shifts are given as:

$$\Delta t_i = \Delta t_0 + (i-1)\Delta T_u = \Delta t_0 + (i-1)\frac{T_u}{N}, \tag{3.2}$$

with N as the number of sampling points ($i = 1..N$) and an arbitrary additional offset Δt_0 (units s) between G_1 and $G_{2,i}$.

In the multiphase DENSE-MRE acquisition, the Δt shifts are realized via a series of mixing times. The desired $G_{2,i}$ time points arise within the related readout block. To define the TM series, the differences ΔTM between subsequent readout blocks have to match the sampling point interval:

$$\Delta TM = \Delta T_u = \frac{T_u}{N} \tag{3.3}$$

and the TM series reads:

$$TM_i = TM_1 + (i-1)\Delta TM = TM_1 + \Delta t_i - \Delta t_0 = TM_1 + (i-1)\frac{T_u}{N}. \tag{3.4}$$

The first TM_1 is thereby chosen in due consideration of the motion reference point or sequence parameter aspects. Figure 3.2 clarifies the relations of the timings.

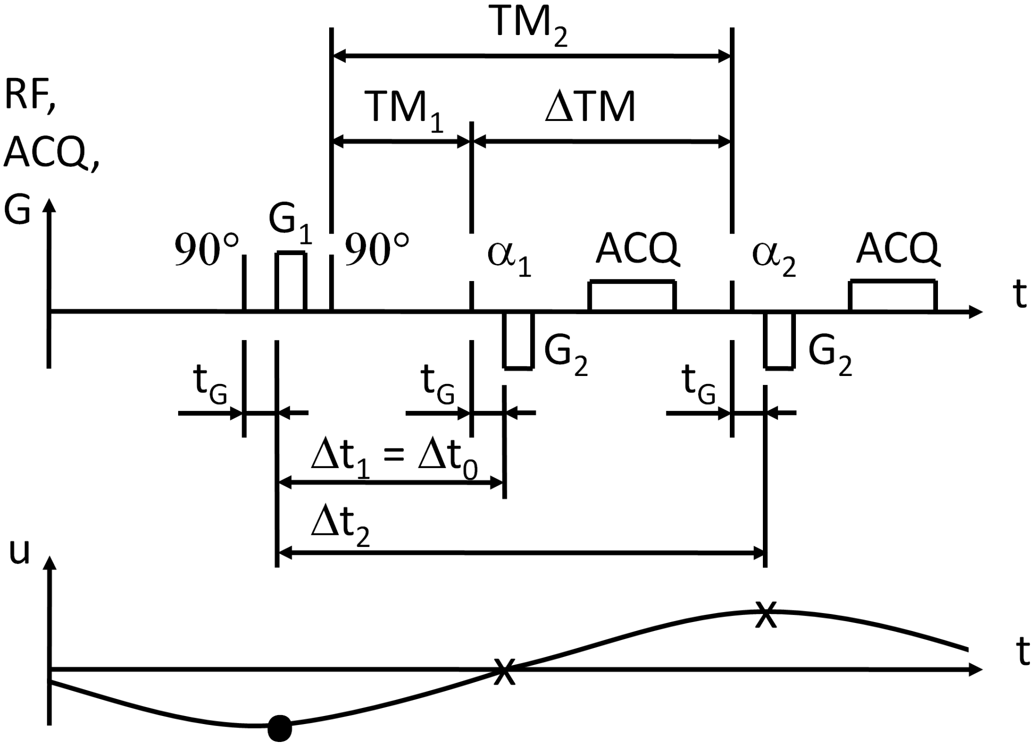

Figure 3.2: Illustration of the sequence and MEG timings in multiphase DENSE-MRE.

3.2.2 Encoded wave motion – Encoding efficiency

Motion encoding in multiphase DENSE-MRE follows the same principles as described in general in Chapter 2.3.1 as long as no constraints in the MEG timings have been applied. Hence, Equations (2.32) and (2.33) also describe Φ_1 and $\Phi_{2,i}$. The MEG timings are defined by the TM series from Equation (3.4). Inserting $\Delta t_i = TM_i - TM_1 + \Delta t_0$ in Equation (2.33), the equations for Φ_1 and $\Phi_{2,i}$ read as:

$$\Phi_1 = \frac{\gamma G_1 r_0}{\pi f_u} \sin(\pi f_u \tau) \sin(\pi f_u \tau + \delta), \tag{3.5}$$

$$\begin{aligned}\mathit{\Phi}_{2,i} &= \frac{\gamma G_2 r_0}{\pi f_u}\sin(\pi f_u \tau)\sin(\pi f_u \tau + 2\pi f_u \Delta t_i + \delta) \\ &= \frac{\gamma G_2 r_0}{\pi f_u}\sin(\pi f_u \tau)\sin(\pi f_u \tau + 2\pi f_u (TM_i - TM_1 + \Delta t_0) + \delta),\end{aligned} \tag{3.6}$$

with the excitation frequency f_u. The full motion encoded phase for each i^{th} readout block results from summing up $\mathit{\Phi}_i$ and $\mathit{\Phi}_{2,i}$ and inserting $G_2 = -G_1$:

$$\begin{aligned}\mathit{\Phi}_i &= \mathit{\Phi}_1 + \mathit{\Phi}_{2,i} \\ &= \frac{\gamma G_1 r_0}{\pi f_u}\sin(\pi f_u \tau)\left[\sin(\pi f_u \tau + \delta) - \sin(\pi f_u \tau + 2\pi f_u \Delta t_i + \delta)\right] \\ &= \frac{\gamma G_1 r_0}{\pi f_u}\sin(\pi f_u \tau)\left[\sin(\pi f_u \tau + \delta) - \sin(\pi f_u \tau + 2\pi f_u (TM_i - TM_1 + \Delta t_0) + \delta)\right]\end{aligned} \tag{3.7}$$

With these equations, the encoding efficiency of the acquisition approach is derived. Firstly, as $\mathit{\Phi}_1$ is constant over all phase offsets, its contribution to the remaining wave encoding efficiency vanishes for all phase offsets. Thus, only $\mathit{\Phi}_{2,i}$ have to be considered. Secondly, returning to Equation (3.6), also other terms are constant over all phase offsets. In particular:

$$\mathit{\Phi}_{2,i} = \frac{\gamma G_2 r_0}{\pi f_u}\sin(\pi f_u \tau)\sin(\pi f_u \tau + 2\pi f_u \Delta t_i + \delta) = A\sin(B + 2\pi f_u \Delta t_i), \tag{3.8}$$

with $A = \frac{\gamma G_2 r_0}{\pi f_u}\sin(\pi f_u \tau) = constant$ and $B = \pi f_u \tau + \delta = constant$. To reach the maximum phase $\mathit{\Phi}_{max}$, the sine-term describing the phase offset relation $\sin(\pi f_u \tau + 2\pi f_u \Delta t_i + \delta)$ is set to its maximum magnitude of 1. Hence, the encoding efficiency for the multiphase DENSE-MRE $E_{0,mp}$ is derived as:

$$E_{0,mp} = \frac{\mathit{\Phi}_{max}}{r_0} = \frac{\gamma G_2}{\pi f_u}\sin(\pi f_u \tau). \tag{3.9}$$

and holds for all phase offsets.

3.3 Sequence optimization

To achieve a balanced image quality along the phase offset series and reduce image artefacts, optimizations of sequence aspects have been included into the multiphase acquisition approach. On the one hand, a variable flip angle scheme for the RF pulses aims for constant signal intensities and on the other hand spoiling techniques reduce residual signals between the phase offsets.

3.3.1 Variable flip angle scheme

In the series of multiple readouts, the available longitudinal magnetizations in the beginning of each readout block have different magnitudes. Although the encoding efficiency of the motion encoding into the signal phase is not influenced by the different magnetization magnitudes, the noise in the images is affected. Depending on the T1 relaxation, different signal intensities in the magnitude images of the subsequent readout blocks occur. Thus, the signal-to-noise ratio (SNR) within the magnitude images decreases over the wave sampling points. This fact also influences the phase images, since the noise in a phase image is related to the inverse of the corresponding voxel magnitude SNR within the magnitude images [105]:

$$\sigma_{phase} = \frac{1}{SNR_{mag}}. \tag{3.10}$$

Hence, along subsequent readout blocks, the noise in the phase images increases. As a result the phase measurements might be prone to errors, in areas with low magnitude image SNR. To tackle this problem, different flip angles α_i for the different readout blocks i can be applied. A variable flip angle concept known from single shot stimulated echo imaging [118] was implemented into the sequence. In this variable flip angle approach, the flip angles increase during the sequence progression up to 90° to fully use the available longitudinal magnetization [118]. A series of N flip angles can be calculated recursively starting with the last flip angle $\alpha_N = 90°$ as follows [118]: The signal S_i for the i^{th} readout is given by:

$$S_i = M_i \sin(\alpha_i), \tag{3.11}$$

with the current longitudinal magnetization M_i. The remaining longitudinal magnetization is available for the next readout block but decreased by the T1 relaxation over the elapsed time ΔTM:

$$M_{i+1} = M_i \cos(\alpha_i) e^{\left(-\frac{\Delta TM}{T1}\right)}. \tag{3.12}$$

By increasing the index and getting S_{i+1} from Equation (3.11), rearranging and substituting M_i and M_{i+1} into Equation (3.12), a relation between subsequent signals can be obtained:

$$\frac{S_{i+1}}{S_i} = \frac{\sin(\alpha_{i+1})}{\tan(\alpha_i)} e^{\left(-\frac{\Delta TM}{T1}\right)}. \tag{3.13}$$

Since the signal intensities shall be the same within all readout blocks, hence $S_{i+1} = S_i$, an equation for the flip angle series can be found:

$$\alpha_i = \arctan\left(\sin(\alpha_{i+1})\right) e^{\left(-\frac{\Delta TM}{T1}\right)}. \tag{3.14}$$

To obtain a set of flip angles via Equation (3.14), a value for the tissues T1 relaxation time has to be assumed. For the brain investigations at 3 T, a mean T1 relaxation time for white matter of T1=800 ms [119, 120, 121] was chosen. The time differences between the subsequent readouts resulted from the sampling points of the 20 Hz excitation and were set to be $\Delta TM = 12.5\,ms$ for all i. The calculated four flip angles were rounded up to the next integers as $\alpha_{series} = [30°, 35°, 45°, 90°]$.

3.3.2 Spoiling schemes

The RF pulse within a readout block tips the prepared magnetization vector with a defined flip angle α_i from the longitudinal axis to get a projection onto the transverse plane and allow the image acquisition. However, the acquisition process does not automatically crush the transverse magnetization afterwards. Residual transverse magnetization after a readout block can still exist and can negatively affect the measured signal during the subsequent readout blocks. Without further manipulation, the residual transverse magnetization would only decay with the relaxation rate T2, which can be insufficient when the time intervals between the readout blocks (ΔTM) are short. To tackle this issue and allow short ΔTM intervals, the issue was considered analogous to other rapid imaging sequences utilizing short TRs. Hence, spoiling concepts used in GRE imaging [122, 123, 124] and also single-shot stimulated echo imaging [118] were implemented into the multiphase DENSE-MRE scheme.

To minimize the influence of one readout block on the following blocks, the remaining transverse magnetization vector after the acquisition can be destroyed at the end of each readout block. This can be achieved via an additional magnetic field gradient – a spoiling gradient – which forces the transverse magnetization to dephase [96]. Subsequent readout blocks can thus start earlier. Spoiling gradients are therefore implemented on the readout-axis at the end of each readout block. Additionally, the phase encoding gradients are rewound after each echo acquisition [96].

Another, even better spoiling concept is RF spoiling [96]. Undesired coupling between rapid consecutive readout blocks in multiphase DENSE-MRE was thus further suppressed via RF spoiling. Thereby a phase coherence between the RF pulse and the measured signal echo is ensured by a particular phase position for each couple of RF pulse and echo acquisition. The applied additional phase from the RF pulse is then shifted back in the data after acquisition. From one readout block to the next, the applied phase of the RF pulse is altered incrementally by 50°, which is one typical spoiling increment used in spoiled GRE imaging [124, 125].

In addition to the spoiling of the remaining transverse magnetization of each readout block, the magnetization after the preparation part has also to be considered. Imperfections in the two 90° RF pulses can lead to a remaining transverse magnetization during the mixing time and in general, the two RF pulses generate a spin echo (Chapter 2.3.7.1). Both effects are undesired in the multiphase DENSE-MRE acquisition. Hence, spoiler gradients were applied after the second RF pulse on the readout and phase encoding axes. The motion encoding is thereby unaffected, as these spoilers only influence the transverse magnetization and not the longitudinal magnetization.

3.4 Post-processing

The acquired series of phase offset images contains the time-resolved wave propagation information. To obtain proper wave images from this acquired dataset, several post-processing steps have to be performed. As a first step in phase image processing, rescaling of the data has to be performed. As the data in the DICOM files is stored as integer numbers, the phase images are linearly rescaled to radians using rescale slope a and rescale intercept b entries from the DICOM header:

$$\varPhi_{rad} = a\varPhi_{int} + b. \tag{3.15}$$

The phase data now ranges from $-\pi$ to π and further processing steps can be applied. Before the dataset can be input to the wave inversion algorithm, additional processing steps can be necessary, which are described in the following.

3.4.1 Phase offset rearrangement

The phase offsets are imaged using a series of readout blocks synchronized to the desired sampling points of the excitation wave. One strategy is to synchronize each of them in chronological order as they appear on the wave time course. The readout blocks are then separated by ΔTM which equals the sampling interval ΔT_u. However, several imaging parameters and accompanied pulse and gradient durations define how long one readout block lasts. As a result the necessary time of one readout block can be longer than the intervals between the sampling points ΔT_u within one excitation wave period according to the chosen excitation frequency. Shifting the subsequent readout blocks by adding integer multiples of the wave period repeatedly to the later elements in the TM series would allow reaching the recurring sampling points of the harmonic excitation (Figure 3.3a). But, this can lead to long latency between the readout blocks coupled with an unnecessarily prolonged runtime performance of the sequence. An optimization can be obtained by a chronologically independent phase offset sampling arrangement (Figure 3.3b).

According to the excitation frequency f_u, the used TM series TM_i inherently defines the reordering scheme R:

$$R_i = ((TM_i - TM_1)f_u N)\,mod\,(N) + 1 \tag{3.16}$$

for each i^{th} of the N phase offsets.

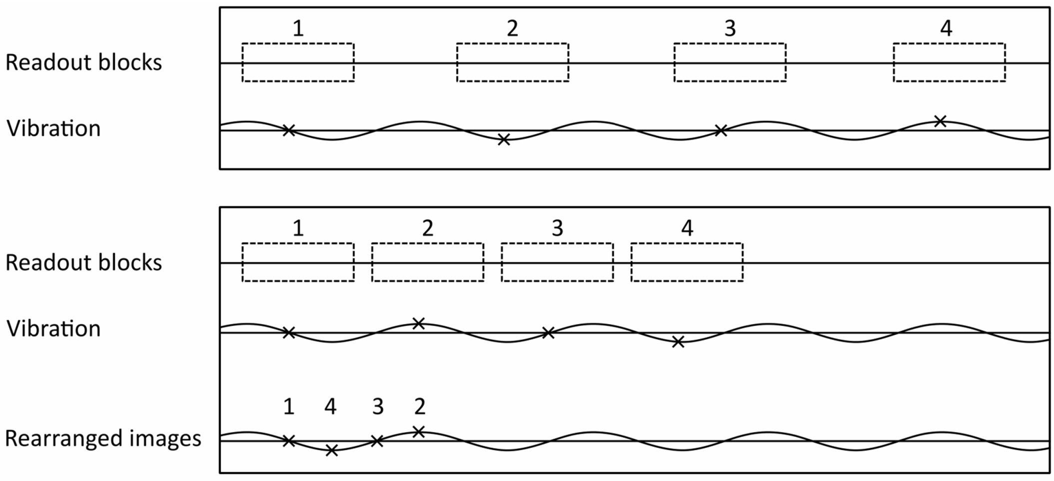

Figure 3.3: Illustration of the phase offset rearrangement concept for acquiring four sampling points (marked as X) of the vibration wave. (a) Strict chronological order of the phase offset acquisition can lead to prolonged gaps between the readout blocks. (b) Scanning efficiency is increased with an optimized phase offset acquisition order.

3.4.2 Background phase

The encoded motion signal in the phase offset images is described by Equation (3.7). At an arbitrary wave motion time point, the preparation part of the sequence generates a phase value Φ_1. Hence, Φ_1 contributes to all of the acquired phase images. Since the preparation part is the same for all readout blocks, Φ_1 arises as a constant additional offset along the time axis. This offset from the baseline – the direct current (DC) offset – can be eliminated via subtraction of the mean value of a voxel over time. Thus, only the time dependent – the alternating current (AC) – phase information remains in the images (Figure 3.4).

Mathematically, eliminating the baseline offset by subtracting the mean equals discarding the DC bin of the Fourier transformed signal. As described previously in Chapter 2.4.2, a Fourier transform is typically performed to pick the excitation frequency bin and to discard other temporal frequencies including DC. However, in certain cases it is beneficial to perform background phase elimination first. For one, the waves are revealed and become clearly visible within the images and spatial filtering can then be performed on the wave images. A further significant benefit arises with respect to phase wraps. If the images

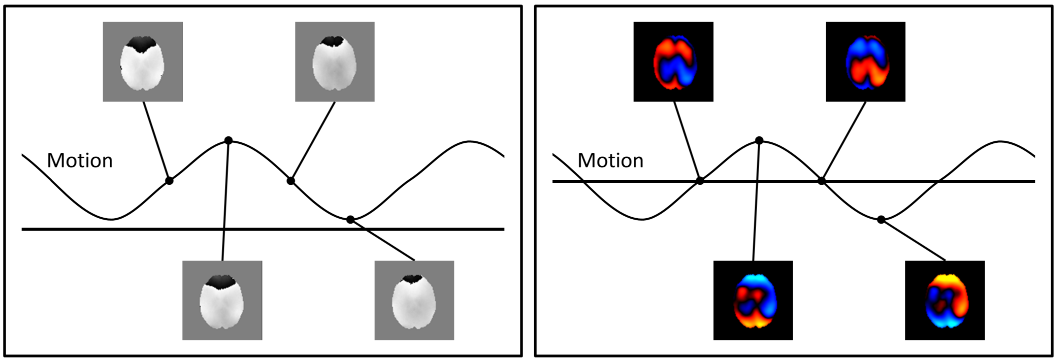

Figure 3.4: Elimination of the baseline offset in multiphase DENSE-MRE acquisitions reveals the wave motion.

contain phase wraps, during Fourier transform for the first harmonic extraction, image artifacts will possibly be magnified. Hence, performing the DC subtraction prior and in the complex domain by Equation (3.17), as recommended for phase difference reconstructions [96], can reduce the phase wrap problematic. Thus, even if there were a few phase wraps in the initial images, the wraps could vanish and further phase unwrapping could be omitted. To eliminate the background phase, the phase offset image series is thus processed by:

$$\varPhi_{i,AC} = \arctan\left(e^{(i\varPhi_i)} e^{(-i\varPhi_{DC})}\right) \tag{3.17}$$

with $\varPhi_{DC} = \frac{1}{N}\sum_{i=1}^{N}(\varPhi_i)$. Hence, the AC part $\varPhi_{i,AC}$ remains in the dataset.

Chapter 4

Phantom investigations with multiphase DENSE-MRE

Parts of this chapter have been published in Strasser J. et al., Magn Reson Med. 2019;81(6):3578-3587 [109] and Proc. ISMRM 2017 (1370) [107].

To test the new MRE acquisition technique, phantom experiments were performed. Investigations were done using the novel multiphase DENSE-MRE approach and validated with acquisitions using the singlephase DENSE-MRE scheme and also with a conventional GRE-MRE sequence. To perform an MRE test experiment and investigate the materials viscoelasticity, a suitable phantom which fulfills several requirements is essential. On the one hand, there are general requirements of MR compatibility and signal sensitivity for such phantoms. And on the other hand, specifically for MRE, the phantoms have to be of soft material which is sufficiently viscoelastic to allow wave propagation through the phantom. Over the years, different phantom materials have been investigated for MRE by researches worldwide. Most commonly, phantoms were made out of agar [13, 24, 74, 103], gelatin [126, 127, 128, 129] or combinations of both [130]. But also other available materials amongst pudding, jam or tofu were tested as MRE phantoms [131]. Custom made phantoms based on gels however allow preparing phantoms with stiffness ranges comparable to soft tissues. Additionally, the custom preparation allows manufacturing homogeneous as well as heterogeneous phantoms with specific inclusion properties. Several phantoms were thus built for various experimental aspects.

4.1 Preparation of agar phantoms

Soft agar phantoms were prepared for the experiments using various agar/water concentrations. The agar powder was dissolved in distilled water and heated up. The resulting liquid gel was further poured into containers and cooled down in the fridge. To avoid contamination, the containers were sealed airtight. Two types of agar powders were used.

For the larger phantom, Agar-Agar Kobe I (Carl Roth GmbH + Co.KG, Karlsruhe, Germany) was used. The smaller phantom was built using Electran DNA grade agarose (VWR International BVBA, Leuven, Belgium). Several phantom preparation tests were performed to find agar/water concentration ratios which results in a gel block with suitable stiffness values appropriate for MRE tests. To achieve mechanical waves at the used excitation frequencies that develop several wavelengths within the geometrical dimensions of the phantoms, the agar gel block was manufactured as soft as possible.

The heterogeneous phantoms (Figure 4.1), which include stiffer embeddings (higher agar concentration (Table 4.1)) in a bulk soft-surrounding gel matrix were manufactured in several steps. First, the bottom bulk layer was built in the phantom's container and cooled down to gelatinize. In next steps, the inclusion gel blocks were separately built in different small boxes with various geometrical shapes. One box and one cylinder were used with individual lengths. The gelatinized inclusions were then uncased and put in place onto the already prepared bottom layer within the container of the phantom. Further, the container was filled up with bulk solution to finalize the heterogeneous phantom. For the small phantom, a stiff rectangular container and for the large phantom a deformable conical container was used. In the larger phantom, the bulk material filling was done in three subsequent steps. Thereby, the already ongoing gelatination of the previous layers has resulted in interfaces between them which can be seen in the T2 weighted images (Figure 4.1b).

Table 4.1: Used agar powder and concentrations of the bulk material and inclusions in the constructed phantoms ($\% \mathrel{\hat{=}}$ g agar/1000 ml water).

Phantom	**Agar**	**Bulk matrix**	**Box inclusion**	**Cylinder incl.**
Small	Electran DNA grade agarose	0.3 %	0.6 %	0.6 %
Large	Agar-Agar Kobe I	0.9 %	1.3 %	1.1 %

4.2 Mechanical excitation

The investigations were performed using the piezoceramic mechanical excitation device with the head rocker as described in Chapter 2.2.3. The phantom was placed within the head rocker and fixated with foam material for good mechanical coupling.

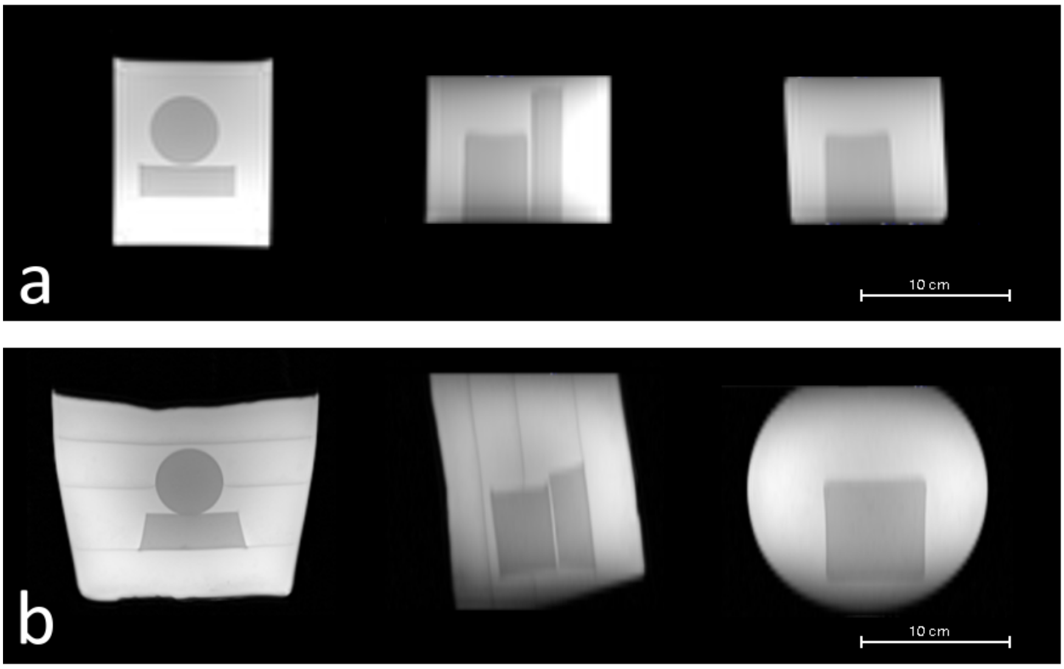

Figure 4.1: T2 weighted images of the small phantom (a) and the large phantom (b). Presented are transversal, sagittal and coronal cross-sectional slices, in the left, center and right column, respectively. T2 weighting produced a different contrast of the inclusions with higher agar concentrations compared with the surrounding bulk material.

4.3 Multiphase acquisition

The small phantom was investigated with the new multiphase DENSE-MRE sequence. In these experiments, an excitation frequency of 60 Hz together with the sequence parameters presented in Table 4.2 were used. The variable flip angle scheme was incorporated with increasing flip angles over the four readout blocks.

Table 4.2: Multiphase DENSE-MRE parameters – wave sampling in the small phantom.

Parameter	**Settings**
FOV	300x300 mm^2
Matrix	128x128
Slice thickness	4 mm
Slices	5
MEG amplitude	34 mT/m
MEG duration	0.7 ms
α-series	[30 °, 35 °, 45 °, 90 °]
TR	2500 ms
TE/2	3.8 ms
TMs	[8, 20.5, 33, 45.5] ms
Phase offsets at	[0, 12.5, 25, 37.5] ms
Parallel imaging	GRAPPA factor 2
Partial Fourier	6/8
TA	2 min 30 s

The used TM series led to an acquisition of the four phase offsets in an disordered way in the first place. A chronologically ascending order was achieved according to Equation (3.16) by sorting the phase offsets from image number [1, 2, 3, 4] to [1, 4, 3, 2]. The image rearrangement was performed prior to the first harmonic extraction.

In Figure 4.2, the phantom images acquired with multiphase DENSE-MRE and motion encoding in z-direction are shown. Over the four time steps, the magnitude image intensities are alike, as a result of the variable flip angle approach (Figure 4.2a). Figure 4.2b,c show the corresponding phase images at the applied TM time points in the acquired and rearranged order. In the raw phase images, wave displacements are already observable, but the waves are superimposed with background phase and also phase wraps are present (Figure 4.2b-c). The encoded sine motion can be seen in the phase values of a voxel over time and the background phase produces an additional offset in the phase values (Figure 4.3). Elimination of the background phase led to clear visibility of the waves in the images (Figure 4.4). In this process, also the few phase wraps vanished (Figure 4.4b). The full wave motion was imaged in three separate acquisitions with switched MEG axis. The obtained images after first harmonic extraction are shown as real parts of the complex wave images for the three motion encoding directions in Figure 4.5.

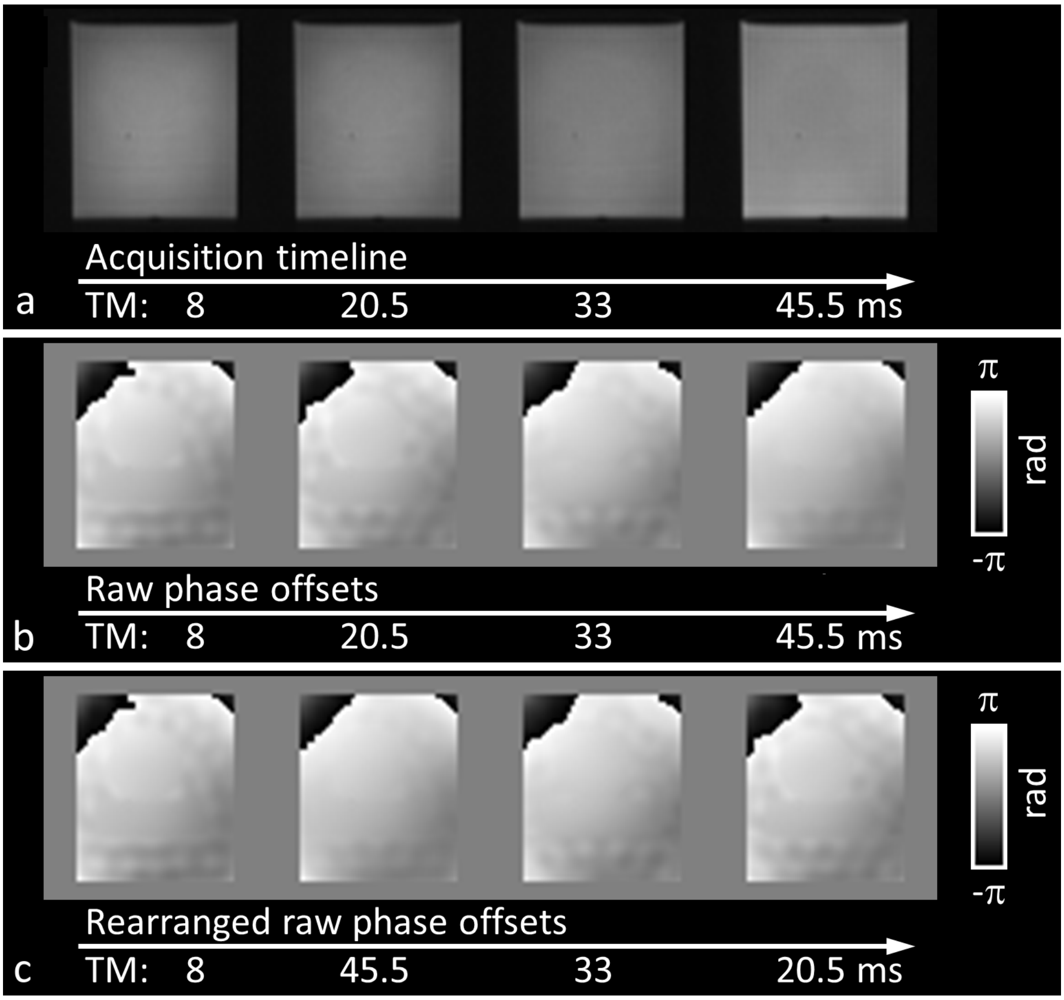

Figure 4.2: Phase offset images in one slice of the mutliphase DENSE-MRE phantom acquisition with z-motion encoding. The magnitude images (a) and corresponding phase images (b) are arranged according to the acquisition timeline. Rearranging of the phase offsets offers a chronological order corresponding to the wave motion (c). (modified from [109])

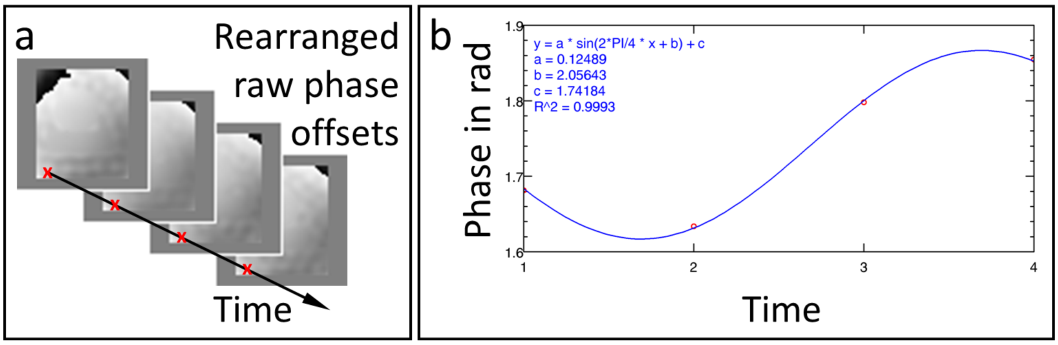

Figure 4.3: Visualization of the encoded sine motion and background phase over the phase offsets. (a) depicts the four phase offsets of one slice. The red crosses in the images in (a) indicate the voxels plotted over time in (b). (from [109])

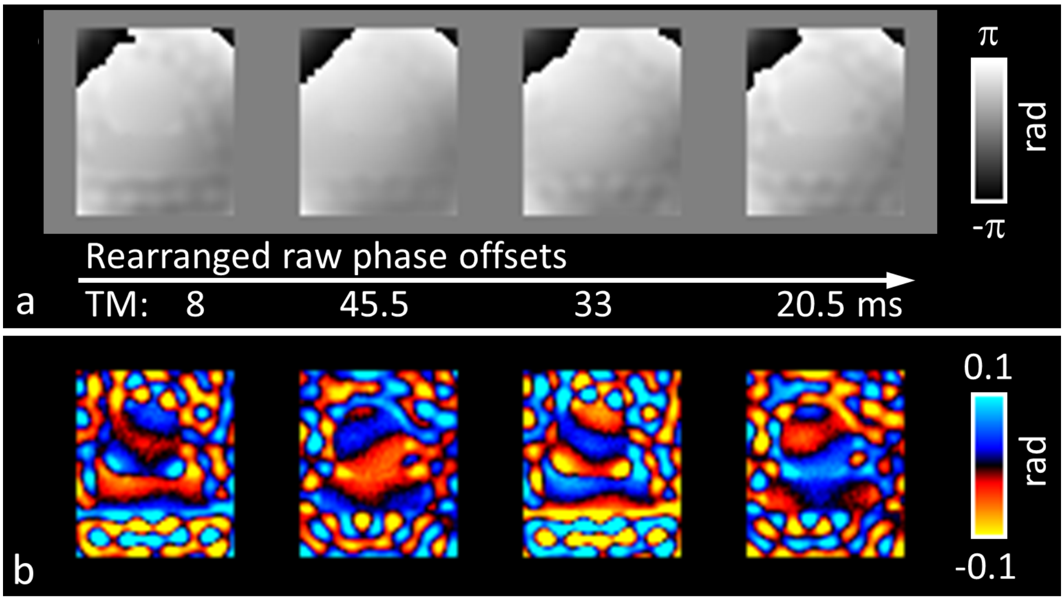

Figure 4.4: Rearranged raw phase offset images (a). The waves showed up clearly after removal of the background phase (b). (modified from [109])

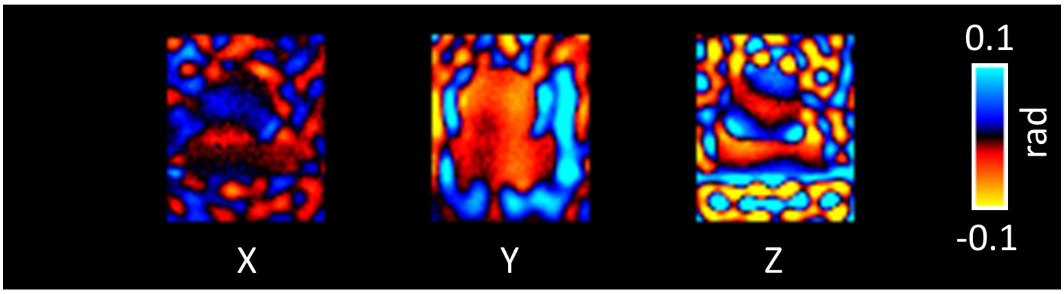

Figure 4.5: Real parts of the complex wave images with motion encoding in x-, y- and z-direction. (modified from [109])

4.4 Multiphase and singlephase acquisitions

To validate the new acquisition approach, experiments have also been performed with singlephase DENSE-MRE. Thereby, the four phase offsets were acquired in separate consecutive singlephase acquisitions with shifts caused by trigger offsets for the excitation. The sequence parameters of the multiphase acquisitions were slightly modified in these experiments (Table 4.3). Again, a continuous 60 Hz wave excitation was used for the experiments. The motion was encoded in z-direction and the timings of the multiphase and singlephase acquisitions were matched to reach the same sampling points of the mechanical wave and in further consequence comparable wave images.

Table 4.3: Singlephase and multiphase DENSE-MRE parameters – comparative measurements in the small phantom.

Parameter	**Settings**	
FOV	300x300 mm^2	
Matrix	128x128	
Slice thickness	4 mm	
Slices	5	
MEG amplitude	34 mT/m	
MEG duration	0.7 ms	
TR	2500 ms	
TE/2	3.8 ms	
Parallel imaging	GRAPPA factor 2	
Partial Fourier	6/8	
	singlephase	**multiphase**
Number of TMs	1	4
TMs	20.5 ms	[20.5, 33.0, 45.5, 58.0] ms
Phase offsets at	[0, 12.5, 25, 37.5] ms	[0, 12.5, 25, 37.5] ms
α-series	90 °	[30 °, 35 °, 45 °, 90 °]
TA	2 min 30 s	2 min 30 s
Executions	4 (4 phase offsets)	1
Total TA	10 min	2 min 30 s

Motion encoded phase offset images could be gathered with both acquisition approaches. With the multiphase acquisition scheme, the total scan time could be reduced by a factor of four compared with the singlephase acquisitions. One slice of the singlephase acquisitions is shown in Figure 4.6. The same slice acquired using the multiphase approach is presented in Figure 4.7. In each figure, the four raw phase offsets, the images after background phase subtraction and the excitation frequency extracted wave images are depicted. Corresponding line plots show the grey values of the respective voxels. In the singlephase acquisitions, the spatial waves can be seen in all raw phase offsets and the associated line plots (Figure 4.6a). The waves become clearer after eliminating the background phase (Figure 4.6b) and frequency extraction (Figure 4.6c). In the multiphase acquisitions, the wave motion is only present in some of the raw phase offset images (Figure 4.7a). In the third raw phase offset, almost no waves are present, due to the sequence timings of the MEGs G_1 and $G_{2,3}$. This can also be seen in the corresponding line plot. After background field subtraction (Figure 4.7b) and excitation frequency selection (Figure 4.7c), the waves become clearly visibly over all phase offsets. The color coded wave images (Figure 4.6c and Figure 4.7c) indicate a high correspondence between the two acquisition approaches.

In the singlephase acquisitions, the MEGs G_1 and G_2 were separated by half a vibration period $\Delta t = \frac{T_u}{2}$. With these settings, the encoding efficiency of the single phase acquisition was twice the encoding efficiency of the multiphase DENSE-MRE. The by factor two increased phase values can be seen in the scale of the line plots through the motion encoded images when the waves are revealed in Figure 4.6b-c and Figure 4.7b-c.

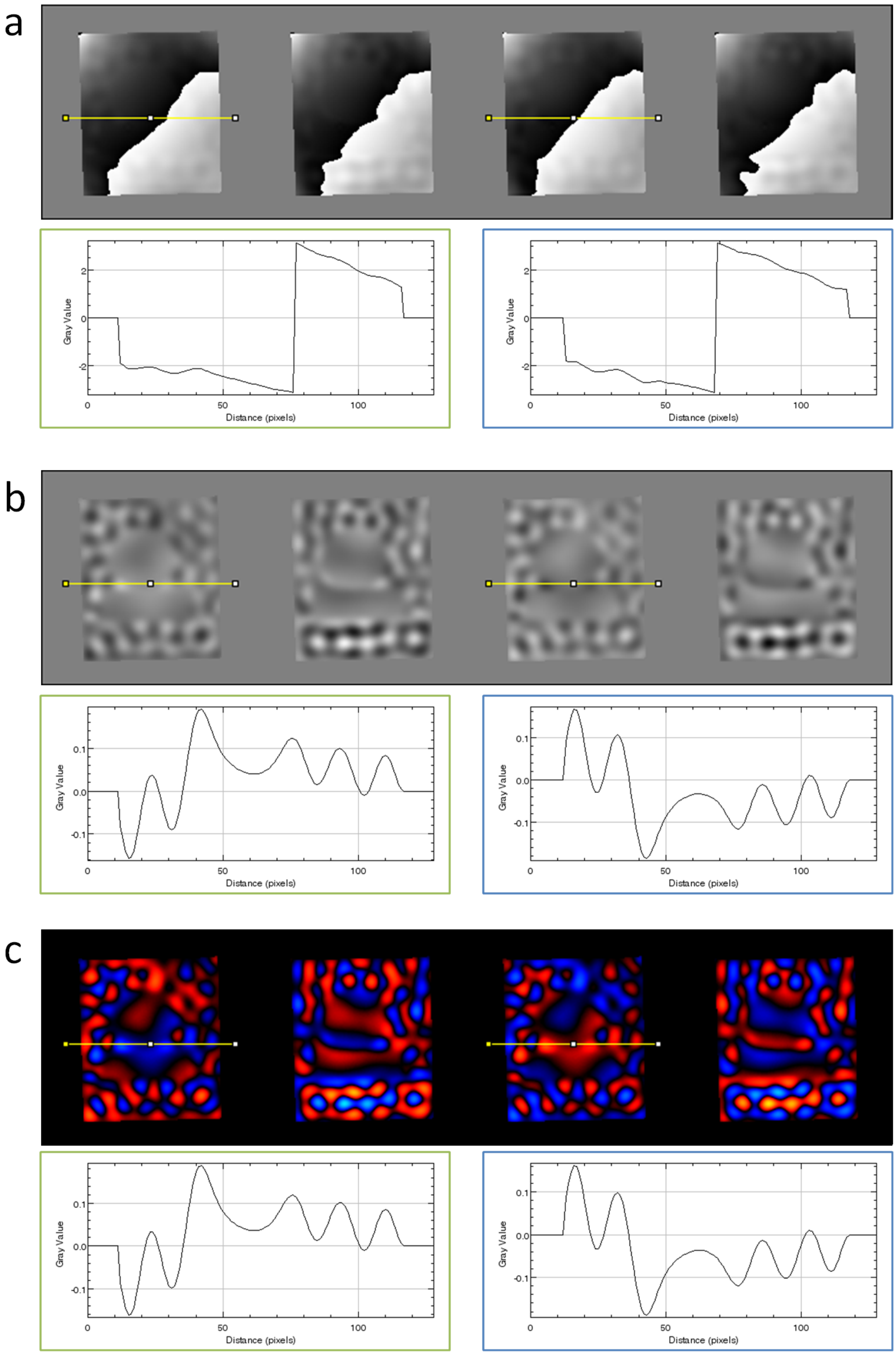

Figure 4.6: Singlephase acquisitions of comparative measurements between singlephase and multiphase DENSE-MRE. (a) Four raw phase offsets. (b) Phase offsets after background elimination. (c) Wave image series after excitation frequency selection. In (a-c), the graphs show the line plots trough the phantom as outlined in the respective image above.

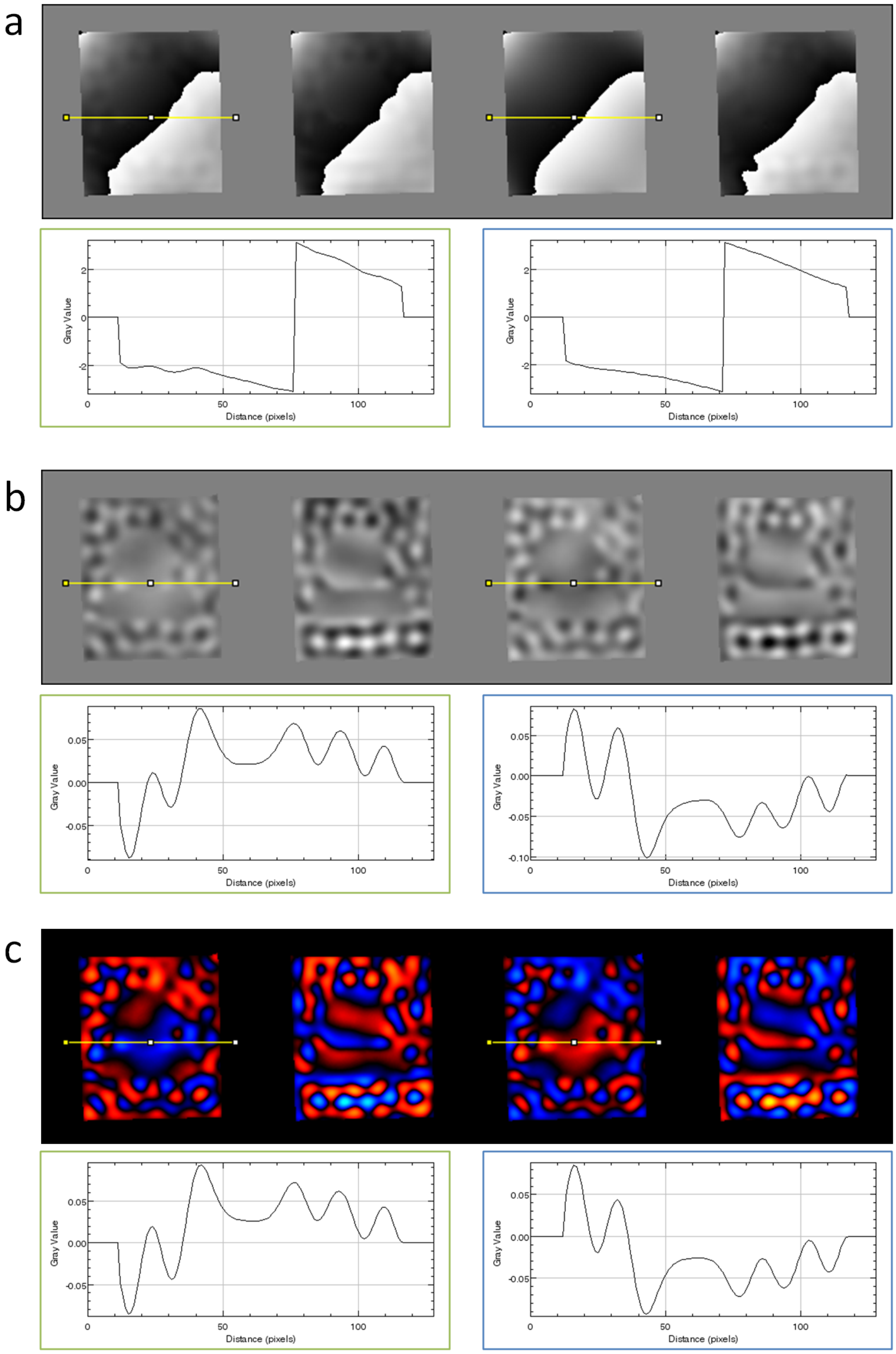

Figure 4.7: Multiphase acquisitions of comparative measurements between singlephase and multiphase DENSE-MRE. (a) Four raw phase offsets. (b) Phase offsets after background elimination. (c) Wave image series after excitation frequency selection. In (a-c), the graphs show the line plots trough the phantom as outlined in the respective image above.

4.5 Multiphase DENSE-MRE and conventional GRE-MRE

To confirm the results from the novel multiphase DENSE-MRE acquisition technique, comparative measurements using a conventional GRE-MRE acquisition technique were carried out. The five slices of the phantom were therefore additionally imaged with a conventional GRE-MRE sequence. This sequence allowed imaging four phase-difference images with z-motion encoding. The phase offsets were realized by delays in the trigger for the excitation device. Every offset was imaged twice with switched MEG polarity and phase-difference images were directly calculated on the scanner. The sequence was executed with identical geometric imaging parameters as used for the multiphase DENSE-MRE acquisition (Table 4.2). Further related imaging parameters are given in Table 4.4.

Table 4.4: GRE-MRE parameters – comparative measurements for validation of the multiphase DENSE-MRE.

Parameter	**Settings**
FOV	300x300 mm^2
Matrix	128x128
Interpolated matrix	256x256
Slice thickness	4 mm
Slices	5
α	23 °
TR	50 ms
TE	22.8 ms
Parallel imaging	GRAPPA factor 2
Partial Fourier	7/8
TA	2 min 12 s

The z-motion encoded datasets were taken as inputs to the MDEV [67] (Chapter 2.4.5) inversion. From the multiphase DENSE-MRE acquisition (data from Chapter 4.3), the x- and y-motion datasets were skipped, since also only z-motion encoded data was available from the GRE-MRE acquisition. The material density was set to $\rho = 1000$ kg/m^3. As part of the inversion, a 2D Gaussian filter with a 5x5 pixel kernel and $\sigma = 1$ pixel reduced noise in the input data and higher wavelengths were minimized by a 2D Butterworth low-pass filter (threshold at 100 m^{-1}). Outliers in the calculated $|G^*|$ and $\angle(G^*)$ maps were removed by means of a 2D median filter (5x5 pixel kernel). The results obtained by both techniques were confirmed by visual inspection of the generated $|G^*|$ and $\angle(G^*)$ maps on the one hand and by assessment of the obtained stiffness values within the stiff inclusions and within the surrounding area on the other hand. To evaluate the shear modulus values of the phantom, regions of interest (ROIs) were defined on the T2-weighted images and copied to the G^* maps. One ROI covered the inclusions with higher agar concentrations in all slices and a second ROI defined the surrounding material. Within the ROIs, mean values for $|G^*|$ and $\angle(G^*)$ were assessed. The phantom T2-weighted images and G^* maps of both MRE acquisitions are shown in Figure 4.8. The box as well as the cylinder inclusion are clearly distinguishable from the surrounding in the G^* maps of both acquisitions (Figure 4.8b-e). The obtained $|G^*|$ and $\angle(G^*)$ maps of the multiphase DENSE-MRE acquisition (Figure 4.8b,c) match well with the ones obtained by GRE-MRE (Figure 4.8d,e).

Mean value assessment of the shear modulus within the ROIs further yielded comparable results between multiphase DENSE-MRE and conventional GRE-MRE (Table 4.5). The $|G^*|$ and $\angle(G^*)$ values were higher in the inclusions than in the surrounding, which fits to the higher agar concentration of 0.6% in the inclusions versus 0.3% in the surrounding.

Table 4.5: Obtained $|G^*|$ and $\angle(G^*)$ values (mean ± SD) within ROIs in the heterogeneous small phantom from the acquisitions using the multiphase DENSE-MRE and a conventional GRE-MRE sequence. (from [109])

	$|G^*|$ **(kPa)**		$\angle(G^*)$ **(rad)**	
	Inclusions	**Surrounding**	**Inclusions**	**Surrounding**
Multiphase DENSE-MRE	4.46 ± 1.48	1.25 ± 0.09	0.64 ± 0.26	0.14 ± 0.09
Conventional GRE-MRE	4.78 ± 1.70	1.24 ± 0.08	0.52 ± 0.30	0.10 ± 0.04

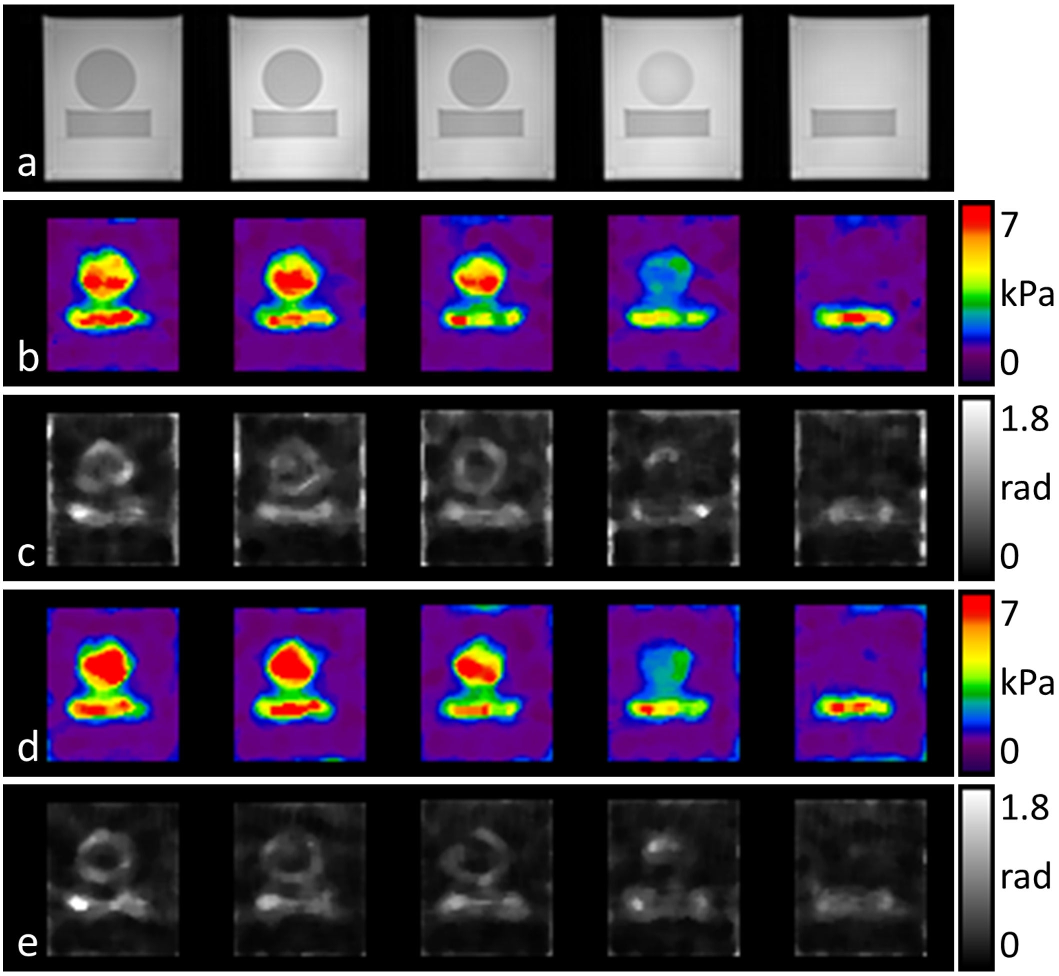

Figure 4.8: Shear modulus maps of the heterogeneous small phantom from the multiphase DENSE-MRE and the conventional GRE-MRE acquisition. (a) T2-weighted images of the five slices in the phantom. (b) $|G^*|$ maps and (c) $\angle(G^*)$ maps from the multiphase DENSE-MRE acquisition. (d) $|G^*|$ maps and (e) $\angle(G^*)$ maps from the conventional GRE-MRE acquisition. (from [109])

4.6 Different excitation frequencies

The large phantom was used to test the multiphase DENSE-MRE acquisition with four phase offsets and motion encoding in z-direction at different excitation frequencies. The acquisition parameters in this experiment were set to achieve a short TA while imaging 15 slices. Various excitation frequencies of 20 Hz, 60 Hz and 100 Hz were used in consecutive acquisitions. For this appropriate combination of frequencies, the TM series of the sequence parameters could be kept unchanged while still matching the sampling points of the mechanical waves. Table 4.6 lists further acquisition parameters.

Table 4.6: Multiphase DENSE-MRE parameters – large phantom with different excitation frequencies.

Parameter	**Settings**
FOV	300x300 mm^2
Matrix	128x128
Slice thickness	5 mm
Slices	15
MEG amplitude	34 mT/m
MEG duration	0.7 ms
α	14°
TR	1000 ms
TE/2	4.7 ms
TMs	[12, 24.5, 37, 49.5] ms
Phase offsets at	[0, 12.5, 25, 37.5] ms
Parallel imaging	GRAPPA factor 2
TA	1 min 16 s

The multiphase DENSE-MRE acquisition scheme allowed imaging the phase offsets for all excitation frequencies with the same sequence parameter settings. In the 20 Hz and 100 Hz acquisitions, the applied TM series led already to a chronological order of the wave sampling points. The images of the 60 Hz experiment were rearranged to achieve a temporally ascending wave sampling order. Complex wave images were obtained for all three excitation frequency experiments. Figure 4.9 shows the measured waves at the different excitation frequencies.

MRE inversion was performed with the wave data of all frequencies combined in the MDEV [67] (Chapter 2.4.5) algorithm. Together with a corresponding T2 weighted image slice, the resulting $|G^*|$ map is shown in Figure 4.10.

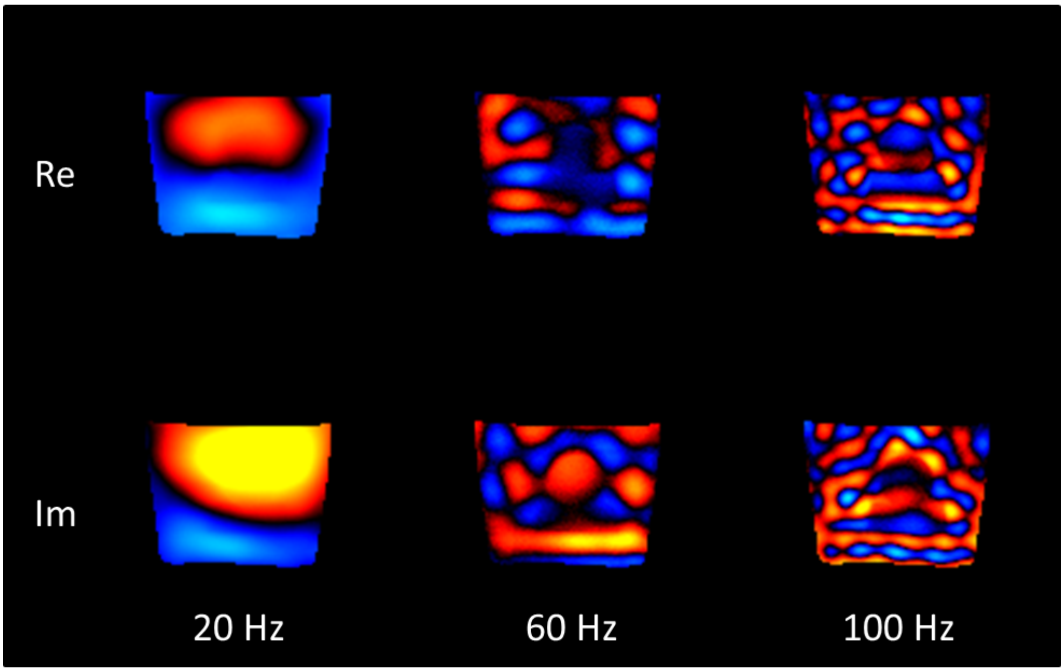

Figure 4.9: First harmonic extracted wave images of one slice within the large phantom at the three excitation frequencies (columns). The top row shows the real parts and the bottom row the imaginary parts of the complex data. (from [107])

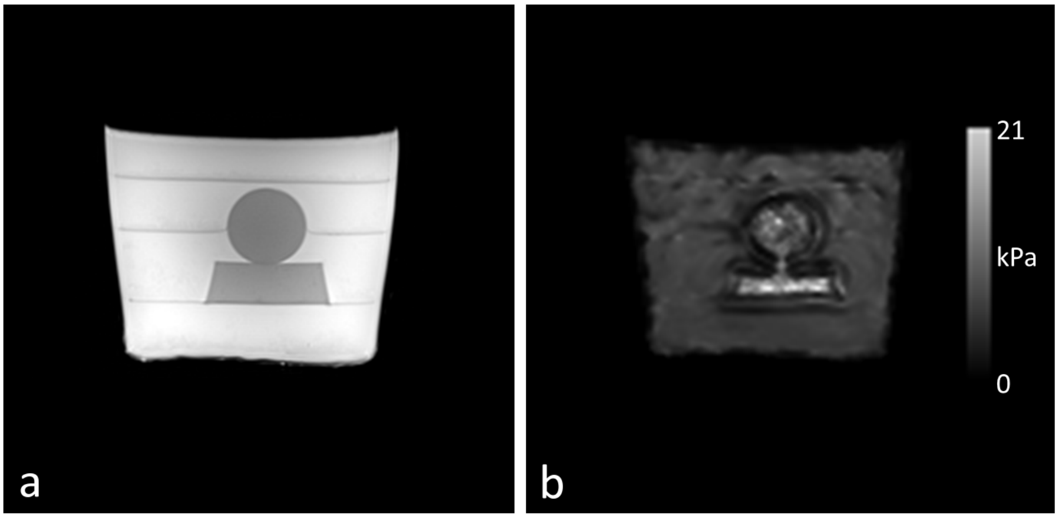

Figure 4.10: One slice of the large phantom. The T2 weighted image (a) shows the inclusions and $|G^*|$ (b) depicts the stiffer material of the inclusions compared with the surrounding bulk material. $|G^*|$ was derived from a combined inversion of the 20 Hz, 60 Hz and 100 Hz wave data. (from [107])

Chapter 5

In vivo brain investigations with multiphase DENSE-MRE

Parts of this chapter have been published in Strasser J. et al., Magn Reson Med. 2019;81(6):3578-3587 [109] and Proc. ISMRM 2018 (2282) [108].

To evaluate the multiphase DENSE-MRE scheme for brain MRE, investigations in four healthy volunteers were performed. The study was approved by the local ethics committee and all subjects gave written informed consent. The male subjects were in the age range of 27-48 years. As an image quality measure, the SNR of the acquired images was determined. The mechanical properties of the human brain tissue in vivo were then assessed in different region of the brain.

5.1 Acquisition and data processing

In the investigations, five transversal slices were acquired using the multiphase DENSE-MRE sequence together with a 20 Hz motion excitation frequency. Besides, T2w images of the same 5 transversal slices were acquired in the brain. The multiphase DENSE-MRE sequence was executed with the parameters given in Table 5.1.

The sampling points of the 20 Hz excitation were reached using the same TM series that also fit to the 60 Hz excitation in the phantom experiments. Hence, the same sequence parameters were used for the 20 Hz in vivo brain acquisition as for the 60 Hz phantom experiment (Chapter 4.3), which also led to the same acquisition time.

5.2 Resulting images and shear modulus assessment

The gathered set of phase offset images was cleaned from background phase. Rearrangement was skipped, as the phase offsets were already acquired in correct order.

Table 5.1: Multiphase DENSE-MRE parameters – in vivo brain investigations.

Parameter	**Settings**
FOV	300x300 mm^2
Matrix	128x128
Slice thickness	4 mm
Slices	5
MEG amplitude	34 mT/m
MEG duration	0.7 ms
α-series	[30 °, 35 °, 45 °, 90 °]
TR	2500 ms
TE/2	3.8 ms
TMs	[8 ms, 20.5 ms, 33 ms, 45.5 ms]
Phase offsets at	[0 ms, 12.5 ms, 25 ms, 37.5 ms]
Parallel imaging	GRAPPA factor 2
Partial Fourier	6/8
TA	2 min 30 s
Executions	3
TA	7 min 30 s

Figure 5.1 shows the magnitude as well as the raw and processed phase images of the z-motion encoded data of one slice within a subject. The upper three rows (Figure 5.1a-c) depict the sampling point timelines at the four mixing times. The magnitude images are shown in Figure 5.1a. 5.1b presents the series of raw phase offsets and the background phase cleaned images are given in Figure 5.1c. Figure 5.1d represents the real parts of the first harmonic complex wave images for all three motion encoding directions x, y and z.

The set of wave images was inverted using the MDEV inversion algorithm [67] (Chapter 2.4.5). Wave data of all three motion encoding directions was input to the algorithm. The cut-off wavenumber of the low-pass Butterworth filter was set to 50 m^{-1} to reduce noise in the input data. $|G^*|$ and $\angle(G^*)$ maps were generated for all slices of each subject. In contrast to the phantom experiments (Chapter 4.5), no further median filtering was applied to the maps. In Figure 5.2, the shear modulus maps of one subject are shown for the five acquired slices.

Mean values of $|G^*|$ and $\angle(G^*)$ were determined in different areas and compared between the four subjects. ROIs were defined using the DENSE-MRE magnitude and T2-weighted images and used to evaluate the values in the shear modulus maps. A global shear modulus assessment was performed in a region defining gray and white matter within all slices. The regions were semi-automatically generated and manually refined. With an intensity threshold on the magnitude images, a mask of the brain contour was predefined. The ventricles were removed from the masks with the help of the T2-weighted images. Additionally to global assessments, $|G^*|$ and $\angle(G^*)$ were assessed in several specific brain regions of white matter and deep gray matter, namely frontal lobes, occipital lobes, centrum semiovale and putamen. These ROIs were defined by hand on the

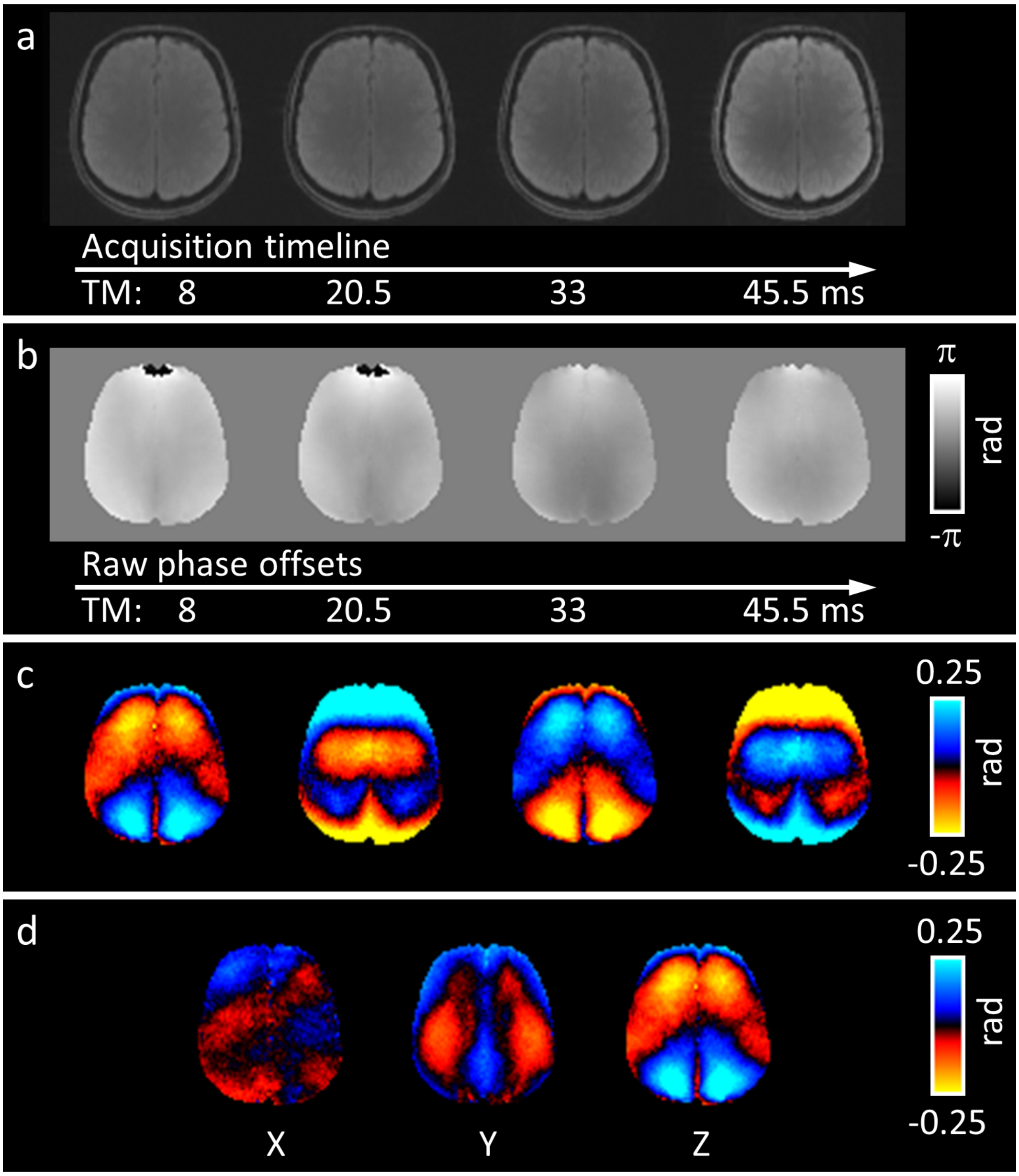

Figure 5.1: Multiphase DENSE-MRE images. Z-motion encoded magnitude (a) and phase (b) images of each time step. Subtraction of the background phase revealed the wave patterns (c). First harmonics (real parts) for all motion components (d). (from [109])

T2-weighted images (Figure 5.3). The defined ROIs were further used for SNR estimation of the multiphase DENSE-MRE acquisitions. For each sampling point, motion component and subject, the SNR (mean divided by standard deviation) of the raw magnitude images was derived individually. The mean SNR for each separate sampling point was calculated afterwards.

Table 5.2 lists the assessed shear modulus values within the different regions of the brain. Image quality and SNR was similar across all subjects with median SNR over the four sampling points of 21.2 (range: 14.2-24.9).

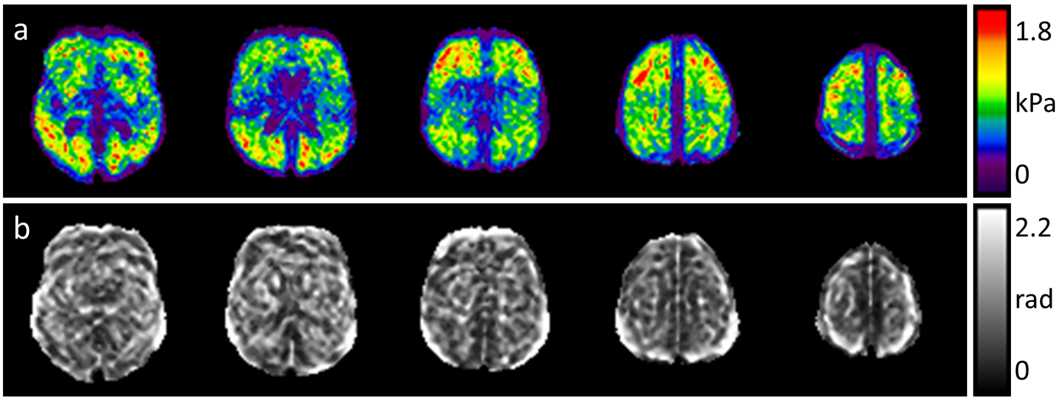

Figure 5.2: Shear modulus maps of five slices within the brain of one volunteer. (a) depicts $|G^*|$ and (b) $\angle(G^*)$ of the complex dataset. (modified from [109])

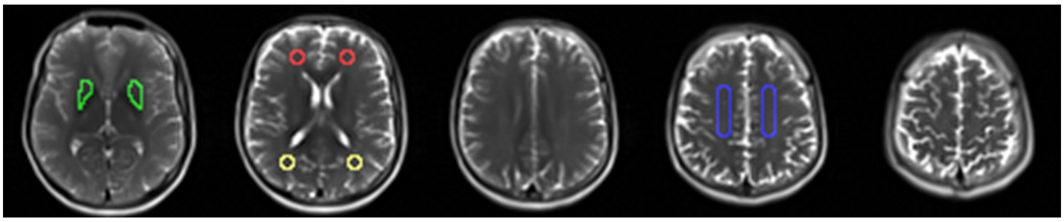

Figure 5.3: T2-weighted images of the same slices as the G^* maps with the used ROIs depicted on the images (putamen (green), frontal white matter (red), occipital white matter (yellow), centrum semiovale (blue)). (modified from [109])

Table 5.2: $|G^*|$ and $\angle(G^*)$ values over the subjects as median (min-max). (from [109])

Region	**$\|G^*\|$ (kPa)**	**$\angle(G^*)$ (rad)**
Global	0.72 (0.64-0.75)	1.03 (0.95-1.07)
Frontal white matter	1.04 (0.96-1.10)	1.01 (0.96-1.26)
Occipital white matter	0.96 (0.90-1.09)	0.95 (0.67-1.15)
Centrum semiovale	0.83 (0.71-1.00)	0.79 (0.71-0.87)
Putamen	0.94 (0.64-1.26)	1.11 (0.97-1.19)

Chapter 6

Multiaxes multiphase DENSE-MRE

Parts of this chapter have been published in Strasser J. et al., Proc. ISMRM 2020 (0170) [110].

The acquisition of the 3D wave motion is a of interest in MRE and especially in brain MRE investigations [52]. Typically, MRE sequences for such an endeavor encode the motion for each of the three orthogonal direction components in three consecutive executions which prolongs the total acquisition time. The multiphase DENSE-MRE acquisition scheme, presented in the previous chapters, allows keeping TA short in general due to the combination of sampling all phase offsets at once together with acquiring a number of slices in an interleaved fashion. The three motion encoding directions however are utilized via three consecutive measurements with switched MEG axis. Thus TA is also prolonged to gather the full 3D wave motion dataset. An acceleration of the multiphase DENSE-MRE scheme was therefore developed which also includes motion encoding on all three orthogonal axes in addition to multiple phase offsets within one TR.

6.1 Concept of multiaxes multiphase DENSE-MRE acquisition

In the multiaxes multiphase DENSE-MRE acquisition scheme, the motion encoding gradients G_1 and G_2 are utilized on all three orthogonal axes in a specific configuration. As in the singleaxis scheme, G_1 is used for preparation and G_2 to finalize the motion encoding at the specific wave sampling points. Again, a series of readout blocks is applied for multiphase sampling, but additionally for multiaxes encoding during each TR. In the multiaxes scheme, the preparation of the magnetization is done with G_1 on all three orthogonal gradient axes at the same time. To encode the motion for each axis, the set of readout blocks is divided into three subsets. One for each encoding direction x, y and z. The time points of G_2 are thereby adjusted in every subset. On one axis,

$G_{2,m,i}$ are applied at the wave sampling points as in multiphase DENSE-MRE. This axis is the current motion encoding axis. The harmonic wave motion is thus acquired as an individual bin in the frequency-spectrum after Fourier transform of the data timeline. In contrast, on the other two axes, the gradients $G_{2,bg,i}$ capture every time an identical point on the wave. This results in a constant background phase in the current subset, making these MEG axes the current background axes. After Fourier transform, their phase contributions appear on the DC bin and can be eliminated during post-processing. The schematic sequence diagram for this concept is presented in Figure 6.1.

Like in the singleaxis multiphase DENSE-MRE, the wave sampling points in the multiaxes concept are defined by a series of TM_i. However, the background sampling points and the subsequent readout blocks with switched motion encoding axis are added to the timing considerations. Thus, the TM_i differ compared to the singleaxis approach. To include the further axes for motion encoding, the TM series increases to a total number M, consisting of three subsets with N entries each. For every subset, the timings of the gradients $G_{2,i}$ within the readout block i are described as follows: The gradients on the two background axes $G_{2,bg,i}$ reach the same point of the excitation wave in all readout blocks at $t_{G_{2,bg,i}}$. On the motion encoding axis however, $G_{2,m,i}$ are applied at the time points $t_{G_{2,m,i}}$, whereby fulfilling the wave sampling concept of one excitation wave period T_u (Chapter 3.2.1, Equations (3.1) and (3.2)). The phase offset shifts are thereby partly incorporated inside the readout blocks which leads to an adaption in the TM series (in contrast to the singleaxis TM_i in Equation (3.4)). Further according to this, TE prolongs dependent on the additional necessary time. The maximum necessary additional time $t_{add,max}$ for incorporating the full phase offset sampling inside the readout blocks is derived by the number of desired phase offsets N (equal to the number of the TM series subset and readout block subset) and the excitation wave period T_u:

$$t_{add,max} = \frac{T_u}{N}(N-1) = \Delta T_u(N-1). \tag{6.1}$$

However, the necessary time $t_{add,max}$ can be reduced by optimizing the time points of $G_{2,bg,i}$ and $G_{2,m,i}$ within the readout blocks. On the background axes, $G_{2,bg,i}$ can appear at an arbitrary time point, as long as they match the same periodic wave time point in all readout blocks. Hence, the $G_{2,bg,i}$ can be centered on the timeline between the first and the last phase offset sampling point. Within the readout blocks, the G_2 ordering can then further either be $G_{2,m}$ first, followed by $G_{2,bg}$ or vice versa. Thus, $t_{add,max}$ can be reduced by the factor 1/2 and the optimized extra time t_{add} becomes:

$$t_{add} = \frac{t_{add,max}}{2} = \frac{T_u}{N}\frac{(N-1)}{2} = \Delta T_u \frac{(N-1)}{2}. \tag{6.2}$$

This optimization is also included in the illustrated sequence schematics in Figure 6.1.

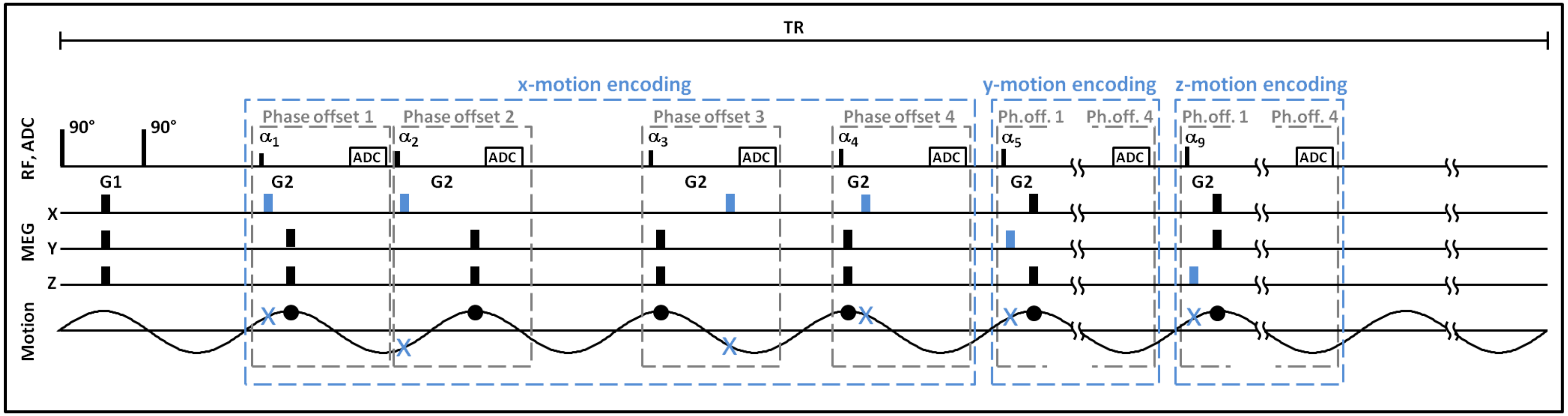

Figure 6.1: Concept of multiaxes multiphase DENSE-MRE. In every subset (x-, y-, z-motion encoding), MEGs G_1 are applied simultaneously on every axis whereas $G_{2,i}$ either capture the wave at the defined sampling points (blue G_2 ($G_{2,m,i}$)) or similar wave points (black G_2 ($G_{2,bg,i}$)). (modified from [110])

6.2 Phantom investigations

The multiaxes multiphase DENSE-MRE acquisition approach was tested using the small agar phantom as described above in Chapter 4.1. With the piezoceramic device and the head rocker (Chapter 2.2.3), a continuous excitation motion with a frequency of 50 Hz was applied. Comparative measurements were performed with the singleaxis multiphase DENSE-MRE scheme.

6.2.1 Acquisition and data processing

In the singleaxis acquisitions, four readout blocks were used to acquire the phase offsets. Three consecutive scans with altered MEG axis gathered all 3D components of the wave motion. In the multiaxes scan, on the other hand, twelf readout blocks were applied. Four blocks for each of the three orthogonal motion enconding axes within one scan. The TM series was adjusted such that the $G_{2,m,i}$ sample the motion and the $G_{2,bg,i}$ encode the background. Due to the additional time t_{add} in each readout block, the readout TE/2 had to be increased. Further sequence parameters were set similar for the multiaxes and the singleaxis acquisitions. Table 6.1 summarizes the applied settings.

For the image processing, the multiaxes dataset was split into three subsets – one for each motion component x, y and z. The constant background phase was eliminated from the image time series. Mean values along the time axis were subtracted in the three consecutive singelaxis acquisition and in each of the three subsets of the multiaxes acquisition individually. To remove drifts of very low spatial frequencies, a spatial Butterworth filter was applied before wave inversion. The filter performed as a band-pass with a lower cut-off at 20 m^{-1} and a higher cut-off at 100 m^{-1}. Hence, also noise was reduced in the wave images. The data was than input to the MDEV inverion [67] (Chapter 2.4.5).

Table 6.1: Multiaxes and singleaxis multiphase DENSE-MRE parameters – small phantom.

Parameter	**Settings**	
FOV	300x300 mm^2	
Matrix	128x128	
Slice thickness	4 mm	
Slices	9	
MEG amplitude	34 mT/m	
MEG duration	1.2 ms	
TR	2520 ms	
readout TE/2	11.8 ms	
Parallel imaging	GRAPPA factor 2	
Partial Fourier	6/8	
	multiaxes	**singleaxis**
Number of TMs	12	4
TMs	[8.00, 23.00, 50.50, 70.50, 88.00, 103.00, 130.50, 150.50, 168.00, 183.00, 210.50, 230.50] ms	[8.00, 23.00, 38.00, 53.00] ms
α-series	[16, 17, 18, 19, 20, 22, 24, 26, 30, 35, 45, 90]°	[30, 35, 45, 90]°
Phase offsets at (sampling axis)	[0, 15, 50, 65, 80, 95, 130, 145, 160, 175, 210, 225] ms	[0, 15, 30, 45] ms
Phase points at (background axes)	[2.5, 22.5, 42.5, 62.5, 82.5, 102.5, 122.5, 142.5, 162.5, 182.5, 202.5, 222.5] ms	–
TA	2 min 31 s	2 min 31 s
Executions	1	3 (x-, y-, z-motion-encoding)
Total TA	2 min 31 s	7 min 33 s

6.2.2 Resulting images and shear modulus assessment

The obtained images show clear wave patterns in all components of the 3D motion acquired with the multiaxes method. The data allowed inversion to shear modulus maps and assessment of the underlying values. A direct comparison with the singleaxis approach showed excellent correspondence in the wave images as well as in the resulting shear modulus maps. Estimation of G^* led to global mean values across all slices which are presented in Table 6.2 for the multiaxes scan and the singleaxis scans and led to almost identical values.

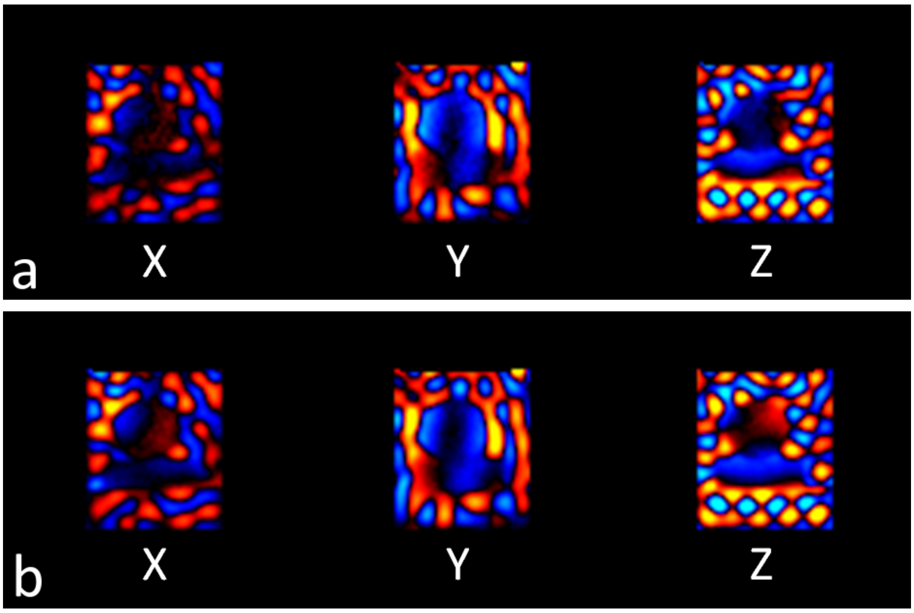

Figure 6.2: Real parts of the first harmonic extracted complex wave images of one slice in the phantom (x-, y- and z-motion components). (a) Wave data acquired with one multiaxes multiphase DENSE-MRE scan. (b) Wave data acquired with three separate singleaxis multiphase scans with altered MEG directions. (modified from [110])

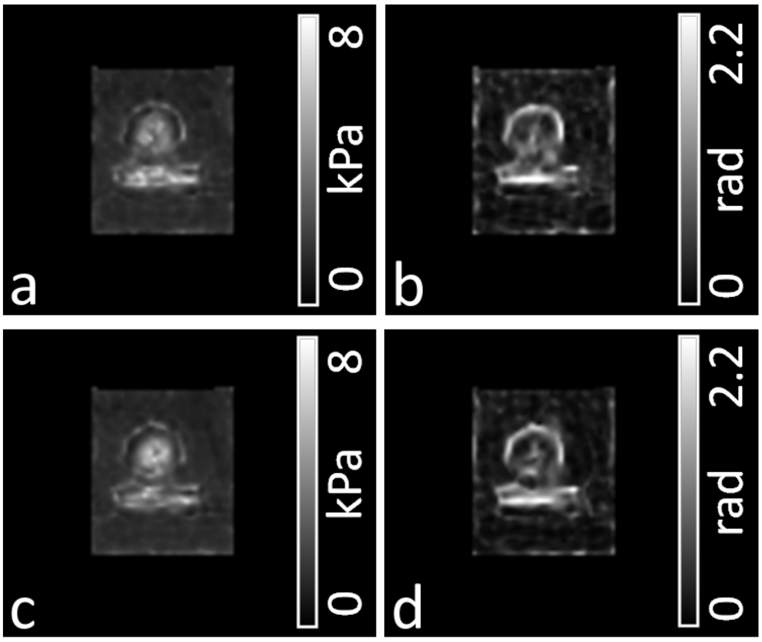

Figure 6.3: Obtained G^* maps in one slice of the of the phantom. The top row shows the results from one multiaxes scan (a,b). In the bottom row the results of a series of three consecutive singleaxis scans with altered MEG axis are depicted (c,d). Shown are maps of $|G^*|$ (a,c) and $\angle(G^*)$ (b,d). (modified from [110])

Table 6.2: Global mean values of $|G^*|$ and $\angle(G^*)$ obtained by the multiaxes and the singleaxis acquisitions in the phantom. (from [110])

	$\boldsymbol{|G^*|}$ **in kPa**	$\boldsymbol{\angle(G^*)}$ **in rad**
Multiaxes	1.66	0.42
Singleaxis	1.64	0.42

6.3 Brain investigations

The multiaxes multiphase DENSE-MRE acquisition scheme was further evaluated for the investigation of the brain. MRE of the brain of a volunteer was examined using multiaxes as well as comparative singleaxis multiphase DENSE-MRE acquisitions with a 20 Hz motion excitation. The imaging parameters were well matched between the scan approaches (Table 6.3).

Table 6.3: Multiaxes and singleaxis multiphase DENSE-MRE parameters – in vivo brain.

Parameter	**Settings**	
FOV	300x300 mm^2	
Matrix	128x128	
Slice thickness	4 mm	
Slices	5	
MEG amplitude	34 mT/m	
MEG duration	0.7 ms	
Parallel imaging	GRAPPA factor 2	
Partial Fourier	6/8	
	multiaxes	**singleaxes**
TR	3250 ms	2500 ms
readout TE/2	23.0 ms	3.8 ms
Number of TMs	12	4
TMs	[8.00, 45.50, 114.25, 164.25, 208.00, 245.50, 314.25, 364.25, 408.00, 445.50, 514.25, 564.25] ms	[8.00, 20.50, 33.00, 45.50] ms
α-series	[16, 17, 18, 19, 20, 22, 24, 26, 30, 35, 45, 90]°	[30, 35, 45, 90]°
Phase offsets at (sampling axis)	[0, 37.5, 125, 162.5, 200, 237.5, 325, 362.5, 400, 437.5, 525, 562.5] ms	[0, 12.5, 25, 37.5] ms
Phase points at (background axes)	[6.25, 56.25, 106.25, 156.25, 206.25, 256.25, 306.25, 356.25, 406.25, 456.25, 506.25, 556.25] ms	–
TA	3 min 15 s	2 min 30 s
Executions	1	3 (x-, y-, z-motion-encoding)
Total TA	3 min 15 s	7 min 30 s

6.3.1 Resulting images and shear modulus assessment

The multiaxes acquisition performed well in the brain. In the multiaxes approach, t_{add} led to a longer TE/2 in the readout parts and the higher number of readout blocks combined with the interleaved multislice imaging led to an increase in TR and TA of one scan. However, the total acquisition time could be reduced to from 7 min 30 s with the three singleaxis scans to 3 min 15 s with the multiaxes approach. The wave images of the multiaxes acquisition were smoothed using a spatial Butterworth low-pass filter with 50 m^{-1} cut-off to minimize noise in the images. The gathered wave patterns matched well between the multiaxes and singleaxis multiphase DENSE-MRE acquisition approaches as can be seen in Figure 6.4. MDEV inversion [67] (Chapter 2.4.5) to shear modulus provided $|G^*|$ and $\angle(G^*)$ maps shown in Figure 6.5. Global mean values were assessed within the brain tissue and resulted in much the same values between both scan approaches (Table 6.4).

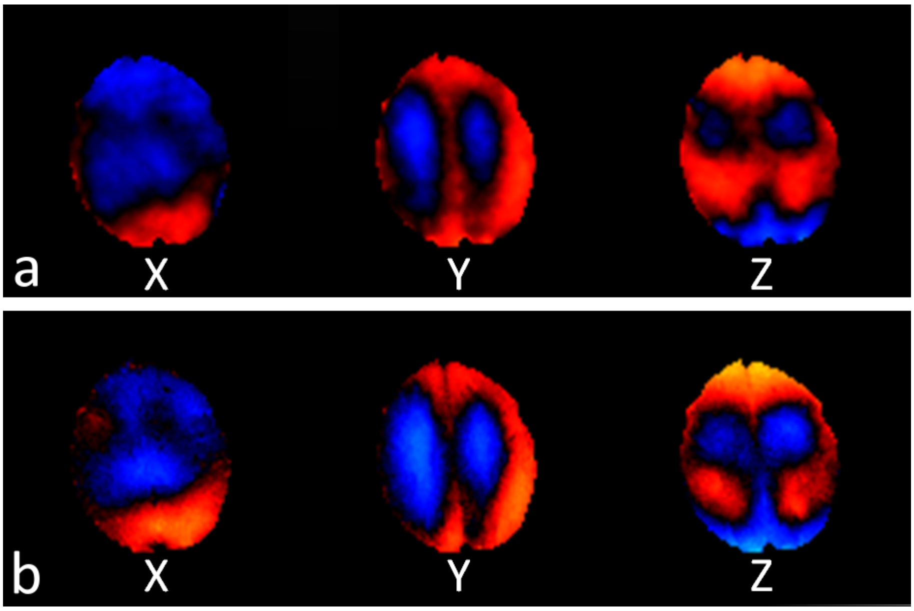

Figure 6.4: Real parts of the first harmonic extracted complex wave images of one slice in the brain of a healthy volunteer (x-, y- and z-motion components). (a) Wave data acquired with one multiaxes multiphase DENSE-MRE scan. (b) Wave data acquired with three separate singleaxis multiphase scans with altered MEG directions. (modified from [110])

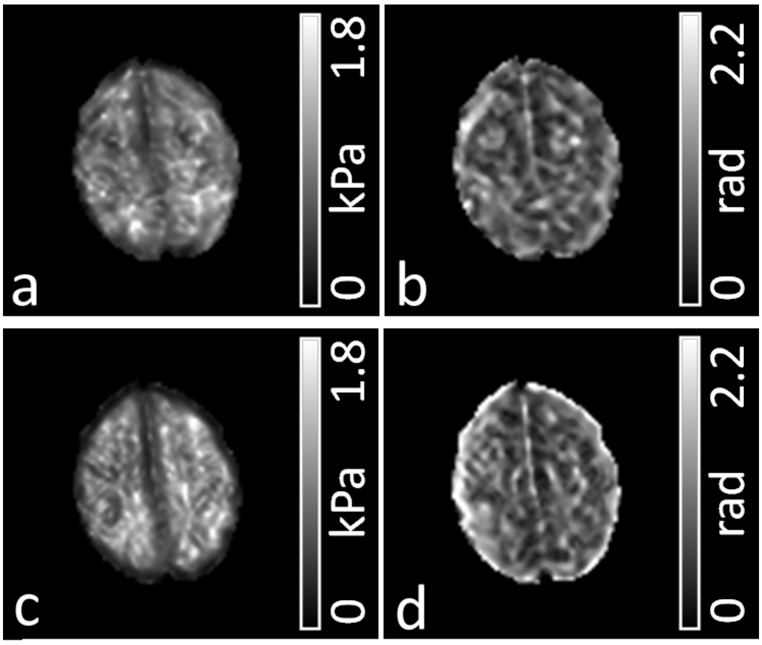

Figure 6.5: Obtained G^* maps in one slice in the brain. The top row shows the results from one multiaxes scan (a,b). In the bottom row, the results of a series of three consecutive singleaxis scans with altered MEG axis are depicted (c,d). Shown are maps of $|G^*|$ (a,c) and $\angle(G^*)$ (b,d). (modified from [110])

Table 6.4: Global mean values of $|G^*|$ and $\angle(G^*)$ obtained by the multiaxes and the singleaxis acquisitions in the brain. (from [110])

	|G*| in kPa	**∠(G*) in rad**
Multiaxes	0.69	0.66
Singleaxes	0.73	0.83

Chapter 7

Discussion

In this thesis, magnetic resonance elastography of the human brain was investigated. A novel acquisition sequence utilizing DENSE-MRE with a multiphase offset readout approach was developed [109]. This approach allows acquiring all dynamic phase offset scans efficiently, which are essential for an MRE examination. Stimulated echoes are used for displacement encoding in DENSE-MRE. Within the multiphase DENSE-MRE scheme, several readouts are performed, which are matched to the excitation frequency in order to fully sample the mechanical waves within one sequence execution [109].

The acquisition of several k-space lines by means of multiple stimulated echo readouts is well-known for accelerating stimulated echo imaging [104]. The innovation in the presented concept is that the acquisition time is reduced by gathering all time-resolved phase offsets within each TR during a single sequence run. Hence, a significant benefit is, that encoding the displacements of all dynamic phase offsets is realized as short as possible in time. Thus, it helps to keep influences such as misalignments of k-space lines because of patient movement and magnetic field fluctuations to a minimum when phase contrast images are generated. Known from phase contrast imaging in flow-encoded MRI [96], this concept is also advantageous in MRE, where the phase offset image series is processed to a first harmonic wave image. Additionally to acquiring all phase offsets in a compact way, there are several benefits in applying DENSE in MRE. The DENSE-MRE technique allows utilizing short echo times, which is superior in tissues with short T2 and T2* values [31]. It also helps preventing susceptibility related artifacts. Especially conventional GRE-MRE sequences might reach their limit in tissues with short T2* relaxation rates due to degraded signal intensity [132]. Spin echo MRE sequences, where, in contrast to GRE sequences, TE can be longer due to the T2 dependency and susceptibility artifacts are not an issue, are a possible choice to perform difficult MRE acquisitions. Spin echo MRE sequences have been proposed to perform MRE exams in livers of patients with iron overload when the tissue shows up very short T2* values [133]. DENSE-MRE could be an alternative to spin echo sequences, especially with the acceleration by the multiphase expansion. Furthermore, in DENSE-MRE, the excitation frequency and the motion encoding gradient durations are not coupled [31]. This easily allows using low excitation frequencies in MRE experiments. In conventional MRE sequences, a low excitation frequency means a long MEG duration and hence, a long echo time is required which results in an advanced MR signal decay when the echo is recorded. In multiphase DENSE-MRE, the short echo times can be used independent of the excitation frequency. To further reduce the scan time, the proposed sequence allows interleaved multislice imaging. In the presented experiments, up to 15 transversal slices have been acquired to demonstrate the interleaved multislice acquisition capability. Increasing the number of interleaved slices is possible and allows whole brain investigations. The number of slices can be chosen in a way, that multiplied by the excitation wave period a matching with TR results. This has an effect on the continuity of the excitation motion and the sampling-point matching between the slices. The continuous harmonic excitation ensures a steady-state condition of the wave field in the tissue while the image acquisition which is advantageous in MRE [89]. Realized is this by repeated trigger pulses in the MRE sequence, which synchronize the excitation device to the MRI scanner. Proper slice number and associated mutlislice timings ensure acquiring the same sampling points in all slices. This, however, restricts the maximum interleaved slice number. Imaging more slices will be possible, if the sampling point matching across the slices is neglected during the acquisition. In this cause, the motion information across all slices can be matched afterwards during postprocessing by slice-wise shifting the phase of each complex wave image appropriately [89].

In the phantom experiments, the feasibility of the multiphase DENSE-MRE for fully sampling the wave motion could be demonstrated. Comparison with singlephase DENSE-MRE resulted in excellent correlation of the gathered wave images. As four phase offsets were acquired in the experiments, an acceleration of the scan time by factor of four was achieved. In contrast, since in the multiphase scheme only one of the MEGs samples the wave, the motion encoding efficiency is lower than in the singlephase scheme. Further validation of the multiphase acquisition approach was done with respect to the obtained shear modulus maps. Phantoms made of agar are stiffer in parts with higher agar concentration and softer in lower agar concentrated regions [10]. In the obtained shear modulus maps, the higher agar concentrated inclusions are clearly distinguishable from the lower agar concentrated bulk material. Regional evaluation of the mean values of $|G^*|$ also confirmed the higher stiffness within the inclusions in contrast to the softer surrounding. Furthermore, the phantom was also imaged using a conventional GRE-MRE sequence. A comparison of the obtained shear modulus maps from both acquisitions confirmed the results of the multiphase DENSE-MRE approach. In the $|G^*|$ as well as in the $\angle(G^*)$ maps, all five slices showed visual similarity between the two acquisitions. Also the evaluated mean values corresponded well in $|G^*|$ and also in $\angle(G^*)$. The applicability of the multiphase DENSE-MRE sequence to acquire wave images at different excitation frequencies for consecutive multifrequency MRE experiments was demonstrated using a larger phantom. Even though the excitation frequency was changed between the measurements from 20 Hz over 60 Hz to 100 Hz, the sequence parameters could be kept unchanged as the sampling points could be reached with the same TM series for this set of excitation frequencies. On the other hand, by adapting the TM series, any excitation frequency or other suitable combinations of different frequencies can be used together with the multiphase DENSE-MRE scheme.

The efforts which were made in the phantom research led to the MRE investigation of the brain with the developed multiphase DENSE-MRE acquisition approach. In healthy volunteers, the feasibility of this multiphase scheme was demonstrated. In the brain investigations, a 20 Hz excitation frequency was applied to especially obtain low frequency MRE images. Motion encoded images could be acquired which showed the wave patterns within the brain. The shear modulus assessment of the brain tissue showed a median global $|G^*|$ of 0.72 kPa across all subjects. This is very similar to the results of brain MRE experiments using low excitation frequencies with 10 Hz to 20 Hz presented by Dittmann et al. [89]. They found a mean $|G^*|$ of 0.62 ± 0.08 kPa (mean ± SD) in the investigated group of eight healthy volunteers [89]. In contrast to the global value, the values of the different regions of white matter and gray matter show higher median $|G^*|$. This suggests that the global $|G^*|$ assessment might be influenced by partial-volume effects with cerebrospinal fluid.

The MDEV inversion algorithm [67] applied in this thesis uses finite difference operators which can retrieve the spatial derivatives for the shear modulus estimation in pixel-wise resolution [134]. Limitations in discretization of the waves at short spatial wavelengths can lead to overestimated stiffness values, whereas at low excitation frequencies and accompanied long spatial wavelengths, noise in the wave images can lead to underestimated stiffness values [134]. For the angle of the complex shear modulus, noise in the wave images can lead to overestimated values of $\angle(G^*)$ [89]. Thus, to reduce noise, the wave images were smoothed during inversion [67, 89].

Another point concerning the sampling of the wave motion is the order of the sampling points during the acquisition. A strict forward way would be to acquire the sampling points subsequently in the chronological ascending order as they appear on the harmonic wave motion. The timeline of the dataset would then directly describe the harmonic motion. However, the acquisition order of the sampling points can also be permuted in multiphase DENSE-MRE. This brings the benefit of minimizing the time slots between each readout block and thereby enables a higher number of interleaved slices within one TR. The images can be rearranged afterwards to obtain the correct order. The effectiveness of the rearrangement concept is coupled to the excitation frequency with its sampling point intervals (ΔT_u) and the time one readout block lasts. In the phantom experiments, the rearrangement concept was thus utilized, whereas the in vivo scans were performed directly in chronologically ascending sampling point order. The MRE acquisitions were performed with four phase offsets. However, also an increased number of phase offsets can be imaged with the multiphase DENSE-MRE method. In this case the rearrangement approach might be used to increase overall efficiency even at low excitation frequencies.

The concept of multiphase DENSE-MRE also brings along some limitations. The acquisition generates, besides the phase according to the motion, also an additional constant phase value along the phase offset time series. This background phase was eliminated by mean value subtraction to reveal the clear waves within the images. The background phase elimination thereby reduced the few spatial phase wraps within the images. However, if there were phase wraps over the time dimension, this could lead to an incorrect elimination. Background phase elimination was therefore performed in the exponential domain and motion excitation together with encoding strength was adjusted to keep this influence minimal. The usage of stimulated echoes also bring along a general limitation. In general, stimulated echo sequences offer just one half of the maximum signal intensity that spin-echo sequences can provide [104]. However, in DENSE-MRE, the signal loss from ongoing transversal relaxation is less since shorter echo times can be applied. As the minimum TE depends on the MEG duration, the MEG parameters have to be balanced between the aspects of short echo times and high motion encoding efficiencies. A benefit of the developed multiphase DENSE-MRE scheme is the reduction in scan time as all wave sampling points are imaged at once. Hence, compared with singlephase DENSE-MRE, the acceleration factor in multiphase-DENSE-MRE is given by the number of simultaneously acquired phase offsets. In the presented investigations, the achieved acceleration was a factor of four. Increasing the number of phase offsets results in higher acceleration but, in contrast, also less available signal in each readout. In contrast to conventional GRE-MRE, TR has to be longer in DENSE-MRE due to the T1 signal relaxation. The multiphase DENSE-MRE approach is thus more efficient when higher numbers of sampling points and interleaved slices are acquired. Nevertheless, other MRE sequence approaches with EPI readouts and fractional motion encoding [89] can acquire the wave data even faster than the multiphase DENSE-MRE approach. The use of EPI trajectories, however, brings along EPI distortions in the acquisitions. In DENSE-MRE with conventional readout trajectories, EPI distortions and susceptibility artifacts are normally not an issue, as the stimulated echo is fully refocused.

Further technical development of the multiphase DENSE-MRE sequence led to an enhancement by including the multiaxes acquisition approach into the multiphase scheme. The MR phase signal is therefor modified by MEGs on all three gradient axes. Due to the simultaneous motion encoding preparation on all axes by the G_1, the phase also has to be modified with G_2 on all three axes to not only finalize the motion encoding but also to produce a stimulated echo in each readout block. In general, the generated MR phase signal is a scalar and represents the sum of all encoded motion directions in the first place. However, different G_2 shifts within each readout block together with the wave sampling and first harmonic extraction techniques used in MRE allow separating the motion components afterwards.

The developed multiaxes adaption of the multiphase DENSE-MRE, enabled acquiring the complete three-dimensional wave image dataset within one scan. In the phantom experiments, the multiaxes sequence allowed utilizing the same acquisition time as for one of the singleaxis scans. Hence, as the singleaxis scans were performed three times with altered MEG axis, an acceleration by factor three was achieved with the multiaxes scheme. After decomposition of the motion components, the wave images showed excellent matching between the two acquisition approaches. The resulting shear modulus maps and evaluated global values ($|G^*| = 1.66$ kPa (1.64 kPa), $\angle(G^*) = 0.42$ rad (0.42 rad) in the multiaxes (singleaxis) investigation) further confirmed this excellent matching.

In the brain investigations, the low excitation frequency prolonged the applicable readout-TE and TM series. TR was thus increased in contrast to the singleaxis scans, resulting in an acceleration of roughly 2.3-fold by the multiaxes version. The obtained images match well between the two acquisition approaches. The global shear modulus assessment in the brain tissue yielded comparable values between the two approaches ($|G^*| = 0.69$ kPa (0.73 kPa), $\angle(G^*) = 0.66$ rad (0.83 rad) in the multiaxes (singleaxis) investigation) and also fit to the data presented in the multiphase DENSE-MRE chapter of the invivo brain investigations ($|G^*| = 0.72$ kPa, $\angle(G^*) = 1.03$ rad in the global assessment). In the multiaxes multiphase DENSE-MRE approach, a benefit arises with respect to image registration of the wave image dataset. In the singleaxis multiphase DENSE-MRE scheme, misalignments of k-space lines due to unwanted patient movements are reduced as all sampling points are acquired during each TR. Hence, the phase offset images are inherently registered to each other. Such an inherent image registration also provide modified conventional MRE sequences that incorporate SLIM to acquire all three-dimensional motion components simultaneously, where misregistration artifacts caused by biological motions or varying physiological states are reduced [103]. As the multiaxes multiphase DENSE-MRE sequence acquires all sampling points as well as all motion components during each TR, k-space misalignments are further kept to a minimum for the full four-dimensional phase offset image stack, resulting in an inherent image registration and a potentially more accurate full wave image dataset.

A part of the temporal shift to reach the desired sampling points has to be performed inside each readout block. Timing optimized appearance of the G_2 needs a slot of 3/8 times the excitation wave period time. As a consequence, TE approximately prolongs by this time and the minimum TE depends on the used excitation frequency. Hence, in the point of very short-TE MRE imaging, the multiaxes scheme is less effective than the singleaxis multiphase DENSE-MRE approach. A second limitation arises from the higher number of readout blocks as the TM-series elongates to gather all sampling points and motion components. Thus, more pronounced T1 relaxation of the available prepared longitudinal magnetization is present. Hence, the SNR of the images is lower than in the singleaxis scans. In the phantom scans with the higher excitation frequency of 60 Hz, the impact of the prolonged readout-TE was minor compared with the in vivo brain acquisitions where a 20 Hz excitation was applied. The increase in noise in the in vivo images, however, could be tackled by the application of an additional spatial low-pass filter. In return, by imaging all motion components at the same time, the loss in SNR can potentially be accepted as therefor a further reduction in the total scan time by up to a factor of three can be achieved.

Chapter 8

Conclusion and outlook

In this thesis, magnetic resonance elastography was utilized to assess the mechanical properties of human brain tissue in vivo. For this purpose, a novel efficient image acquisition approach was developed to especially allow MRE of the brain at a low excitation frequency of 20 Hz while keeping the echo time short. The feasibility of the developed acquisition approach to acquire all MRE relevant phase-offset scans is shown. The results from comparative phantom experiments demonstrate that the developed multiphase DENSE-MRE concept performs well in comparison with conventional acquisition approaches in terms of wave image quality and obtained shear modulus maps. In the brain investigations, the results demonstrate that the acquisition scheme is well-suited for low excitation frequencies. The results also demonstrate that the images do not suffer from susceptibility artifacts. The acquisition time can be significantly reduced with the multiphase expansion. Efficient multislice MRE of the brain is thus possible in clinical practice. Further modification of the multiphase DENSE-MRE sequence with the multiaxes scheme, allows additional efficiency enhancement.

The presented work builds the basis for a currently ongoing brain MRE study in a large cohort of patients with neurological diseases and healthy controls, seeking for differences in the shear modulus maps due to variances in the brains biomechanical conditions. The scans are therefor performed not only in five slices, but the interleaved slice acquisition was increased to cover the whole brain within the same acquisition time. Over 100 study participants have already been investigated and high quality images could be obtained. As for now, the participant recruiting and data acquisition is in progress. The gathered MRE data hopefully allows the identification of newly discovered insights into the brain biomechanical structures at low excitation frequency of 20 Hz and neurological disease related alterations within it.

The presented acquisition sequences are not limited to MRE investigations of the human brain, but can easily be used to investigate different tissue types. Especially in tissues with short T2 and T2* times, the presented multiphase DENSE-MRE technique could be powerful. The technique could be extremely beneficial for example in MRE investigations of the liver, when the livers had iron overload. In such livers, the multiphase DENSE-MRE sequence with its advantage of allowing short echo times could increase the feasibility of performing MRE acquisitions.

Besides clinical applications, the presented methods could be enhanced by further technical developments, aiming for higher acceleration of the acquisition with focus on the multiaxes multiphase DENSE-MRE concept. As in this approach the full motion information is imaged at once, it offers more robustness against non-excitation related subject movements on the one hand but there is still space for improvements like allowing shorter echo times, shorter mixing times and higher slice numbers. Also, adding more advanced readout trajectories like EPI to the sequence could potentially further improve the MRE acquisitions. All in all, this could further lead to potential undiscovered applications fields of MRE and provide MRE feasibility even in currently challenging areas.

Bibliography

[1] Venkatesh SK Ehman RL, editors. *Magnetic Resonance Elastography.* Springer New York Heidelberg Dordrecht London, 2014.

[2] Hirsch S, Braun J, Sack I. *Magnetic Resonance Elastography: Physical Background And Medical Applications.* Wiley-VCH, 2017.

[3] Streitberger KJ, Sack I, Krefting D, Pfüller C, Braun J, Paul F, Würfel J. Brain Viscoelasticity Alteration in Chronic-Progressive Multiple Sclerosis. *PLoS ONE*, 7(1):e29888, 2012.

[4] Sack I. Magnetresonanz-Elastographie Magnetic resonance elastography. *Dtsch Med Wochenschr*, 133:247–251, 2008.

[5] Muthupillai R Ehman RL. Magnetic resonance elastography. *Nature Medicine*, 2(5):601–603, 1996.

[6] Pepin K, Ehman R, McGeeb K. Magnetic resonance elastography (MRE) in cancer: Technique, analysis, and applications. *Progress in Nuclear Magnetic Resonance Spectroscopy*, 90-91(November):32–48, 2015.

[7] Uffmann K Ladd ME. Actuation systems for MR elastography. *IEEE Engineering in Medicine and Biology Magazine*, 27(3):28–34, 2008.

[8] Ophir J, Céspedes I, Ponnekanti H, Yazdi Y, Li X. ELASTOGRAPHY: A QUANTITATIVE METHOD FOR IMAGING THE ELASTICITY OF BIOLOGICAL TISSUES. *ULTRASONIC IMAGING*, 13(1991):111–134, 1991.

[9] Chenevert TL, Skovoroda AR, O'Donnell M, Emelianov SY. Elasticity reconstructive imaging by means of stimulated echo MRI. *Magnetic Resonance in Medicine*, 39(3):482–490, 1998.

[10] Mariappan YK, Glaser KJ, Ehman RL. Magnetic resonance elastography: A review. *Clinical Anatomy*, 23(5):497–511, 2010.

[11] Glaser KJ, Manduca A, Ehman RL. Review of MR elastography applications and recent developments. *Journal of Magnetic Resonance Imaging*, 36(4):757–774, oct 2012.

[12] Bohte A, Nelissen J, Runge J, Holub O, Lambert S, Graaf Ld, Kolkman S, Meij Sv. d, Stoker J, Strijkers G, Nederveen A, Sinkus R. Breast magnetic resonance elastography : a review of clinical work and future perspectives. *NMR in Biomedicine*, 31(March):1–14, 2018.

[13] Muthupillai R, Lomas DJ, Rossman PJ, Greenleaf JF, Manduca A, Ehman RL. Magnetic Resonance Elastography by Direct Visualization of Propagating Acoustic Strain Waves. *Science*, 269(5232):1854–1857, 1995.

[14] Parker KJ, Huang SR, Musulin RA, Lerner RM. Tissue response to mechanical vibrations for "sonoelasticity imaging". *Ultrasound in Medicine and Biology*, 16(3):241–246, 1990.

[15] Muthupillai R, Rossman PJ, Lomas DJ, Greenleaf JF, Riederer SJ, Ehman RL. Magnetic Resonance Imaging of Transverse Acoustic Strain Waves. *Magnetic Resonance in Medicine*, 36(2):266–274, 1996.

[16] Lieber RL, Steinman S, Barash IA, Chambers H. Structural and functional changes in spastic skeletal muscle, may 2004.

[17] Dresner AM, Rose GH, Rossman PJ, Muthupillai R, Manduca A, Ehman RL. Magnetic resonance elastography of skeletal muscle. *Journal of Magnetic Resonance Imaging*, 13(2):269–276, 2001.

[18] Uffmann K, Maderwald S, Ajaj W, Galban CG, Mateiescu S, Quick HH, Ladd ME. In vivo elasticity measurements of extremity skeletal muscle with MR elastography. *NMR in Biomedicine*, 17(4):181–190, jun 2004.

[19] Chakouch MK, Charleux F, Bensamoun SF. Quantifying the elastic property of nine thigh muscles using magnetic resonance elastography. *PLoS ONE*, 10(9):e0138873, sep 2015.

[20] Basford JR, Jenkyn TR, An KN, Ehman RL, Heers G, Kaufman KR. Evaluation of healthy and diseased muscle with magnetic resonance elastography. *Archives of Physical Medicine and Rehabilitation*, 83(11):1530–1536, nov 2002.

[21] McCullough MB, Domire ZJ, Reed AM, Amin S, Ytterberg SR, Chen Q, An KN. Evaluation of muscles affected by myositis using magnetic resonance elastography. *Muscle and Nerve*, 43(4):585–590, apr 2011.

[22] Bensamoun SF, Ringleb SI, Chen Q, Ehman RL, An KN, Brennan MD. Thigh muscle stiffness assessed with magnetic resonance elastography in hyperthyroid patients before and after medical treatment. *Journal of Magnetic Resonance Imaging*, 26(3):708–713, sep 2007.

[23] Strijkers GJ, Araujo EC, Azzabou N, Bendahan D, Blamire A, Burakiewicz J, Carlier PG, Damon B, Deligianni X, Froeling M, Heerschap A, Hollingsworth KG, Hooijmans MT, Karampinos DC, Loudos G, Madelin G, Marty B, Nagel AM, Nederveen AJ, Nelissen JL, Santini F, Scheidegger O, Schick F, Sinclair C, Sinkus R, De Sousa PL, Straub V, Walter G, Kan HE. Exploration of new contrasts, targets, and MR imaging and spectroscopy techniques for neuromuscular disease-A workshop report of working group 3 of the biomedicine and molecular biosciences COST action BM1304 MYO-MRI, 2019.

[24] Plewes DB, Bishop J, Samani A, Sciarretta J. Visualization and quantification of breast cancer biomechanical properties with magnetic resonance elastography. *Physics in Medicine and Biology*, pages 1591–1610, 2000.

[25] Sinkus R, Lorenzen J, Schrader D, Lorenzen M, Dargatz M, Holz D. High-resolution tensor MR elastography for breast tumour detection. *Physics in Medicine and Biology*, 45(6):1649–1664, 2000.

[26] Lorenzen J, Sinkus R, Lorenzen M, Dargatz M, Leussler C, Röschmann P, Adam G. MR elastography of the breast: Preliminary clinical results. *RoFo Fortschritte auf dem Gebiet der Rontgenstrahlen und der Bildgebenden Verfahren*, 174(7):830–834, jul 2002.

[27] Hoelzl SH, Sethi S, Sudakova J, Dokumaci AS, Runge JH, Ng T, Purushotham A, Sinkus R. Enabling high resolution MRE images of the breast. In *Proc. Intl. Soc. Mag. Reson. Med. 25 (2017)*, page 4938, 2017.

[28] Balleyguier C, Lakhdar AB, Dunant A, Mathieu MC, Delaloge S, Sinkus R. Value of whole breast magnetic resonance elastography added to MRI for lesion characterization. *NMR in Biomedicine*, 31(1):e3795, jan 2018.

[29] Patel BK, Samreen N, Zhou Y, Chen J, Brandt K, Ehman R, Pepin K. MR Elastography of the Breast: Evolution of Technique, Case Examples, and Future Directions, 2020.

[30] Elgeti T, Rump J, Hamhaber U, Papazoglou S, Hamm B, Braun J, Sack I. Cardiac magnetic resonance elastography: Initial results. *Investigative Radiology*, 43(11):762–772, nov 2008.

[31] Robert B, Sinkus R, Gennisson JL, Fink M. Application of DENSE-MR-Elastography to the Human Heart. *Magnetic Resonance in Medicine*, 62(5):1155–1163, 2009.

[32] Khan S, Fakhouri F, Majeed W, Kolipaka A. Cardiovascular Magnetic Resonance Elastography: A Review HHS Public Access. *NMR Biomed*, 31(10):3853, 2018.

[33] Rump J, Klatt D, Braun J, Warmuth C, Sack I. Fractional Encoding of Harmonic Motions in MR Elastography. *Magnetic Resonance in Medicine*, 57(2):388–395, 2007.

[34] Venkatesh S, Kundapur , Ehman RL. Magnetic resonance elastography of abdomen. *Abdominal Imaging*, 40(4):745–759, 2015.

[35] Low G, Kruse SA, Lomas DJ. General review of magnetic resonance elastography. *World Journal of Radiology*, 8(1):59, 2016.

[36] Dittmann F, Tzschätzsch H, Hirsch S, Barnhill E, Braun J, Sack I, Guo J. Tomoelastography of the abdomen: Tissue mechanical properties of the liver, spleen, kidney, and pancreas from single MR elastography scans at different hydration states. *Magnetic Resonance in Medicine*, 78(3):976–983, 2017.

[37] Akkaya HE, Erden A, Öz DK, Ünal S, Erden l. Magnetic resonance elastography: Basic principles, technique, and clinical applications in the liver. *Diagnostic and Interventional Radiology*, 24(6):328–335, 2018.

[38] Yin M, Talwalkar JA, Glaser KJ, Manduca A, Grimm RC, Rossman PJ, Fidler JL, Ehman RL. Assessment of Hepatic Fibrosis With Magnetic Resonance Elastography. *Clinical Gastroenterology and Hepatology*, 5(10):1207–1213.e2, oct 2007.

[39] Huwart L, Sempoux C, Vicaut E, Salameh N, Annet L, Danse E, Peeters F, Beek LCt, Rahier J, Sinkus R, Horsmans Y, Van Beers BE. Magnetic Resonance Elastography for the Noninvasive Staging of Liver Fibrosis. *Gastroenterology*, 135(1):32–40, 2008.

[40] Asbach P, Klatt D, Schlosser B, Biermer M, Muche M, Rieger A, Loddenkemper C, Somasundaram R, Berg T, Hamm B, Braun J, Sack I. Viscoelasticity-based staging of hepatic fibrosis with multifrequency MR elastography. *Radiology*, 257(1):80–86, 2010.

[41] Wang QB, Zhu H, Liu HL, Zhang B. Performance of magnetic resonance elastography and diffusion-weighted imaging for the staging of hepatic fibrosis: A meta-analysis. *Hepatology*, 56(1):239–247, 2012.

[42] Su LN, Guo SL, Li BX, Yang P. Diagnostic value of magnetic resonance elastography for detecting and staging of hepatic fibrosis: A meta-analysis. *Clinical Radiology*, 69(12):e545–e552, 2014.

[43] Singh S, Venkatesh SK, Wang Z, Miller FH, Motosugi U, Low RN, Hassanein T, Asbach P, Godfrey EM, Yin M, Chen J, Keaveny AP, Bridges M, Bohte A, Murad MH, Lomas DJ, Talwalkar JA, Ehman RL. Diagnostic performance of magnetic resonance elastography in staging liver fibrosis: A systematic review and meta-analysis of individual participant data. *Clinical Gastroenterology and Hepatology*, 13(3):440–451.e6, 2015.

[44] Loomba R, Cui J, Wolfson T, Haufe W, Hooker J, Szeverenyi N, Ang B, Bhatt A, Wang K, Aryafar H, Behling C, Valasek MA, Lin GY, Gamst A, Brenner DA, Yin M, Glaser KJ, Ehman RL, Sirlin CB. Novel 3D Magnetic Resonance Elastography for the Noninvasive Diagnosis of Advanced Fibrosis in NAFLD: A Prospective Study. *American Journal of Gastroenterology*, 111(7):986–994, 2016.

[45] Plaikner M, Kremser C, Viveiros A, Zoller H, Henninger B. Magnetic resonance elastography of the liver: Worth knowing for clinical routine. *Radiologe*, pages 966–978, 2020.

[46] Tang A, Cloutier G, Szeverenyi NM, Sirlin CB. Ultrasound elastography and MR elastography for assessing liver fibrosis: Part 2, diagnostic performance, confounders, and future directions. *American Journal of Roentgenology*, 205(1):33–40, 2015.

[47] Kim YS, Song JS, Kannengiesser S, Seo SY. Comparison of spin-echo echoplanar imaging and gradient recalled echo-based MR elastography at 3 Tesla with and without gadoxetic acid administration. *European Radiology*, 27(10):4120–4128, 2017.

[48] Venkatesh SK, Yin M, Glockner JF, Takahashi N, Araoz PA, Talwalkar JA, Ehman RL. MR elastography of liver tumors: Preliminary results. *American Journal of Roentgenology*, 190(6):1534–1540, 2008.

[49] Thompson SM, Wang J, Chandan VS, Glaser KJ, Roberts LR, Ehman RL, Venkatesh SK. MR elastography of hepatocellular carcinoma Correlation of tumor stiffness with histopathology features Preliminary findings. *Magnetic Resonance Imaging*, 37:41–45, 2017.

[50] Qayyum A, Hwang KP, Stafford J, Verma A, Maru DM, Sandesh S, Sun J, Pestana RC, Avritscher R, Hassan MM, Amin H, Rashid A, Wistuba II, Ehman RL, Ma J,

Kaseb AO. Immunotherapy response evaluation with magnetic resonance elastography (MRE) in advanced HCC. *Journal for ImmunoTherapy of Cancer*, 7(1):1–6, 2019.

[51] Ichikawa S, Motosugi U, Enomoto N, Onishi H. Magnetic resonance elastography can predict development of hepatocellular carcinoma with longitudinally acquired two-point data. *European Radiology*, 29(2):1013–1021, 2019.

[52] Hiscox LV, Johnson CL, Barnhill E, McGarry MDJ, Huston J, Beek EJRv, Starr JM, Roberts N. Magnetic resonance elastography (MRE) of the human brain: technique, findings and clinical applications. *Physics in Medicine and Biology*, 61(24):R401–R437, 2016.

[53] Manduca A, Oliphant T, Dresner M, Mahowald J, Kruse S, Amromin E, Felmlee J, Greenleaf J, Ehman R. Magnetic resonance elastography: Non-invasive mapping of tissue elasticity. *Medical Image Analysis*, 5(4):237–254, dec 2001.

[54] Hiscox LV, McGarry MD, Schwarb H, Van Houten EE, Pohlig RT, Roberts N, Huesmann GR, Burzynska AZ, Sutton BP, Hillman CH, Kramer AF, Cohen NJ, Barbey AK, Paulsen KD, Johnson CL. Standard-space atlas of the viscoelastic properties of the human brain. *Human Brain Mapping*, (May):1–19, 2020.

[55] Sack I, Beierbach B, Wuerfel J, Klatt D, Hamhaber U, Papazoglou S, Martus P, Braun J. The impact of aging and gender on brain viscoelasticity. *NeuroImage*, 46(3):652–657, 2009.

[56] Arani A, Murphy MC, Glaser KJ, Manduca A, Lake DS, Kruse SA, Jack CR, Ehman RL, Huston J. Measuring the effects of aging and sex on regional brain stiffness with MR elastography in healthy older adults. *NeuroImage*, 111:59–64, 2015.

[57] Sack I, Streitberger KJ, Krefting D, Paul F, Braun J. The influence of physiological aging and atrophy on brain viscoelastic properties in humans. *PLoS ONE*, 6(9), 2011.

[58] Kruse SA, Rose GH, Glaser KJ, Manduca A, Felmlee JP, Jack CR, Ehman RL. Magnetic resonance elastography of the brain. *NeuroImage*, 39(1):231–237, jan 2008.

[59] Braun J, Guo J, Lützkendorf R, Stadler J, Papazoglou S, Hirsch S, Sack I, Bernarding J. High-resolution mechanical imaging of the human brain by three-dimensional multifrequency magnetic resonance elastography at 7T. *NeuroImage*, 90:308–314, apr 2014.

[60] Johnson CL, McGarry MD, Van Houten EE, Weaver JB, Paulsen KD, Sutton BP, Georgiadis JG. Magnetic resonance elastography of the brain using multishot spiral readouts with self-navigated motion correction. *Magnetic Resonance in Medicine*, 70(2):404–412, 2013.

[61] Johnson CL, McGarry MD, Gharibans AA, Weaver JB, Paulsen KD, Wang H, Olivero WC, Sutton BP, Georgiadis JG. Local mechanical properties of white matter structures in the human brain. *NeuroImage*, 79:145–152, 2013.

[62] Johnson CL, Schwarb H, McGarry MD, Anderson AT, Huesmann GR, Sutton BP, Cohen NJ. Viscoelasticity of subcortical gray matter structures. *Human Brain Mapping*, 37(12):4221–4233, 2016.

[63] Guo J, Hirsch S, Fehlner A, Papazoglou S, Scheel M, Braun J, Sack I. Towards an Elastographic Atlas of Brain Anatomy. *PLoS ONE*, 8(8):e71807, 2013.

[64] Murphy MC, Huston III J, Jack CR, Glaser KJ, Manduca A, Felmlee JP, Ehman RL. Decreased brain stiffness in Alzheimer's disease determined by magnetic resonance elastography. *Journal of Magnetic Resonance Imaging*, 34(3):494–498, 2011.

[65] Huston J, Murphy MC, Boeve BF, Fattahi N, Arani A, Glaser KJ, Manduca A, Jones DT, Ehman RL. Magnetic resonance elastography of frontotemporal dementia. *Journal of Magnetic Resonance Imaging*, 43(2):474–478, feb 2016.

[66] ElSheikh M, Arani A, Perry A, Boeve BF, Meyer FB, Savica R, Ehman RL, Huston J. MR elastography demonstrates unique regional brain stiffness patterns in dementias. *American Journal of Roentgenology*, 209(2):403–408, 2017.

[67] Streitberger KJ, Reiss-Zimmermann M, Freimann FB, Bayerl S, Guo J, Arlt F, Wuerfel J, Braun J, Hoffmann KT, Sack I. High-resolution mechanical imaging of glioblastoma by multifrequency magnetic resonance elastography. *PLoS ONE*, 9(10), 2014.

[68] Lipp A, Skowronek C, Fehlner A, Streitberger KJ, Braun J, Sack I. Progressive supranuclear palsy and idiopathic Parkinson's disease are associated with local reduction of in vivo brain viscoelasticity. *European Radiology*, 28(8):3347–3354, aug 2018.

[69] Wuerfel J, Paul F, Beierbach B, Hamhaber U, Klatt D, Papazoglou S, Zipp F, Martus P, Braun J, Sack I. MR-elastography reveals degradation of tissue integrity in multiple sclerosis. *NeuroImage*, 49(3):2520–2525, 2010.

[70] Fehlner A, Behrens JR, Streitberger KJ, Papazoglou S, Braun J, Bellmann-Strobl J, Ruprecht K, Paul F, Würfel J, Sack I. Higher-resolution MR elastography reveals

early mechanical signatures of neuroinflammation in patients with clinically isolated syndrome. *Journal of Magnetic Resonance Imaging*, 44(1):51–58, 2016.

[71] Murphy MC, Huston JI, Ehman RL. MR elastography of the brain and its application in neurological diseases. *NeuroImage*, 187:176–183, 2019.

[72] Steger HG, Sieghart J, Glauninger E. *Technische Mechanik 2 - Festigkeitslehre, Kinematik, Kinetik, Hydromechanik (4. Auflage)*. Wien, öbv&hpt, 2000.

[73] Van Houten EEW, Paulsen KD, Miga MI, Kennedy FE, Weaver JB. An Overlapping Subzone Technique for MR-Based Elastic Property Reconstruction. *Magnetic Resonance in Medicine*, 42:779–786, 1999.

[74] Hamhaber U, Grieshaber FA, Nagel JH, Klose U. Comparison of quantitative shear wave MR-elastography with mechanical compression tests. *Magnetic Resonance in Medicine*, 49(1):71–77, 2003.

[75] Klatt D, Hamhaber U, Asbach P, Braun J, Sack I. Noninvasive assessment of the rheological behavior of human organs using multifrequency MR elastography: A study of brain and liver viscoelasticity. *Physics in Medicine and Biology*, 52(24):7281–7294, 2007.

[76] Tse ZT, Janssen H, Hamed A, Ristic M, Young I, Lamperth M. Magnetic resonance elastography hardware design: A survey. *Proceedings of the Institution of Mechanical Engineers, Part H: Journal of Engineering in Medicine*, 223(4):497–514, 2009.

[77] Yin M, Talwalkar JA, Glaser KJ, Venkatesh SK, Chen J, Manduca A, Ehman RL. Dynamic postprandial hepatic stiffness augmentation assessed with MR elastography in patients with chronic liver disease. *American Journal of Roentgenology*, 197(1):64–70, 2011.

[78] Runge JH, Hoelzl SH, Sudakova J, Dokumaci AS, Nelissen JL, Guenthner C, Lee J, Troelstra M, Fovargue D, Stoker J, Nederveen AJ, Nordsletten D, Sinkus R. A novel magnetic resonance elastography transducer concept based on a rotational eccentric mass: Preliminary experiences with the gravitational transducer. *Physics in Medicine and Biology*, 64(4), 2019.

[79] Zheng Y, Li G, Chen M, Chan QC, Hu SG, Zhao XN, Ehman RL, Lam EY, Yang ES. Magnetic resonance elastography with twin pneumatic drivers for wave compensation. *Proceedings of the 29th Annual International Conference of the IEEE Engineering in Medicine and Biology*, pages 2611–2613, 2007.

[80] Hughes JD, Fattahi N, Van Gompel J, Arani A, Meyer F, Lanzino G, Link MJ, Ehman R, Huston J. Higher-Resolution Magnetic Resonance Elastography in Meningiomas to Determine Intratumoral Consistency. *Neurosurgery*, 77(4):653–659, oct 2015.

[81] Pepin KM, McGee KP, Arani A, Lake DS, Glaser KJ, Manduca A, Parney IF, Ehman RL, Huston J. MR Elastography Analysis of Glioma Stiffness and IDH1-Mutation Status. *AJNR. American Journal of Neuroradiology*, 39(1):31–36, jan 2018.

[82] Braun J, Braun K, Sack I. Electromagnetic actuator for generating variably oriented shear waves in MR elastography. *Magnetic Resonance in Medicine*, 50(1):220–222, 2003.

[83] Hamhaber U, Sack I, Papazoglou S, Rump J, Klatt D, Braun J. Three-dimensional analysis of shear wave propagation observed by in vivo magnetic resonance elastography of the brain. *Acta Biomaterialia*, 3(1):127–137, 2007.

[84] Hirsch S, Guo J, Reiter R, Papazoglou S, Kroencke T, Braun J, Sack I. MR Elastography of the Liver and the Spleen Using a Piezoelectric Driver, Single-Shot Wave-Field Acquisition, and Multifrequency Dual Parameter Reconstruction. *Magnetic Resonance in Medicine*, 71(1):267–277, 2014.

[85] Gallichan D, Robson MD, Bartsch A, Miller KL. TREMR: Table-resonance elastography with MR. *Magnetic Resonance in Medicine*, 62(3):815–821, 2009.

[86] Soellinger M, Rutz AK, Kozerke S, Boesiger P. 3D cine displacement-encoded MRI of pulsatile brain motion. *Magnetic Resonance in Medicine*, 61(1):153–162, 2009.

[87] Weaver JB, Pattison AJ, McGarry MD, Perreard IM, Swienckowski JG, Eskey CJ, Lollis SS, Paulsen KD. Brain mechanical property measurement using MRE with intrinsic activation. *Physics in Medicine and Biology*, 57(22):7275–7287, 2012.

[88] Lipp A, Trbojevic R, Paul F, Fehlner A, Hirsch S, Scheel M, Noack C, Braun J, Sack I. Cerebral magnetic resonance elastography in supranuclear palsy and idiopathic Parkinson's disease. *NeuroImage: Clinical*, 3:381–387, 2013.

[89] Dittmann F, Hirsch S, Tzschätzsch H, Guo J, Braun J, Sack I. In vivo wideband multifrequency MR elastography of the human brain and liver. *Magnetic Resonance in Medicine*, 76(4):1116–1126, 2016.

[90] Hetzer S, Birr P, Fehlner A, Hirsch S, Dittmann F, Barnhill E, Braun J, Sack I. Perfusion alters stiffness of deep gray matter. *Journal of Cerebral Blood Flow and Metabolism*, 38(1):116–125, 2018.

[91] Guenthner C Kozerke S. Encoding and readout strategies in magnetic resonance elastography. *NMR in Biomedicine*, 31(10):1–29, 2018.

[92] Garteiser P, Sahebjavaher RS, Ter Beek LC, Salcudean S, Vilgrain V, Van Beers BE, Sinkus R. Rapid acquisition of multifrequency, multislice and multidirectional MR elastography data with a fractionally encoded gradient echo sequence. *NMR in Biomedicine*, 26(10):1326–1335, oct 2013.

[93] Huwart L, Peeters F, Sinkus R, Annet L, Salameh N, Beek LCt, Horsmans Y, Van Beers BE. Liver fibrosis: Non-invasive assessment with MR elastography. *NMR in Biomedicine*, 19(2):173–179, apr 2006.

[94] Klatt D, Asbach P, Rump J, Papazoglou S, Somasundaram R, Modrow J, Braun J, Sack I. In Vivo Determination of Hepatic Stiffness Using Steady-State Free Precession Magnetic Resonance Elastography. *Investigative Radiology*, 41(12):841–848, dec 2006.

[95] Maderwald S, Uffmann K, Galbán CJ, De Greiff A, Ladd ME. Accelerating MR elastography: A multiecho phase-contrast gradient-echo sequence. *Journal of Magnetic Resonance Imaging*, 23(5):774–780, 2006.

[96] Bernstein MA, King KF, Zhou XJ. *Handbook of MRI Pulse Sequences.* Elsevier Academic Press, 2004.

[97] Dunn TC Majumdar S. Comparison of motion encoding waveforms for magnetic resonance elastography at 3T. *Proceedings of the 2005 IEEE Engineering in Medicine and Biology 27th Annual Conference Shanghai, China, September 1-4, 2005*, (September 1-4):7405–7408, 2005.

[98] Klatt D, Johnson CL, Magin RL. Simultaneous, multidirectional acquisition of displacement fields in magnetic resonance elastography of the in vivo human brain. *Journal of Magnetic Resonance Imaging*, 42(2):297–304, 2015.

[99] Hirsch S, Klatt D, Freimann F, Scheel M, Braun J, Sack I. In vivo measurement of volumetric strain in the human brain induced by arterial pulsation and harmonic waves. *Magnetic Resonance in Medicine*, 70(3):671–683, 2013.

[100] Weaver JB, Qin X, Doyley MM, Van Houten EE, Kennedy FE, Paulsen KD. Encoding Harmonic Motion in MR Elastography Using the Imaging Gradients. *Proc. Intl. Soc. Mag. Reson. Med. 11*, 11:1077, 2003.

[101] Numano T, Mizuhara K, Hata J, Washio T, Homma K. A simple method for MR elastography: A gradient-echo type multi-echo sequence. *Magnetic Resonance Imaging*, 33(1):31–37, 2015.

[102] Wu B Lai Y. Temporal phase transition via fractional wave cycle TR in MR elastography. *Proc. Intl. Soc. Mag. Reson. Med. 21*, page 3699, 2013.

[103] Klatt D, Yasar TK, Royston TJ, Magin RL. Sample interval modulation for the simultaneous acquisition of displacement vector data in magnetic resonance elastography: Theory and application. *Physics in Medicine and Biology*, 58(24):8663–8675, 2013.

[104] Burstein D. Stimulated echoes: Description, applications, practical hints. *Concepts in Magnetic Resonance*, 8(4):269–278, 1996.

[105] Haacke EM, Brown RW, Thompson MR, Venkatesan R. *Magnetic Resonance Imaging: Physical Principles and Sequence Design: Second Edition.* Wiley-Liss, 1999.

[106] Aletras AH, Ding S, Balaban RS, Wen H. DENSE: Displacement Encoding with Stimulated Echoes in Cardiac Functional MRI. *Journal of Magnetic Resonance*, 137(1):247–252, 1999.

[107] Strasser J, Pirpamer L, Fazekas F, Ropele S. Fast Magnetic Resonance Elastography using a DENSE approach with Multi Phase Offset Readout. *Proc. Intl. Soc. Mag. Reson. Med. 25*, page 1370, 2017.

[108] Strasser J, Fazekas F, Ropele S. Low frequency excited MR elastography of the brain using displacement encoding with stimulated echoes and multi phase offset readouts. *Proceedings of the Joint Annual Meeting ISMRM-ESMRMB 2018*, page 2282, jun 2018.

[109] Strasser J, Haindl MT, Stollberger R, Fazekas F, Ropele S. Magnetic resonance elastography of the human brain using a multiphase DENSE acquisition. *Magnetic Resonance in Medicine*, 81(6):3578–3587, 2019.

[110] Strasser J, Soellradl M, Enzinger C, Ropele S. Accelerating DENSE MR elastography by including multi-axes motion encoding into the multiphase DENSE-MRE acquisition scheme. *Proceedings of the ISMRM 28th Annual Meeting and Exhibition 2020*, page 0170, Aug 2020.

[111] Robinson SD, Bredies K, Khabipova D, Dymerska B, Marques JP, Schweser F. An illustrated comparison of processing methods for MR phase imaging and QSM: combining array coil signals and phase unwrapping. *NMR in Biomedicine*, 30(4):e3601, 2017.

[112] Maharjan S, Numano T, Habe T, Ito D, Ueki T, Igarashi K, Maeno T. Phase Unwrapping in Magnetic Resonance Elastography. *Open Journal of Medical Imaging*, 08(04):111–125, 2018.

[113] Ghiglia DC Pritt MD. *Two-Dimensional Phase Unwrapping: Theory, Algorithms, and Software*. Wiley-Interscience, 1998.

[114] Barnhill E, Kennedy P, Johnson CL, Mada M, Roberts N. Real-time 4D phase unwrapping applied to magnetic resonance elastography. *Magnetic Resonance in Medicine*, 73(6):2321–2331, 2015.

[115] Papazoglou S, Xu C, Hamhaber U, Siebert E, Bohner G, Klingebiel R, Braun J, Sack I. Scatter-based magnetic resonance elastography. *Phys. Med. Biol.*, 54:2229–2241, 2009.

[116] Murphy MC, Manduca A, Trzasko JD, Glaser KJ, Huston III J, Ehman RL. Artificial neural networks for stiffness estimation in magnetic resonance elastography. *Magnetic Resonance in Medicine*, 80(1):351–360, 2018.

[117] Jiang X, Asbach P, Streitberger KJ, Thomas A, Hamm B, Braun J, Sack I, Guo J. In vivo high-resolution magnetic resonance elastography of the uterine corpus and cervix. *European Radiology*, 24(12):3025–3033, 2014.

[118] Finsterbusch J Frahm J. Half-Fourier single-shot STEAM MRI. *Magnetic Resonance in Medicine*, 47(3):611–615, 2002.

[119] Tofts P, editor. *Quantitative MRI of the Brain: Measuring Changes Caused by Disease*. John Wiley & Sons, Ltd, 2003.

[120] Lin C, Bernstein M, Huston J, Fain S. Measurements of T1 relaxation times at 3.0T: implications for clinical MRA. *Proc Intl Soc Mag Reson Med*, 9:1391, 2001.

[121] Wansapura JP, Holland SK, Dunn RS, Ball WS. NMR Relaxation Times in the Human Brain at 3 . 0 Tesla. *Journal of Magnetic Resonance Imaging*, 9:531–538, 1999.

[122] Crawley AP, Wood ML, Henkelman RM. Elimination of transverse coherences in FLASH MRI. *Magnetic Resonance in Medicine*, 8(3):248–260, 1988.

[123] Zur Y, Wood ML, Neuringer LJ. Spoiling of Transverse Magnetization in Steady-State Sequences. *Magnetic Resonance in Medicine*, 21:251–263, 1991.

[124] Scheffler K. A pictorial description of steady-states in rapid magnetic resonance imaging. *Concepts in Magnetic Resonance*, 11(5):291–304, 1999.

[125] Leupold J Hennig J. Increasing spoiling efficiency in RF-spoiled gradient echo sequences by averaging of RF phase-cycle-adapted k-spaces. *Magnetic Resonance in Medicine*, 66(4):1123–1128, 2011.

[126] Doyley MM, Weaver JB, Van Houten EE, Kennedy FE, Paulsen KD. Thresholds for detecting and characterizing focal lesions using steady-state MR elastography. *Medical Physics*, 30(4):495–504, 2003.

[127] Chan QC, Li G, Ehman RL, Grimm RC, Li R, Yang ES. Needle shear wave driver for magnetic resonance elastography. *Magnetic Resonance in Medicine*, 55(5):1175–1179, 2006.

[128] Doyley MM, Feng Q, Weaver JB, Paulsen KD. Performance analysis of steady-state harmonic elastography. *Physics in Medicine and Biology*, 52:2657–2674, 2007.

[129] Okamoto RJ, Clayton EH, Bayly PV. Viscoelastic properties of soft gels: Comparison of magnetic resonance elastography and dynamic shear testing in the shear wave regime. *Physics in Medicine and Biology*, 56(19):6379–6400, 2011.

[130] Henni AH, Schmitt C, Cloutier G. Shear wave induced resonance elastography of soft heterogeneous media. *Journal of Biomechanics*, 43(8):1488–1493, 2010.

[131] Evertz LQ, Chen J, Kugel JL, Ehman RL. Evaluation of Commonly Available Materials for MR Elastography Phantoms. *Proc. Int. Soc. Mag. Res. Med.*, 21:2441, 2013.

[132] Ghoz HM, Kröner PT, Stancampiano FF, Bowman AW, Vishnu P, Heckman MG, Diehl NN, McLeod E, Nikpour N, Palmer WC. Hepatic iron overload identified by magnetic resonance imaging-based T2* is a predictor of non-diagnostic elastography. *Quantitative Imaging in Medicine and Surgery*, 9(6):921–927, 2019.

[133] Mariappan YK, Dzyubak B, Glaser KJ, Venkatesh SK, Sirlin CB, Hooker J, McGee KP, Ehman RL. Application of modifed spinecho-based sequences for hepatic MR elastography: Evaluation, comparison with the conventional gradient-echo sequence, and preliminary clinical experience. *Radiology*, 282(2):390–398, 2017.

[134] Mura J, Schrank F, Sack I. An analytical solution to the dispersion-by-inversion problem in magnetic resonance elastography. *Magnetic Resonance in Medicine*, 84:61–71, 2020.